In Situ Examination of Nanoscale Reaction Pathways in Battery Materials

A Dissertation
Presented to
The Academic Faculty

by

Matthew G. Boebinger

In Partial Fulfillment
Of the Requirements for the Degree
Doctor of Philosophy in
Materials Science and Engineering

Georgia Institute of Technology
May 2020

In Situ Examination of Nanoscale Reaction Pathways in Battery Materials

Approved by:

Dr. Matthew McDowell, Advisor
School of Materials Science and Engineering
George W. Woodruff School of Mechanical Engineering
Georgia Institute of Technology

Dr. Josh Kacher
School of Materials Science and Engineering
Georgia Institute of Technology

Dr. Meilin Liu
School of Materials Science and Engineering
Georgia Institute of Technology

Dr. Gleb Yushin
School of Materials Science and Engineering
Georgia Institute of Technology

Dr. Ting Zhu
George W. Woodruff School of Mechanical Engineering
Georgia Institute of Technology

Dr. Raymond Unocic
Center for Nanophase Materials Sciences
Oak Ridge National Laboratory

Date Approved: March 2, 2020

I would like to dedicate this dissertation to my family, friends and girlfriend who have supported me all along the way.

ACKNOWLEDGEMENTS

First of all, I would like to express my deepest gratitude to my advisor Dr. Matthew McDowell for his leadership and guidance through my dissertation work. Matt's passion for research has been a great motivator for me and respect he has for his students, both graduate and undergraduate, have made his lab a wonderful workplace for the last 5 years. With his help I have been shaped into an independent scholar and researcher. I would also like to express my gratitude to my committee members Prof. Josh Kacher, Prof. Meilin Liu, Prof. Gleb Yushin, Prof. Ting, Zhu, and Dr. Raymond Unocic for spending their valuable time on my dissertation committee and providing valuable advice throughout the process. I would like to also thank Dr. Raymond Unocic specifically for all his guidance and mentorship during my time working with him at the Center for Nanophase Materials Science at Oak Ridge National Laboratory while on the Department of Energy SCGSR Fellowship. During this time Ray was a respectful and insightful mentor and the time at CNMS helped to confirm my desire to work as a researcher at a national laboratory upon graduation.

There are many colleagues within the McDowell Lab that I have worked with over the years that I am very grateful for. Neha Kondekar, a graduate student who entered the program with me as Matt's first graduate students, deserves a great deal of thanks as we went through our core classes, qualifying exams and the process of building a lab and watching it grow together. Francisco Cortes and Sang Yun Han were the next to join the group and have been great friends over the years and made the lab a fun and productive place to be. I will always enjoy bouncing ideas off one another in the office to help guide our individual research. I would also like to thank Jack Lewis, Jared Tippens, Stephanie Sandoval, Clay Wright,

Timothy Chen, Kelsey Cavallaro and Eugene Liu who have all come into the lab and quickly added to the wonderful work environment. Several post docs, Akila Thenuwara and Pralav Shetty, have also been a great help these last few years and helped me navigate the role of a senior graduate student. And of course, many undergraduate researchers have come and gone during my years and I thank them all for their hard work, however, I would like to thank a few that have been directly involved and assisted me in my research: Michael Xu, Casey Miles, and David Yeh. Finally, I would like to thank all the staff from the IEN Materials Characterization Facility staff at Georgia Tech for all their help, training and assistance with my experiments over the years. Without the access to the state-of-the-art equipment and their assistance my research would not be possible.

I would like to extend my gratitude to my friends both back home in Florida and here in Atlanta. Our game nights have been a wonderful stress relief over the last few years and I know that the friendships I have made during graduate school will last a lifetime. Of course, I must thank my family, my parents Karen and Gregory Boebinger and my siblings Dana (and brother-in-law Michael) and Scott have all provided a great deal of support and advice throughout my graduate school career. Finally, I am very grateful to my girlfriend Casey Rohman. Her love and support over the last few years, even when we were separated during my time working in Tennessee, have helped me so much as I finished up my dissertation. Thank you for everything.

TABLE OF CONTENTS

ACKNOWLEDGEMENTS iv

LIST OF TABLES ix

LIST OF FIGURES x

LIST OF SYMBOLS AND ABBREVIATIONS xv

SUMMARY xvii

CHAPTER 1. INTRODUCTION AND BACKGROUND 1

1.1 Alkali-Metal Ion Battery Electrochemistry 1

1.2 Current Li-ion Battery Systems 3

1.3 Alloying- and Conversion-Type Battery Materials 5

1.4 Sodium and Potassium Battery Systems 9

1.5 Experimental Materials Background 12

1.5.1 Copper (I) Sulfide Electrode Material 13

1.5.2 Iron (II) Disulfide Electrode Material 14

1.5.3 Antimony Electrode Material 16

1.6 Motivation and Scope of Research 17

CHAPTER 2. EXPERIMENTAL TECHNIQUES 22

2.1 *In Situ* Transmission Electron Microscopy 22

2.2 Electrochemistry 27

2.3 Materials Synthesis 29

2.4 X-ray Diffraction 31

CHAPTER 3. DISTINCT NANOSCALE REACTION PATHWAYS IN CONVERSION BATTERY MATERIAL 34

3.1 Introduction 34

3.2 Cu_2S Electrochemistry 35

3.2.1 Comparison of Li vs Na Cells 35

3.2.2 Cycling Behavior of Cu_2S/Na 38

3.2.3 Effect of Different Electrolytes on Cu_2S Electrochemistry 39

3.3 Phase Evolution of Cu_2S Sodiation 42

3.3.1 *Ex Situ* XRD of Na/Cu_2S and Li/Cu_2S 42

3.3.2 *In Situ* XRD of Na/Cu_2S and Li/Cu_2S 44

3.4 Electron Microscopy Analysis of the Cu_2S Reactions 46

3.4.1 *Ex Situ* Scanning Electron Microscopy of First Cycle 46

3.4.2 *In Situ* TEM of Cu_2S Sodiation 48
3.5 Conclusions 55
CHAPTER 4. FRACTURE BEHAVIOR IN CONVERSION MATERIAL WITH LARGER ALKALI-METAL IONS 57
4.1 Introduction 57
4.2 Electrochemical Behavior of FeS_2 58
4.3 Phase Evolution of FeS_2 60
4.4 *In Situ* TEM of FeS_2 Nanoscale Reaction Mechanisms 61
4.4.1 *In Situ* TEM of FeS_2 Lithiation 63
4.4.2 *In Situ* TEM of FeS_2 Sodiation 67
4.4.3 *In Situ* TEM of FeS_2 Potassiation 70
4.4.4 Comparison of the *In Situ* TEM of FeS_2 72
4.5 Linking Fracture to Phase Transformation Processes 73
4.5.1 Mechanical Properties of the Reacted Phase 74
4.5.2 Shape Evolution Effect on Fracture Behavior 78
4.5.3 Effect of Rate and Particle Size on Fracture Behavior 83
4.6 Modeling Stress Evolution During Reaction 84
4.7 Conclusions 88
CHAPTER 5. SPONTANEOUS AND REVERSIBLE HOLLOWING OF ALLOYING MATERIAL WITH LITHIUM 90
5.1 Introduction 90
5.2 *In Situ* TEM of Lithiation and Delithiation 91
5.2.1 Cycling Behavior 91
5.2.2 Delithiation Process Analysis 95
5.2.3 Structural Evolution During Reaction 103
5.2.4 Particle Size Effect 107
5.3 Effect on Electrochemical Cycling 111
5.4 Chemomechanical Model of Void Formation 118
5.4.1 Strain Energy Inducing Void Formation 120
5.4.2 Stress in Oxide Shell 124
5.5 Comparison to Other Material Systems 129
5.6 Conclusions 131
CHAPTER 6. CONCLUSIONS AND FUTURE WORK 134
APPENDIX 139

A.1 FeS_2 Chemomechanical Simulation Model 139
REFERENCES 143

LIST OF TABLES

Table 4.1: Maximum surface hydrostatic stress at varying extents of reaction for the two modeling simulations considered. 88

LIST OF FIGURES

Figure 1.1: Schematic of a Li-ion battery. 5

Figure 1.2: Schematic of different types of large-volume-change reactions. 7

Figure 1.3: Elemental Abundance of several elements within Earth's crust, including Li, Na and K. Figure from a study by Yabuuchi et. al.[4]..... 10

Figure 2.1: In situ TEM holder with the piezo-controlled cap and TEM half-grid. 24

Figure 2.2: Schematic representation of Bragg's Law with the incident beam coming from the upper left of the frame. This figure was taken from reference[94]. 33

Figure 3.1: (a) Galvanostatic curves for the Cu_2S electrodes in Na and Li half cells during the first cycle. **(b and c)** Cyclic voltammograms of the first cycle of the Li/Cu_2S half cell (b) and the Na/Cu_2S half cell (c). 36

Figure 3.2: (a) The specific capacity (red) and coulombic efficiency of a Na/Cu_2S half-cell undergoing galvanostatic cycling. **(b)** The discharge curves of the 1st (black), 2nd (blue), 10th (red) and 20th (green) discharge/charge curves tested at C/20. **(c)** Cycling rate tests at 1C (black), C/5 (blue) and C/20 (red). 39

Figure 3.3: Galvanostatic discharge/charge curves of a Na/Cu_2S cell with an electrolye consisting of monoglyme solvent with 1.0 M $NaPF_6$ salt at a rate of C/20. 40

Figure 3.4: Galvanostatic cycling (the first, second, and fifth cycle) of a Na/Cu_2S cell with EC/DEC solvent and 1.0 M $NaClO_4$ salt at a rate of C/20. 40

Figure 3.5: Galvanostatic cycling of a Li/Cu_2S half-cell using an electrolyte consisting of 1.0 M LiTFSI in DOL/DME. The cell was cycling at a rate of C/20. **(a)** Discharge/charge curves from the 10th cycle. **(b)** Specific capacity over 20 cycles. 41

Figure 3.6: Galvanostatic cycling (the first, second, and fifth cycle) of a Li/Cu_2S with EC/DEC solvent and 1.0 M $LiPF_6$ salt at a rate of C/10. 42

Figure 3.7: *Ex situ* XRD of Cu_2S/Li **(a)** and Cu_2S/Na **(b)** half cells showing the (111) and (200) Cu Bragg peaks after reaction. 43

Figure 3.8: *In situ* XRD traces during the initial discharge of **(a)** a Li/Cu_2S half-cell at C/30, and **(b)** a Na/Cu_2S half-cell at C/20. 45

Figure 3.9: *Ex situ* SEM images of Cu_2S electrodes in the pristine state **(a)**, after discharge in lithium **(b)** or sodium **(c)** cells, and after charge in lithium **(d)** or sodium **(e)** cells. 47

Figure 3.10: (a) Magnified SEM image of the lithiated Cu_2S electrode from Figure 3.9b. (**b)** The same image colorized with EDS signal emitted from different parts of the sample. 47

Figure 3.11: (a-d) Snapshots of the sodiation reaction of a group of Cu_2S nanocrystals on a thin amorphous carbon layer. **(e)** The SAED pattern after full sodiation. 49

Figure 3.12: Histogram of the measured area of Cu particles after sodiation of the Cu_2S nanocrystals from the data in Figure 3.11. 50

Figure 3.13: (a–d) Higher-magnification in situ TEM imaging during the sodiation of a small group of Cu_2S nanocrystals. **(e)** Magnified view of the boxed region in panel (d), showing the darker Cu

metal surrounded by lighter Na_2S. **(f)** Colorized Fourier-filtered image of panel (e). **(g)** Schematic of the lithiation and sodiation process of Cu_2S causing different structural/morphological evolution. ..52

Figure 4.1: Galvanostatic discharge curves for FeS_2 electrodes in Li, Na, and K half cells at a rate of C/20. 60

Figure 4.2: *Ex situ* XRD of FeS_2 electrodes before and after discharge in Li, Na, and K half cells.. 61

Figure 4.3: (a) Schematic of the *in situ* TEM experimental setup. **(b)** High resolution TEM image of an individual unreacted cubic FeS_2 crystal. **(c)** The fast Fourier transform (FFT) of the unreacted FeS_2 crystal in (b) showing that the material is cubic pyrite viewed along the [100] zone axis. 62

Figure 4.4: (a-d) Snapshots of the lithiation of two FeS_2 nanoparticles. **(a)** The particles prior to reaction with lithium. **(e)** The selected area electron diffraction (SAED) pattern of a group of pristine FeS_2 particles. **(f)** The SAED pattern of the lithiated FeS_2 crystals showing broad rings corresponding to Li_2S. **(g)** A plot displaying the occurrence of fracture after lithiation as a function of the initial particle size. 65

Figure 4.5: (a-d) Snapshot images from an *in situ* TEM experiment of the reaction of a group of particles with lithium..... 66

Figure 4.6: (a) High-resolution TEM (HRTEM) image of FeS_2 after reaction with Li. **(b)** Inverse FFT showing the lattice fringes that correspond to {111} Li_2S planes in (a). **(c)** Map of Fe particles in (a). 67

Figure 4.7: (a-d) Snapshots of the sodiation of a group of FeS_2 particles. **(e)** SAED pattern of the sodiated material. 69

Figure 4.8: (a-d) Snapshot images from an *in situ* TEM experiment of the reaction of a group of particles with sodium. 70

Figure 4.9: (a-d) Snapshots of the potassiation of FeS_2. **(e)** The SAED pattern of the final reacted amorphous product..... 71

Figure 4.10: (a-c) Snapshot images from an *in situ* TEM experiment of the reaction of a particle with potassium. 72

Figure 4.11: SEM image of the FeS_2 film on the Ta foil sulfurized at 500°C prior to electrochemical reactions in half-cells. 76

Figure 4.12: Nanoindentation experiments performed on electrochemically reacted FeS_2. **(a)** Representative force vs. displacement indentation curves of lithiated (red), sodiated (blue), and potassiated (green) FeS_2 films. **(b)** A bar chart showing the elastic modulus of each of the reacted films compared to pristine FeS_2. **(c)** A bar chart showing the hardness of each of the reacted films compared to pristine FeS_2. 77

Figure 4.13: Galvanostatic discharge curves for ~400 nm thick FeS_2 thin film electrodes from Li (red), Na (blue), and K (green) half cells used for nanoindentation tests. 77

Figure 4.14: Statistical plot that quantifies the change of the FeS_2 crystal shape during reaction with each of the alkali ions..... 80

Figure 4.15: Measurements of the size of the internal FeS_2 crystal during reaction of individual particles with Li^+ **(a)**, Na^+ **(b)**, and K^+ **(c)**. 84

Figure 4.16: Chemomechanical finite element simulation results showing stress generation during reaction of a cubic FeS_2 particle with different reaction front shapes. 87

Figure 5.1: (a) TEM image of the smaller Sb nanocrystals. **(b)** XRD trace of the smaller particles showing the R3m rhombohedral structure. **(c)** Histogram of the synthesized particles showing the distribution of particle size, including oxide layer. 92

Figure 5.2: (a) Schematic of the *in situ* TEM experimental setup. **(b-e)** TEM images of a group of Sb nanocrystals during cycling with Li. 94

Figure 5.3: Morphology evolution of a larger group of Sb nanocrystals during repeated cycling. **(a)** Group of pristine Sb crystals before cycling. 95

Figure 5.4: Analysis of the delithiation process of a group of Li-Sb nanocrystals. **(a-d)** Time-series of delithiation. Voids nucleate and grow in the particles at various times, resulting in the final sample (d) in which almost all particles have formed hollow singly-voided structures. **(e-g)** Magnified snapshots of three different particles. **(h)** Plot of the measured void area within each particle in the frame as a function of time. **(i)** Time required for delithiation of each of the particles extracted from each sigmoidal fit as a function of the delay from the beginning of the experiment. 97

Figure 5.5: Example process flow for segmentation analysis of the data in Fig. 5.4. **(a)** TEM image of delithiated particles. **(b)** Overlay of a color map on the with three segmented categories. **(c)** Color map of the three segmented categories. **(d)** Probability map derived from the color map of the Sb classifier. **(e)** The probability map from (d) after thresholding and binarization. **(f)** A pixel count was performed on the binarized image to obtain the particle size measurements. 99

Figure 5.6: Plot of the power parameter, *p*, *vs.* the position of the inflection point (in seconds), x_0, from the sigmoidal growth curves in Fig. 5.4h. 101

Figure 5.7: Plot of the volume of the delithiated Sb *vs.* the initial volume of the lithiated Sb for each particle in the frame in Figure 5.4. 102

Figure 5.8: Selected area electron diffraction (SAED) patterns from an *in situ* SAED experiment with Sb particles along with the corresponding images. **(a)** SAED pattern of the pristine Sb nanocrystals with crystalline rings corresponding to the rhombohedral Sb structure. **(b)** SAED pattern after lithiation showing diffraction rings corresponding to the cubic Li_3Sb phase, as well as another ring from polycrystalline Li_2O. **(c)** SAED pattern of the delithiated cluster of nanocrystals with only the ring from Li_2O visible. **(d)** SAED pattern corresponding to the relithiated particle with no detectable Li_3Sb rings present, but with the Li_2O phase remaining. 104

Figure 5.9: Structural evolution of nanocrystals and larger nanoparticles. **(a)** Integrated intensity of SAED patterns of the group of nanocrystals in Fig. 1 at various stages during cycling. **(b)** High-resolution TEM image of a pristine Sb nanocrystal. **(c)** High-resolution TEM image of a delithiated nanocrystal. 104

Figure 5.10: *Ex situ* scanning TEM energy dispersive X-ray spectroscopy (EDS) of delithiated Sb particles. **(a)** BF-STEM image of a cluster of unreacted Sb nanocrystals. The EDS data show strong Sb signal (green) within the interior of the particle. **(b)** BF-STEM image of a particle that was lithiated and delithiated using *in situ* TEM. The STEM-EDS data of the delithiated particle shows a slightly weaker Sb signal within the interior where the void was formed, and the Sb is still present. 106

Figure 5.11: (a) TEM image of the larger Sb nanoparticles used for in situ TEM. **(b)** XRD trace showing that the larger Sb particles have the same structure as the smaller Sb nanoparticles. **(c)** Histogram showing the distribution of particle sizes for the larger particles. 107

Figure 5.12: (a) SAED of larger pristine Sb nanoparticles supported at the edge of the carbon TEM grid. **(b)** Image of larger Sb particles of various non-uniform sizes and shapes. **(c)** The same group of larger particles after lithiation and volume expansion. **(d)** The same particles after delithiation. **(e)** SAED after delithiation, in which a few Sb diffraction spots remain. 108

Figure 5.13: *Ex situ* TEM image of Sb particles that were electrochemically lithiated and delithiated within a conventional liquid-electrolyte coin cell with a lithium metal counter electrode. 111

Figure 5.14: Characterization of larger nanoparticles synthesized via multiple injections for use in conventional electrochemical testing. **(a)** TEM image showing polydispersity. **(b)** X-ray diffraction shows that the material is single-phase Sb. **(c)** Histogram of particle size showing that the size is randomly distributed from 40 nm to 140 nm. 112

Figure 5.15: (a-c) Galvanostatic curves obtained at a current of 66 mA g^{-1} (C/10) from electrodes containing (a) 15 nm monodisperse nanocrystals, (b) 40-140 nm polydisperse nanoparticles, and (c) "bulk" particles (black: first cycle; red: second cycle; blue: 25^{th} cycle). 114

Figure 5.16: (a) Specific capacity with cycling at a current of 660 mA g^{-1} (1C) for the three types of electrodes. **(b-d)** Galvanostatic curves at a rate of 1C (660 mA g^{-1}) for Sb-based electrodes corresponding to the specific capacity plots in (a). **(b)** Small ~15 nm monodispersed nanocrystals, **(c)** large 40-140 nm polydisperse nanoparticles, and **(d)** bulk 325 mesh particles. 115

Figure 5.17: Specific capacity with cycling of Sb-based electrodes from multiple cells showing consistently long cycle life of the nanocrystals and larger nanoparticles. The electrodes were tested at 1C (triangles) or C/2 (circles). 116

Figure 5.18: Coulombic efficiency of the three types of electrodes over 100 cycles at 1C. Each dataset is averaged over multiple cells, with error bars representing the standard deviation for each cycle. The inset shows the same data but with an expanded range to show the CE of the first cycle. 117

Figure 5.19: Schematic of two possible morphological trajectories during delithiation. As Li^+ is removed from the Li-Sb phase under constraint from the oxide (top), the Li-Sb alloy experiences hydrostatic tensile stress ($\sigma h, core$) while the oxide shell experiences compressive stress $\sigma shell$. As these stresses increase during delithiation, the morphological result can either be a hollow void that grows within the Li-Sb (pathway 1) or the buckling of the oxide shell and particle shrinkage (pathway 2). 119

Figure 5.20: Schematics illustrating the origin of hydrostatic tensile strain within a spherical Li-Sb alloy particle during delithiation. 121

Figure 5.21: Plot of the critical strain required for void formation during delithiation as a function of initial particle diameter (blue curve, left axis) for a shell thickness of 5 nm. In the same plot, the resulting stress in the oxide shell at this critical strain is shown as a function of particle size (red curve, right axis). 123

Figure 5.22: Plot of the calculated stress in the oxide shell with thickness of 5 nm as a function of volumetric strain for several different particle core diameters, as shown in the legend. 125

Figure 5.23: Plot of the shell stress above which voids will form ($\sigma_{shell,v}$) as a function of particle diameter for three different oxide thickness values (dotted lines), as well as the shell stress above which shell buckling will occur ($\sigma_{shell,b}$) as solid lines..... 127

Figure 5.24: (a) Electrochemical impedance spectroscopy (EIS) of a nanocrystal-based working electrode in a half cell at different states of charge. Each curve features a single semicircle that was fit with a parallel resistor/capacitor equivalent circuit..... 129

Figure 5.25: Comparing *in situ* TEM sodiation/desodiation of Sb nanocrystals to lithiation/delithiation. **(a)** TEM image of a group of Sb nanocrystals that have undergone sodiation. **(b)** Image of a different group of Sb nanocrystals that have been desodiated. **(c)** TEM image of a group of Sb nanocrystals that have undergone lithiation, and **(d)** the same group after delithiation. 131

Figure A1.1: Chemomechanical finite element simulation results showing stress generation during reaction of a cubic FeS_2 particle with different reaction front shapes..... 142

LIST OF SYMBOLS AND ABBREVIATIONS

TEM	Transmission Electron Microscopy
SEI	Solid-Electrolyte Interphase
ΔG_r	Gibbs Free Energy of Reaction
E	Voltage
z	Charge Number
F	Faraday's Constant
mAh/g	Milliamp Hour per Gram
V	Volt
SHE	Standard Hydrogen Potential
CE	Coulombic Efficiency
ppm	Parts per Million
LC	Low Chalcocite
Ah/L	Amp Hour per Liter
nm	Nanometer
XRD	X-ray Diffraction
EDS	Energy Dispersive Spectroscopy
EELS	Electron-Energy Loss Spectroscopy
kV	Kilovolt
STM	Scanning Tunneling Microscope
STM	Scanning Tunneling Microscope
FFT	Fast-Fourier Transform
CV	Cyclic Voltammetry
PVDF	Polyvinylidene Difluoride
CMC	Sodium Carboxymethyl Cellulose
μm	Micron
d	Spacing between Diffracting Planes
θ	Incident Angele of X-rays
n	Order of Reflection
λ	Wavelength of Incident X-rays
ICDD	International Center for Diffraction Data
NMP	N-Methyl-2-pyrrolidone

C/#	Charge Rate
EC/DEC	carbonate electrolyte
DOL/DME	dioxolane/monoglyme electrolyte
SEM	Scanning Electron Microscopy
SAED	Selected Area Electron Diffraction
HRTEM	High-resolution Transmission Electron Microscopy
sccm	Standard Cubic Centimeter per Minute
μN	micronewton
C_{Li}	Lithium Concentration
$C_{Na/K}$	Sodium/Potassium Concentration
σ_h	Hydrostatic Tensile Stress
Q	Scattering Vector
SDD	Silicon-Drift Detector System
BF-STEM	Bright-Field Scanning Transmission Electron Microscopy
σ_{shell}	Compressive Stress
γ_σ	Total Surface Energy
dU	Differential Internal Energy
dV	Differential Volume
B	Bulk Modulus
$\Delta V/V_o$	Volumetric Strain
C	Integration Constant
U	Internal Energy
E	Surface Energy
t	Thickness
$\sigma_{shell,b}$	Buckling Stress
E	Young's Modulus
v	Poisson's Ratio
$\sigma_{shell,v}$	Shell Stress During Void Formation
EIS	Electrochemical Impedance Spectroscopy
D_o	Diffusion Coefficient
ε_{ij}^e	Elastic Strain
β_{ij}^e	Isotropic Expansion Coefficient

SUMMARY

In order to engineer less expensive and more energy-dense batteries, new materials that can reliably store and transport active ions must be first developed. However, these materials are known for their poor reversibility due to large morphological changes during cycling. To maximize reversibility during charge and discharge, we must be able to understand and control the electrochemical reaction mechanisms of these new electrode materials. This dissertation uses *in situ* experiments, primarily *in situ* transmission electron microscopy (TEM), to understand the nanoscale reaction pathways in various high-capacity electrode materials during reactions with Li^+, Na^+, and K^+ ions. Upon reacting with alkali-metal ions, these electrode materials often exhibit much higher specific storage capacities than conventional Li-ion battery electrode materials. In addition, these types of materials can also be used in lower-cost sodium- and potassium-based systems. Hence, they could replace electrode materials in Li-ion batteries, which would make possible engineering batteries with higher specific energy. However, the more substantial volumetric changes that these electrode materials undergo during reaction cause a significant decrease in the capacity retention. This decrease in the capacity retention is caused by the mechanical fracture of the active material and continuous growth of the solid-electrolyte interphase (SEI) on the surface of the anode particles, which both lead to very low cyclability of these systems.

If these battery systems are to be improved, it is critical to understand both how the larger Na^+ and K^+ ions affect the nanoscale phase transformations during these reactions and how to engineer high capacity battery materials with high coulombic efficiency and longer

cycle life. As part of the research described in this dissertation, studies on the Cu_2S and FeS_2 active materials were conducted to examine the effect that larger alkali metal ions have on the reaction mechanisms of large-volume-change materials. Evidence obtained from extensive *in situ* and *ex situ* experiments suggests that the larger volume changes associated with the sodium/potassium reactions indicate that the different reaction pathways affect the materials behavior. This altered reaction behavior results in a more stable morphology for the overall cycling of the electrode material. In an effort to aid the engineering of a high capacity battery material with longer cycle life, a study was conducted on Sb nanocrystal electrode materials that exhibited stable electrochemical behavior. This study demonstrated that small spherical particles naturally formed uniform internal voids that were easily filled and vacated during cycling. This was found to be due to the resilient lithiated oxide layer that formed after the first lithiation and subsequently prevented shrinkage during delithiation. A chemomechanical model describing the void formation was developed; this model can serve as a tool to guide the creation of oxide or other shells that enable alloying materials to undergo voiding transformations *in situ*. When reacting with alkali ions of different sizes, all of these materials (Cu_2S, FeS_2, and Sb) exhibited counter-intuitive phase evolution and mechanical degradation behavior. The findings indicate that, thanks to their high energy density, large-volume-change materials could make possible the development of next-generation batteries, whether they be Li-ion batteries or batteries with other chemistries that undergo complex morphological changes.

CHAPTER 1. INTRODUCTION AND BACKGROUND

As an efficient electrical energy storage system for the renewable energy market and as a power source for transportation, defense, aerospace and consumer electronic applications, Li-ion batteries have revolutionized the modern world and have become commonplace in developed nations since their first commercialization in 1991.[1–4] However current Li-ion technology cannot meet the growing demand for high energy density and long cycle life as these markets expand.[1–6] This has helped fuel the search of electrode materials with higher gravimetric and volumetric specific capacities in recent years while also lowering the high cost it takes to fabricate Li-ion batteries. However, it has been found that increasing the capacity generally leads to a decrease in the cyclability.[7–9] Therefore, there must be a concerted effort to understand the chemomechanical degradation of these electrode materials to enable their use in alkali-metal ion battery systems.

1.1 Alkali-Metal Ion Battery Electrochemistry

Batteries are an energy storage device that store chemical energy and converts this to electrical energy and vice versa by shuttling ions between two electrodes during charge-discharge cycles. An alkali-metal ion battery is composed of a positive electrode (cathode) and a negative electrode (anode) separated by an ionically conductive, but electrically insulating, liquid electrolyte, as seen in Figure 1.1. These electrodes are generally composite structures made of a mixture of active material particles, conductive additive, and polymer binder. This results in a very porous electrode with a large amount of surface

area available for the redox reactions to take place during cycling. These electrode films are adhered to metallic current collectors to ensure electrical contact. Within these electrodes themselves the conductive additive ensures electrical contact between the battery framework and the active materials. Physical separation between the electrodes is maintained using a polymer separator soaked in an ionically conductive liquid electrolyte. This liquid electrolyte generally consists of an organic solvent containing a dissolved alkali-metal salt.

As the alkali-metal ions flow through the electrolyte during cycling they electrochemically react with the positive and negative electrodes. The chemical driving force across the cell that allows this flow is due to the difference in the chemical potential of the two electrodes. This difference in the chemical potential is directly related to the standard Gibbs free energy change per mol of reaction, ΔG_r°. During the discharge process, electrons are taken out of the negative electrode, where the chemical potential is the highest. These electrons are moved through the current collector and the outer circuit, and then inserted into the positive electrode. The bulk charge neutrality is maintained as the electrochemical potential difference between the two electrodes drives the ions through the electrolyte from the anode, where oxidation is occurring, to the cathode, where reduction is occurring. The relation between the Gibbs free energy of the reaction is directly related to the electrochemical potential, or voltage, of the battery through the following equation,

$$E = -\frac{\Delta G_r^\circ}{zF} \qquad \text{(Eq. 1.1)}$$

where E is the measurable voltage between the two electrodes, z is defined as the charge number of the mobile ionic species and F is Faraday's constant. This flow of electrons and

ions can be reversed in these types of cells if a high enough voltage to overcome the driving force of the chemical reaction is imposed on the cell in the opposite direction. This will result in the current to flow in the other direction, meaning the electrical energy will be consumed and the chemical energy will increase, and thus the cell will be recharged.[10] In terms of voltage of the cell, as energy is extracted from the cell during discharge, the voltage decreases, and as the cell is recharged and energy is being reinserted into the cell, the voltage increases.

1.2 Current Li-ion Battery Systems

Conventional commercial Li-ion batteries traditionally make use of a graphitic anode, a layered transition metal lithium oxide cathode (140-160 mAh/g)[1,11,12] and a polymer separator soaked in an organic liquid electrolyte that consists of a carbonate solvent and Li salts, such as $LiPF_6$.[12,13] The particulate cathode is attached to an aluminum metal current collector, while the anode is spread on a copper current collector.[14] A schematic of this battery setup can be seen in Figure 1.1. Typical negative electrode materials have potentials near the electrochemical potential of the Li^+/Li redox reaction (at -3.04 V vs. the standard hydrogen potential (SHE)), usually around 0.01-0.5 V vs. Li^+/Li. Positive electrode materials have potentials in the range of 3-4 V vs. Li^+/Li. The positive electrode potential is maximized in order to maximize the total specific energy of the two electrodes, since the total energy is found by multiplying the total charge capacity by the voltage of the couple.

During operation, the redox reactions in conventional Li-ion batteries take place through an intercalation-type mechanism. In this reaction, lithium ions are inserted between atomic layers of the electrode materials into the interstitial sites with minor structural changes as the battery is repeatedly cycled.[2,11,14] This causes relatively small volume changes, hence retaining capacity over repeated cycles as a stable morphology is maintained, which allows for a thin stable SEI to grow on the electrode surface. However, this lower volume expansion is directly linked to the few available sites for Li ions to be stored in, hence resulting in low specific capacity. For example, upon full reaction of lithium with graphite, the chemical compound LiC_6 is formed as seen below,

$$Li^+ + e^- + 6C \rightarrow LiC_6 \qquad \text{(Eq. 1.2)}$$

limiting its theoretical capacity to 372 mAh/g. While intercalation-type materials are generally more structurally and electrochemically stable during cycling, the energy density of these battery systems remains an issue due to the relatively low possible alkali-metal concentration. One option to increase the overall capacity these battery materials can store is by examining different reaction mechanisms battery materials can undergo. The focus of this work is the development of different type of these promising materials that address these concerns for the future development of high-capacity electrode materials.

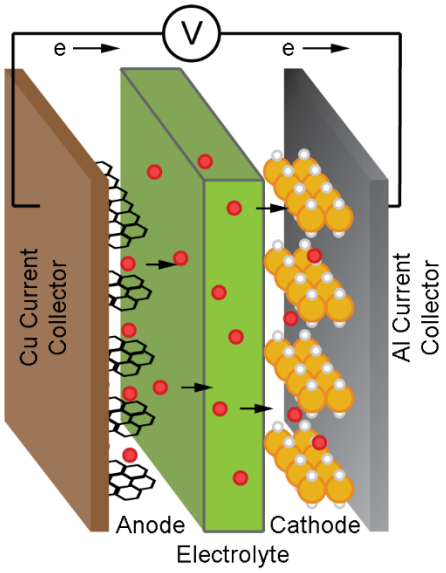

Figure 1.1: Schematic of a Li-ion battery. The battery is made up of an anode and a cathode separated by a Li-containing electrolyte. The anodic active material is made of graphitic carbon and the cathodic active material is generally made of a transition metal lithium oxide material. Both of these electrode materials store lithium through intercalation of the Li between the layers of the material.

1.3 Alloying- and Conversion-Type Battery Materials

Most current Li-ion battery systems make use of intercalation-type materials with good cyclability due to minor structural changes; however, as previously stated, the energy density of these materials is relatively low. This has led to a great deal of research on large-volume-change reaction materials with much larger specific capacities for use in Li^+-based systems.[15–19] Commonly they are divided into two different types of reactions, the alloying- and conversion-type which are defined according to the characteristics of the reaction that takes place.

Materials that alloy with lithium are an attractive candidate for negative electrodes of Li-ion batteries. Alloying-type reactions refer to the active materials electrochemically forming compound phases made of the alkali ions and metals and can be seen in Figure 1.2a. Many materials such as silicon, germanium, aluminum, lead, silver, gold, tin, antimony, and others have been found to alloy with lithium at the low potentials that negative electrodes react at. The alloying process involves breaking the bonds between the host atoms, which leads to dramatic structural and volumetric changes.[9,20–22] Since the atomic framework is destroyed in this reaction the theoretical specific capacities of alloy anodes are generally 2-10 times higher than that of graphite. For example, fully-lithiated alloyed Si forms the $Li_{22}Si_5$ phase with a specific capacity of 4200 mAh/g, and it experiences a 310% volume expansion.[16–18,23,24]

A conversion-type reaction involves the reaction of an alkali metal species with a transition-metal compound, such as an oxide or sulfide, generally forming a mixture of multiple new phases, as shown in Figure 1.2b. In this mixture, one phase is a new compound that incorporates the alkali ion (such as Li_2O or Li_2S), and the other new phase is a stable transition metal species. The final reaction product is a nanoscale mixture of these two phases.[19,25] A subset of these conversion-type reaction is a displacement reaction and can be seen in Figure 1c.[19,26,27] In this reaction, the inserted ion displaces the metal ions, expelling them to the surface where they are reduced, resulting in a mixture of the alkali-metal compound and transition metal similar to a conversion-type reaction.[26] The overall crystal structure undergoes only minor changes during this process. This reaction is enabled by several factors: (i) the initial and final sulfide/oxide phases of the reaction have similar crystal structures, (ii) the initial and final sulfide/oxide phases have similar

molar volumes, (iii) and the ionic conductivities of the alkali metal ion and transition metal ion in the initial sulfide/oxide structure are very high.[19,28] For all conversion-type reaction materials, this formation of a two-phase mixture results in large-volume changes which leads to high specific capacity.

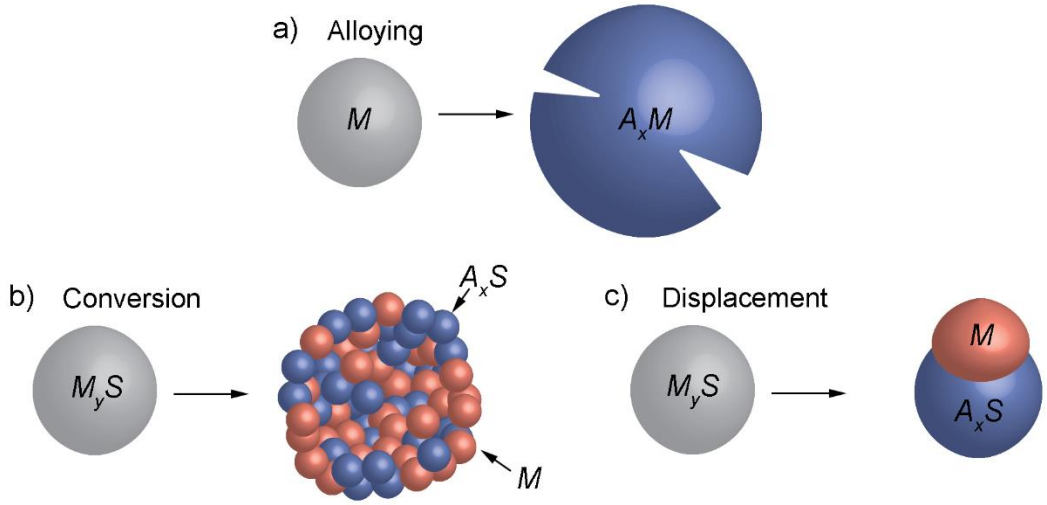

Figure 1.2: Schematic of different types of large-volume-change reactions. **(a)** Alloying-type reaction occurs when the active material alloys with the alkali-metal ions, generally resulting in the largest volume expansion and fracture. **(b)** Conversion-type reactions result in nanoscale phase separation to form the mixed metal/sulfide phases. **(c)** Displacement-type reaction are a unique type of conversion reactions that occur and are distinguished by direct replacement of the metal with the alkali-metal ion.

As previously stated, these materials experience significant volumetric and structural changes during both ion insertion and removal, as these materials shrink drastically during ion removal.[29,30] This is consistent for all these types of reaction mechanisms and can cause major problems for electrodes made of these materials. One such problem is the pulverization or fracture of the particles during cycling which can result

in the loss of contact between the electrode framework and the active material.[16–18,29,31,32] This, in turn, can result in irreversible capacity loss as the active material is electrically disconnected from the framework. Additionally, the cyclic volume changes of these materials repeatedly break the solid-electrolyte interphase (SEI) layer. This exposes the surface of the active material leading to continuous SEI growth rather than the formation of a thin passivating SEI layer. This continuous SEI growth results in a much lower Coulombic efficiency (CE) and increases the overall impedance as new SEI is formed every cycle.[9,11,33–35] Together, these effects can cause rapid capacity decay.

To mitigate the problems caused by these drastic volume changes, advanced nanostructures have been developed that can accommodate large volume changes by maintaining a dimensionally-stable outer surface during cycling. It has been shown that various types of hollow nanostructures improve the stability of materials while also supporting fast charge/discharge rates.[17,35–41] In particular the "yolk-shell" nanostructures have proven very successful. These structures feature an inactive outer shell that surrounds a smaller active material that is detached from the outer shell, leaving a void around the active material.[17,36] This voided region is fabricated to be large enough to allow for the full volume expansion of the contained active material without straining the inactive shell. By maintaining the same outer surface during cycling, a stable, undamaged SEI can form resulting in higher CE and improved cycled life.[17,34,36] However while these yolk-shell structured electrodes have shown significantly improved electrochemical properties, the synthesis required to fabricate these materials involves multiple complicated and expensive processing steps, such as uniform coatings and removal of multiple sacrificial layers on the nanoparticles. These processes limit the commercial application of these materials. Several

types of alloying materials have been shown to exhibit pore formation at the nanoscale, such as Sn.[42,43] However the pores formed are non-uniform and still result in overall volume changes that lead to poor SEI formation. While internal voids have shown promise for nanostructured large-volume-change electrode materials, a more feasible material system must be found.

1.4 Sodium and Potassium Battery Systems

As the growth of technological markets, such as electric transportation and renewable energy production continues, electrical energy storage systems with advantages in cost as well as cyclability and energy density must be found.[1–4] While extensive research has been conducted on high capacity electrode materials for lithium systems, not much is known about how electrochemical reactions with other ions influence phase transformation dynamics and mechanical degradation of these active materials.

Sodium-ion[44,45] and emerging potassium-ion[46,47] batteries provide promising affordable alternatives to Li-ion battery systems. This reduction of cost is due to the fact that Na- and K-ion battery systems can make use of less expensive and lighter-weight aluminum, rather than copper, metal current collectors. This is due to sodium and potassium not forming alloys with aluminum at low potentials like lithium does.[48] In addition to saving on manufacturing costs, sodium and potassium are each ~1000 times more abundant than lithium in the Earth's crust (Figure 1.3),[4] and there is an almost infinite supply of sodium in the ocean. The abundance may lead to cost reduction, which makes

these alternative types of alkali-metal batteries of great interest for multiple technology markets searching for lighter and more cost-effective energy storage systems.

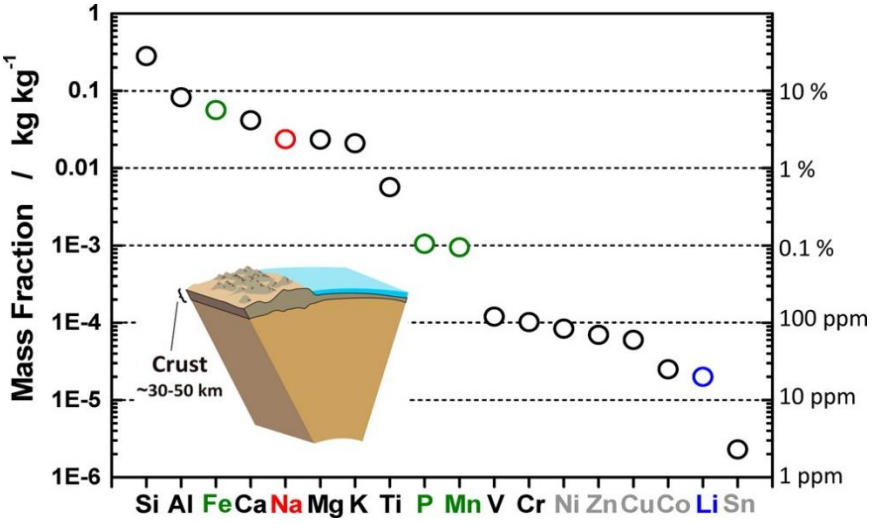

Figure 1.3: Elemental Abundance of several elements within Earth's crust, including Li, Na and K. Figure from a study by Yabuuchi et. al.[4]

Since Li, Na and K systems feature similar electrochemistry due to their monovalency, previous research and the existing knowledge of Li-related systems can be used to guide the synthesis, characterization and testing of electrode materials for Na and K systems. Recent developments of a variety of anode and cathode materials for use in Na-ion batteries have enabled the operation of these types of batteries at appropriate potentials with prolonged cycle life.[3,4] It has been known that sodium atoms do not intercalate well into graphite[3] due to the mismatch of the graphite interlayer distance with the larger Na^+ ions. Breakthroughs in the development of layered sodium transition-metal oxides that operate through intercalation reactions have produced Na-based cathodes with energy density comparable to lithium systems.[2,49] However, as previously stated, intercalation-type materials do not achieve the high specific energy required of new battery systems.

Therefore, the use of high-capacity anode materials for Na and K systems has recently seen more interest, however, improved understanding of reaction mechanisms is still required. Preliminary results have shown that alloying and conversion-type materials show very promising behavior and capacity retention in Na-ion systems. In alloying materials, such as Sn, Ge, and Sb, and conversion materials, such as FeS_2, similar electrochemical behavior, when compared to Li-ion systems, has been observed. In certain cases, such as Sb and FeS_2 battery systems, capacity retention of greater than 90% has been maintained over thousands of cycles.[3,49]

While most recent studies have placed more emphasis on the development of Na-ion systems, K-ion batteries also provide similar cost advantages when compared to Li-ion systems. Furthermore, the standard potential of the K/K^+ redox couple is comparable to that of Li/Li^+ (-2.93 V and -3.04 V vs SHE, respectively), while the standard redox potential of Na/Na^+ is -2.71 V vs. SHE. This means that, theoretically, K-ion batteries could deliver similar cell voltages as Li-ion batteries.[46,47,50–52] However, research into potassium based batteries is still in its infancy, with most studies currently only investigating carbon-based anodes.[46,47,50,53] While potassium has been shown to electrochemically intercalate into graphite to form KC_8 (theoretical capacity of 279 mAh/g), the exact mechanism by which potassium is stored is not fully understood and the low specific capacity of such electrodes is not ideal.[50,53] Several studies have shown that alloying materials, such as Sb, Sn, and P, when made into a composite electrode with some carbonaceous materials can be electrochemically cycled reliably.[50,53] Conversion materials such as FeS_2, also have been found to react with potassium by using the yolk-shell electrode architecture discussed previously, and have reported a specific capacity of 166 mAh/g for over 1000 cycles.[54]

However, the large volume changes associated with this reaction generally result in capacity decay from the theoretical capacity of 894 mAh/g upon full reaction. To further the development and improve electrochemical behavior of these different alkali-ion systems, a greater understanding of the basic phase transformations of electrode materials is needed.

In recent years, breakthroughs in the development of novel nanoscale architectures capable of controlling the large morphological changes have made these large-volume-change electrode materials more feasible in next-generation batteries.[17,55] However, due to the larger ionic radii of Na^+ and K^+ ions and the larger molar volumes of Na- and K- based compounds, it is expected that materials undergoing sodiation and potassiation will experience larger volumetric changes when compared to lithiation.[50,56] Previous studies have shown that these larger volumetric changes can be linked to mechanical degradation and fracture of electrode materials which can diminish the cyclability of these systems.[18,57,58] However, the impact of these larger ions on the structural, morphological and chemical evolution of these type of electrode materials is yet to be fully studied. Therefore, the nanoscale reaction processes in conversion and alloying battery materials must be investigated in detail to allow for effective use in rechargeable Na- and K-based battery systems.

1.5 Experimental Materials Background

Several different material systems have been investigated over the course of this dissertation. These consist of two different sulfide conversion-type reaction materials,

Cu_2S and FeS_2, and an alloying-type reaction material, Sb. It is worth noting that Cu_2S is known to undergo a displacement-type reaction with lithium.[19,26] Background information on these materials is presented in the next section.

1.5.1 Copper (I) Sulfide Electrode Material

Copper (I) sulfide was the first material examined in this dissertation work, and the results are presented in Chapter 3. Cu_2S in this study was of the low chalcocite (LC) phase. This phase consists of a distorted hexagonal-close-packed sulfur sub-lattice with Cu^+ ions occupying mainly triangular interstitial sites throughout.[59–61] This results in a crystal structure with monoclinic symmetry (space group $P2_1/c$). This chalcocite ore can be found naturally and makes this material relatively inexpensive compared to other materials needed for current battery electrodes.

Previous work on the material has shown that Cu_2S undergoes a displacement-type reaction with lithium.[19,26] As discussed previously, this unique type of reaction is due to the structure of the LC Cu_2S and resulting Li_2S phase. In this reaction, the inserted Li^+ displaces the Cu^+ ions within the crystal structure. Due to the very high ionic conductivities of both Li^+ and Cu^+ in the Cu_2S ($\sim 10^{-7}$ cm^2 s^{-1}),[19,28] the Li^+ expels the Cu^+ to the surface where the ions are reduced to Cu metal, resulting in a mixture of Li_2S and Cu metal.[26] During this reaction the overall crystal structure undergoes only minor changes as it converts from Cu_2S to Li_2S. This reaction is only possible due to the fact that the low chalcocite crystal structure of Cu_2S is very similar to the Li_2S structure, including their molar volumes which only have a $\sim$2.7% volume difference.

From previous work it is know that Cu_2S has a theoretical capacity of 335 mAh/g after undergoing a full reaction with both lithium and sodium through the electrochemical reaction seen below forming X_2S, where $X^+$is the alkali-metal ion species in question:

$$Cu_2S + 2X^+ + 2e^- \rightarrow X_2S + 2Cu \qquad \text{(Eq. 1.3)}$$

A study by Jache et. al. found that Cu_2S exhibits good reversibility in Li cells up to 150 cycles with negligible capacity decay.[28] However, when examining Cu_2S in a sodium cell using a 1.0 M $NaCF_3SO_3$ tetra ethylene glycol dimethyl ether electrolyte there was a drastic decrease in the capacity retention where they suggest that fully sodiation does not occur resulting in a Na_xCu_2S (x<2) phase is formed.[62] This unique type of reaction, and the difference in the cyclability between the Li and Na cells, make it an interesting materials system to study the effect that larger alkali-metal ions have on structural evolution.

1.5.2 Iron (II) Disulfide Electrode Material

The iron (II) disulfide reaction with lithium, sodium and potassium is examined in Chapter 4. This material is an ideal candidate for study in battery systems due to its natural abundance, inexpensive components, and very high theoretical capacity of 894 mAh/g. FeS_2 is known to be the prototype of the simple cubic crystallographic pyrite structure (space group $Pa\bar{3}$). The unit cell of this system is composed of a face-centered cubic sublattice of Fe, with each Fe atom surrounded by six S nearest neighbors in a distorted octahedral arrangement.[63] Each S is bonded to another S atom, as well as three Fe atoms, and the formal oxidation states of each element are Fe^{2+} and S_2^{2-}. The full electrochemical

conversion-type reaction of FeS_2 with alkali metal ions is expected to behave according to the following equation:

$$FeS_2 + 4X^+ + 4e^- \rightarrow Fe + 2X_2S \qquad \text{(Eq. 1.4)}$$

where X is the alkali metal of interest. The full conversion to X_2S would involve electrochemical reduction of both the Fe^{2+} cation and the S_2^{2-} species. Prior to the conversion reaction it has been shown that Li^+, Na^+ and K^+ ion intercalation takes place at higher relative voltages, but the theoretical specific capacity of all these reactions remains 894 mAh/g.[54,64]

Since the late 1980s, FeS_2 material has been in development as a potential battery material. Early efforts involved the use of molten salt FeS_2/Li-Al batteries, which have since fallen out of favor.[65] However, due the beneficial properties discussed above, interest in this material remains. Previous work has shown that FeS_2 undergoes a conversion-type reaction with Li as the above reaction indicates.[19,64,66] Nanoscale FeS_2 crystals have also been shown to be a promising, high-capacity electrode material for multiple types of batteries, including primary Li cells.[67] It has been reported that FeS_2-based secondary cells have relatively long cycle life in both Li- and Na-ion batteries (utilizing either partial reaction via intercalation or full conversion).[63,64,67–71] However several of these studies have shown that during cycling this material is not fully reversible in sodium cells. Yolk-shell structures have also been implemented for use in Na/FeS_2 cells and shown excellent cycling behavior for over 100 cycles.[72] Additionally FeS_2 electrodes have also shown promising high-capacity behavior in solid-state Li systems.[66,73] These beneficial

electrochemical properties makes this material ideal to study the effect that different alkali-metal ions have on nanostructured FeS_2 during initial discharge of the material.

1.5.3 Antimony Electrode Material

Uniform elemental antimony nanocrystals are examined in the final study in Chapter 5. As an alloy anode material, Sb is known to have a high theoretical specific capacity of 660 mAh/g and volumetric capacity of 1890 Ah/L[74–76] upon full lithiation to the Li_3Sb phase:

$$Sb + 3X^+ + 3e^- \rightarrow X_3Sb \qquad \text{(Eq. 1.5)}$$

It has been shown that a Li_2Sb phase can form (two plateaus at 0.82 and 0.78 V), however in the experimental data shown in Chapter 5, and in other studies[76] show the direct conversion from Sb to Li_3Sb is possible and takes place at 1.02 V. This alloying reaction results in a theoretical volume expansion of the material by a factor of 2.35.[76] The antimony used for this study has the rhombohedral structure (space group $R\bar{3}m$, $a = b = 0.4307$ nm, $c = 1.1273$ nm).While antimony is not as abundant as silicon, Sb remains a promising alloying electrode material due to the fact that it does not experience as drastic of volumetric changes, while still having a high specific and volumetric capacity.

Prior electrochemical studies of Sb electrode materials have shown varying degrees of cyclability with in both lithium and sodium based cells.[38,74,75,77,78] Additionally, as discussed previously, hollow nanostructures have been used with antimony to increase the electrochemical stability of these electrodes, with carbon "yolk-shell" structures[38] and Sb

nanotubes[77] showing exceptional cycle life and high coulombic efficiency. In a particularly interesting study by He *et al.*,[74] the electrochemical behavior and cycle life of uniform monodisperse Sb nanocrystals (diameter of 10-20 nm) were shown to be superior to larger Sb particles (diameter of many microns) in both Li- and Na-based systems. Additionally, these materials were found to have very good capacity retention even at faster rates. This is a unique finding as the high surface area of small nanocrystals can often result in poor CE and cycling behavior.[34,79] This intriguing finding, combined with the intrinsic advantages of antimony, makes it an interesting material to study the nanoscale reaction mechanisms using *in situ* methods.

1.6 Motivation and Scope of Research

Batteries are a part of everyday life and the growth in the electric vehicle and renewable energy market has called for the development of new energy storage with increased affordability, cyclability and/or energy density compared to current Li-ion systems.[1–4] Current Li-ion systems make use of a graphitic carbon anode and a layered lithium transition-metal oxide cathode, however these types of cells are reaching their limits. New batteries utilizing energy-dense conversion- and alloying-type battery systems are a possibility, but a great deal of research is needed to understand these systems to optimize their performance. These materials have very high specific Li storage capacities and enable the use of larger, cheaper alkali-metal ion systems, such as Na- and K-ion batteries. However, these reactions result in substantial morphological changes and volume expansion. The volume changes, ranging between 100-300%, cause significant challenges

such as mechanical fracture of the active particles and continuous growth of solid-electrolyte interphase (SEI).[23] This results in a lower Coulombic efficiency (CE), leading to early battery failure as the impedance continuously increases.[9,11,33–35]

Traditionally, researchers have made use of a variety of *ex situ* characterization techniques to understand battery transformations, but it is critical to understand the inner workings of a battery in order to engineer these new materials to overcome cycle life issues. As is true in all battery systems, the energy density and cycle life are heavily dependent on the phase transformations of active materials. In order to have complete understanding of how to better engineer these novel materials with higher capacity, the nanoscale reaction mechanisms that occur in these materials must be known. The primary objective during my studies was to use *in situ* transmission electron microscopy (TEM) to examine the nanoscale reactions of these materials to better understanding how these reactions affect the electrochemical behavior of the overall battery systems.

This work helped determine how nanoscale reaction pathways influence the electrochemical behavior of battery systems that make use of different alkali metal ions. Additionally, this work discovered the naturally occurring behavior of an alloying material that forms a unique hollow nanostructure upon delithiation that remains electrochemically stable during cycling. In the following chapters I will discuss various experiments conducted on the conversion-type materials, Cu_2S and FeS_2, and alloying-type reaction material, Sb, that undergo large volumetric expansion to guide the engineering of these energy-dense materials for increased stability and cycle life. This research helped determine the effect that different alkali metal reactions have on these large-volume-change materials that can help lead to the development of promising Na- and K-ion battery systems

with potentially lower cost than Li-ion systems. This work will enable the development of compact energy storage devices with high energy density and operational stability using high capacity electrode materials not used previously.

In Chapter 2, the various experimental techniques used for the studies on the Cu_2S, FeS_2 and Sb material are discussed. Within this chapter the specialized *in situ* transmission electron microscopy techniques used for each of these experiments are discussed along with the electrochemical techniques needed for the study of the battery materials. Additionally, other experimental techniques needed for these studies are discussed, such as the image processing techniques required after *in situ* TEM experiments. Finally, the syntheses required to fabricate these nanoscale electrode materials are discussed.

In Chapter 3, I discuss the sodiation of the displacement-type Cu_2S electrode material. For this study, a large amount of electrochemical data was collected, which demonstrated that the Na/Cu_2S reaction can exhibit cyclability comparable to Li/Cu_2S cells. However, the electrochemical behavior of these cells suggests different reaction mechanisms take place. Structural analysis of the Cu_2S, using both *ex situ* and *in situ* XRD showed that the resulting phases for both the lithiation and sodiation are very similar. *In situ* TEM techniques were then used to demonstrate the difference in the sodiation reaction from the displacement reaction seen during lithiation. The resulting morphology was found to be more electrochemically stable than the lithiation reaction. These results illustrate that the large volumetric changes involved with this reaction do not necessarily lead to worse electrochemical behavior, as commonly believed.

In Chapter 4, the sulfide conversion-type material, FeS_2 is studied using similar experimental techniques to determine the effect that Li^+, Na^+, and K^+ ions have on the reaction mechanisms and morphological evolution. During the electrochemical studies it was found that the FeS_2 material was reactive with all the alkali-metal ion and undergoes similar two-phase reaction mechanism. Structural analysis demonstrated that the crystallinity of these reacted products decreased as a function of the alkali-metal ion size, with the largest of which, not resulting in a complete reaction after electrochemical reaction. The *in situ* TEM experiments were conducted and show that a sharp reaction front forms in every reaction, and the Fe particle size decreases as the alkali-metal ion size increases. However, despite the larger volume changes associated with the sodium and potassium reaction, fracture only occurred during lithiation. Mechanical testing and chemomechanical modeling demonstrated that this was a result of the shape evolution of the crystal during the reaction, rather than the mechanical properties of the reacted material. The lithiation reaction was highlight anisotropic, producing more substantial mechanical stress than the sodiation or potassiation reaction. These results demonstrate that different reaction pathways influence the fracture behavior of electrode materials.

In Chapter 5, investigation of the fundamental reaction behavior of very small antimony nanocrystals is presented. Using *in situ* TEM, it was shown that sufficiently small antimony nanocrystals spontaneously form uniform voids upon the delithiation of the material, that were then able to be reversibly filled and vacated during cycling. Structural analysis was performed and showed that after the first full lithiation cycle the only crystallinity still present is the result of the Li_2O signal from the formation of a rigid oxide layer. During delithiation this oxide layer was found to remain intact resulting in the

formation of an Sb-rich amorphous coating on the interior of this oxide structure as the lithium was removed. This void formation was also found to be a result of the initial particles size and shape as this behavior was not seen in larger, more irregularly-shaped particles that underwent the same reaction. Electrochemical tests were then conducted on the small uniform Sb nanocrystals, the larger more irregular Sb nanoparticles and bulk Sb powder. These tests showed that the nanocrystals exhibited very stable behavior after the initial formation of the oxide layer structure. A simple chemomechanical model was then developed to explain the formation of these voids within the oxide shells that was analogous to a thin-walled pressure vessel. This model demonstrated the balance of internal strain energy that is developed during delithiation and the associated strain that accompany this reaction while taking the buckling stress of the external oxide shell into account. This model also provides insight into the development of other large-volume-change materials that could possibly benefit from this type of natural voiding behavior as a result of the formation of an oxide shell.

In Chapter 6, I present a summary of the collective results of the studies conducted during the study of these large-volume-change materials. The significance of the results of these studies are explored, as these conversion and alloying-type materials are investigated as promising electrode materials for Li-, Na-, and K-ion battery systems. Future work into various factors of both these materials systems and others like them are discussed in order to engineer these materials for use in next generation batteries.

CHAPTER 2. EXPERIMENTAL TECHNIQUES

In this chapter the experimental procedures used to gather data are described. In this dissertation work several different types of experiments were conducted. These included the synthesis of the nanoparticles needed for electrochemical experiments along with various characterization techniques, including X-ray diffraction (XRD) and transmission electron microscopy (TEM). Of these experiments, the primary amongst them were the use of electrochemical and *in situ* TEM techniques. By combining these types of experiments, direct links can be made from the changes observed on the nanoscale to the electrochemical behavior seen in coin-cell battery setups.

2.1 *In Situ* Transmission Electron Microscopy

The primary experimental characterization technique used throughout these studies is transmission electron microscopy. Modern TEM allows for high spatial-resolution imaging of samples along with the ability to characterize materials using a variety of techniques. These include electron diffraction, energy dispersive spectroscopy (EDS), and electron-energy loss spectroscopy (EELS). For the work done in this dissertation, electron diffraction and EDS were primarily used for *in situ* characterization. If properly used, these techniques combined with the imaging capabilities allow for atomic-scale structural, chemical and morphological characterization.

The TEMs used for these experiments all operate by transmitting a high-energy electron beam (200-300 kV) through a sample that is less than a few hundred nanometers thick.[80] This transmitted beam is then used to form a real-space image or diffraction pattern.

In TEM, contrast is dependent on several factors. The first is mass-thickness contrast, where heavier atoms and thicker regions scatter more electrons and results in lower intensity in a bright-field image. The second is diffraction contrast which is the result of the crystallinity of the imaged sample and is therefore not observed in amorphous materials. This change in contrast results from the scattering that occurs at high angles of electron diffraction from a lattice. The final type of contrast is phase contrast which results from the atoms diffracting electrons in the beam as they pass through them. This results in the relative phase of the electrons changing upon transmission through the imaged sample and the associated contrast from this phenomenon allows for high-resolution imaging of a crystal lattice. The high-resolution imaging made possible by TEM make it the ideal characterization tool for studying the crystal structure, morphology and chemical composition of various nanomaterials.

To make use of these TEM capabilities several experimental methods have been developed to observe dynamic processes *in situ*. While these techniques have revealed a great deal of phenomena,[25,81–86] these experiments remain very difficult due to several factors such as the high vacuum environment within the microscope chamber. In addition, these experiments require precise and complicated sample holders along with complex sample fabrication techniques. However, despite these difficulties *in situ* TEM has previously been utilized to examine the dynamic structural and morphological changes in various battery electrode materials while undergoing electrochemical reaction. This technique was first used by J. Y. Huang and C.-M. Wang et. al. in 2010 to examine the lithiation and delithiation of SnO_2 nanowires using ionic liquid electrolyte and bulk lithium cobalt dioxide cathode. This study demonstrated the lithiation-induced volume expansion

and pulverization of the electrode materials and was one of the first to provide insight in the mechanistic design needed for batteries making used of these materials.[85] This technique has since been modified for use with other types of samples both making use of ionic liquid electrolytes as well as all-solid-state open-cell configurations used in these following experiments. In more recent years, a variety of studies have been conducted on the electrochemical lithiation of various battery nanomaterials and the resulting structural and chemical changes accompanying these reactions.[19,25,30,87–89] These various types of experiments have been made possible by the use of a specialized *in situ* TEM holder, seen in Fig. 2.1, that allows for the probing of various battery nanomaterials with any alkali metal. The procedure to use this type of open cell probing/biasing holder for electrochemical cycling is described as follows.

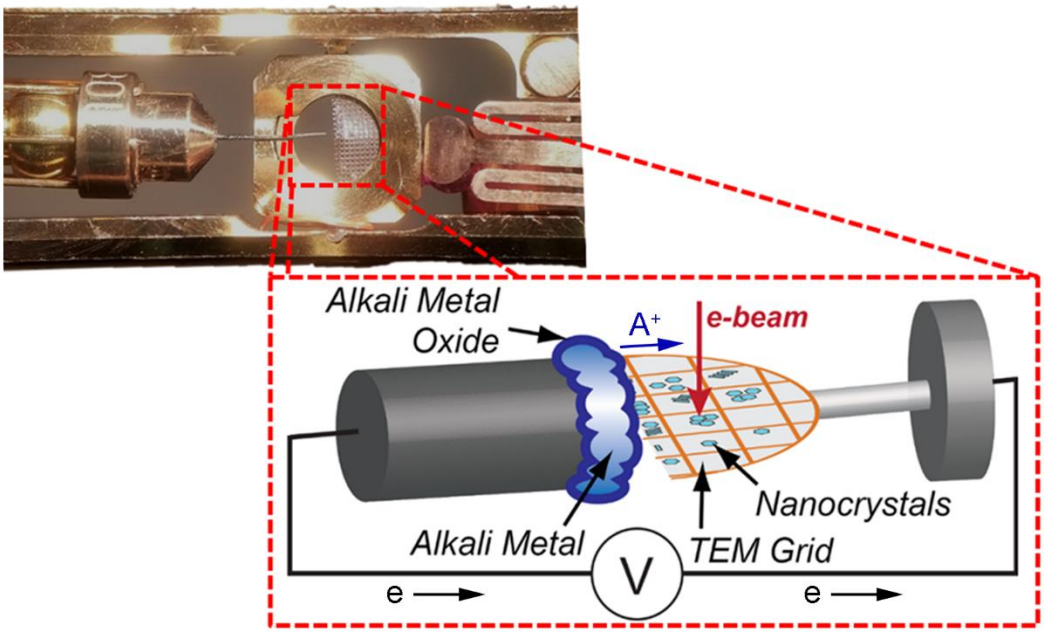

Figure 2.1: *In situ* TEM holder with the piezo-controlled cap and TEM half-grid. A schematic of the open cell probing/biasing *in situ* TEM holder experimental setup that

consists of the alkali-metal tipped tungsten probe as the counter electrode and the drop-cast nanocrystals as the active electrode.

This holder operates through the use of two probes; on one end is a piezoelectrically-controlled tungsten probe and on the other is a copper TEM half-grid with the tested nanomaterial dispersed on it. After coating the tungsten probe in the appropriate alkali metal in an argon-filled glove box, it is affixed to the piezo-controller and attached to the specimen holder. During the transfer of this probe to the holder, the alkali metal is shortly exposed to air, causing a thin oxide, hydroxide and/or nitride layer (~50 nm) to form at the surface of the metal, as labeled in Fig. 2.1. Once inserted into the TEM, the tungsten probe is then either contacted to the carbon film near a cluster of the nanoparticles being tested or directly contacted to the active material itself. A bias can then be applied between the copper TEM grid and the tungsten probe, which drives the alkali metal ions through the oxide/hydroxide surface layers that act as a solid electrolyte and causes them to be reduced on the carbon grid or tested nanomaterial allowing for the nanoparticles reaction with the alkali metal of choice.[30,85,87] To induce the initial reaction a bias between –2 V and –3 V was applied to the gride with respect to the probe. Where applicable, to reverse the reaction a bias between +2 V and +3 V was applied. Previous work has shown that this provides a similar situation to the reaction process that these materials undergo in a conventional battery.[30,88,89] The current is typically not measured in nanoparticle experiments due to the small changes associated with only a small number of the active material reacting relative to what would be seen in typical electrochemical experiments, however the full reaction of these materials combined with *ex situ* TEM experiments generally confirm similar reactions are taking place. The experiments discussed in this

dissertation have been conducted with an FEI NanoEX 3D STM/TEM specimen holder that allows for this physical manipulation of nanoscale samples and electrical biasing. TEM experiments were performed at both Georgia Tech on an FEI Tecnai F30 as well as at the Center for Nanophase Materials Science (CNMS) at Oak Ridge National Laboratory on a FEI Titan S 300kV S/TEM as a part of the user program and then during my time working at CNMS under the Department of Energy Office of Science Graduate Student Research Award from January 2019 to July 2019 working on the antimony nanocrystal lithiation experiments..

After each of the *in situ* TEM experiments a series of image analysis techniques were conducted. These methods were employed to obtain accurate physical and structural information from the large amount of visual data collected while recording the *in situ* TEM experiments. The first technique employed was the use of image software to extract structural information from high-resolution TEM images. This was done using fast-Fourier transforms (FFTs) of a single TEM images. Fourier analysis converts signals from the original image and decomposes them into components of different frequencies.[90] In the context of a TEM image, its Fourier transform is effectively a constructed diffraction pattern as the frequencies from the image correspond to the crystalline planes seen in the image and can therefore be used to determine the structure of the imaged material. Additionally, these points can be isolated and an inverse FFT can be constructed from this resulting pattern can be made, which can be applied as a mask to the original image (examples of this can be seen in Figures 3.13f and 4.6b).

Size and distribution of various particles was also information needed throughout every experiment to determine the volume expansion, reaction rates and the size and shape

effects. For every set of experiments this was done through optimizing the contrast for each image. Generally, for these experiments the metal particles being studied had the darkest contrast compared to the alkali-metal phase. This allowed for automated processes to apply a contrast threshold to the image to binarize the image which allowed for accurate measurements of the physical size, shape and structure of the reacted products. For some specific cases contrast correction was not enough and segmentation of processed images was needed to get accurate measurements. This was done through the use of a trainable segmentation tool within the ImageJ image analysis software.[91] This allowed for the physical selection of areas of pixels that matched different phases within the image and assigning a "class" to them in the software. For example, a class would be the dark contrast metal particle or the vacuum/carbon background. The software then segments the rest of the image based on the manual selections. Based on each classifier, the probability that each pixel belongs to one of these defined "classes" is determined and is displayed on a 32-bit hyperstack. The resulting probability maps can then be filtered of noise and binarized, leaving just the segmented particles that can be examined. This technique was employed in Chapter 5 (Fig. 5.5) to determine the exact volume remaining after several cycles of the material. These types of image analysis techniques allow for a great deal of valuable information to be gather from a single *in situ* TEM experiment.

2.2 Electrochemistry

Traditional electroanalytical methods were used to determine the electrochemical behavior of the tested materials and to make comparisons to the nanoscale reactions that

will be examined using TEM. Galvanostatic electrochemical discharge tests were performed on a LANDT Battery Testing System or a BioLogic VMP-3 potentiostat. The shapes of the galvanostatic curves and hysteresis between charge and discharge were then used to inform further testing of the various materials. Electrochemical impedance spectroscopy (EIS) was performed to determine the internal impedance of the constructed half-cells at different points during cycling. Cyclic voltammetry (CV) was also performed by sweeping the potential of the working electrode at constant rates. From these voltammograms, the differences in the redox reaction of the active materials with different alkali metals were determined.

The electrochemical data was gathered using conventional CR2032 stainless-steel coin cells with working electrodes made of active materials being studied. These electrodes were prepared by creating a powder mixture of a polymer binder, generally polyvinylidene difluoride (PVDF) or sodium carboxymethyl cellulose (CMC), carbon black and the tested active material. These mixtures were then mixed either in a vial with *N*-Methyl-2-pyrrolidone (NMP) solvent or using a ball mill and deionized water. Slurries were then spread on cleaned copper foil using a custom-made doctor-blade apparatus set to spread an even 10-15 μm thick electrode. The slurry-covered copper foil was then placed into a vacuum oven and heated under vacuum. Once dried the electrode disks were then punched out and calendared using a roll press. Coin cells were then constructed using lithium, sodium, or potassium metal as the counter/reference electrode. All the alkali metals were cleaned of all surface contamination in an argon-filled glove box by scraping with a polytetrafluoroethylene block before assembling the coin cell. Each cell used a glass microfiber disk and a polymer separator film (Celgard) soaked in the appropriate

electrolyte. Specific procedures followed for each electrochemical test of Cu_2S, FeS_2 and Sb will be explained in the following chapters.

2.3 Materials Synthesis

Several synthesis methods were used to make the nanoparticles tested. The synthetic methods conducted here at Georgia Tech all made use of a Schlenk line that allows for synthesis under either nitrogen or air.

Copper(I) sulfide (Cu_2S): The Cu_2S nanocrystals used in Chapter 3 were synthesized using a high-temperature pyrolysis reaction procedure.[92] A mixture of 3 mmol copper(II) acetylacetonate, 10 mL 1-dodecanethiol, and 20 mL oleylamine is degassed with nitrogen for half an hour in a three-neck round-bottomed flask. This solution is then heated to 250 °C slowly and held at this temperature for an hour to form the Cu_2S nanocrystals. The nanocrystals were then precipitated in ethanol and then cleaned in a mixture of ethanol and toluene before being dispersed in toluene.

Iron (II) Disulfide (FeS_2): The FeS_2 nanocrystals used in Chapter 4 were made using the following synthesis procedure. This synthesis made use of a two-step solution-based heating process is used.[93] The nucleation of iron (II) disulfide is done using a mixture of 10 g hexadecylamine, 96.2 mg sulfur, and 83.4 mg anhydrous $FeCl_2$ beads degassed with nitrogen gas in the Schlenk line. The mixture was slowly brought to and held at 250 ºC for 3 hours while stirring at 240 rpm. The mixture was then allowed to cool to room temperature and solidify. For the growth of FeS_2, 15 mL oleylamine, 65.7 mg sulfur, and 126.8 mg $FeCl_2$ will then be added to the frozen mixture. The flask was sealed and slowly

brought to and held at 200 ºC for 9 hours while stirring at 750 rpm, after which the mixture was allowed to cool to room temperature and solidify once again. To clean the FeS_2 nanocrystals, the mixture was slowly reheated to 50 ºC, and 30 mL chloroform (anhydrous) was added. Centrifugation of the final cooled mixture was performed for 2 minutes at 3000 rpm. The nanocrystals were cleaned twice more using chloroform in a dispersal and centrifugation process, and the final product was dispersed in chloroform and used for *in situ* TEM tests.

Antimony (Sb): Antimony nanocrystals used for the experiments in Chapter 5 were synthesized to be two different average sizes for the *in situ* TEM. Most experiments investigated particles with a diameter of 15.7 ± 2.5 nm, with the spread denoting the standard deviation (Fig. 5.1). For the *in situ* TEM experiments that involved larger materials, particles of non-uniform shape and size with a diameter of 33 ± 8 nm were synthesized and used (Fig. 5.11). This synthesis was performed by our collaborators from Vanessa Wood's group at ETH Zurich.

In a typical synthesis of the smaller Sb nanocrystals, 10 mL of oleylamine was loaded into a three-neck flask and connected to a vacuum manifold setup *via* a condenser. The flask reactor was then heated to 100 °C under vacuum to remove water residues and air. Meanwhile, three injection mixtures were prepared in air-free glove boxes: Mixture 1 was a solution of $LiN(SiMe_3)_2$ (0.364 g) in dried 1-octadecene (3 mL); mixture 2 was a solution of $Sb(NMe_2)_3$ (43.4 µL) in dried 1-octadecence (1 mL); and mixture 3 was a 1.0 M solution of $Li(C_2H_5)_3BH$ in tetrahydrofuran (0.1 mL). After 1 h of oleylamine purification, the reaction flask was heated to 200 °C, at which the three injection mixtures were sequentially added with a time interval of 10 s between injections. The reaction flask

turned brown after injection of reducing agent (the $Li(C_2H_5)_3BH$ superhydride solution), indicating fast nucleation of Sb nanoparticles. The growth of Sb nanoparticles was allowed for 30 min at 200 °C, after which the reaction mixture was cooled to room temperature with a water bath. Sb nanoparticles were purified with a typical solvent-nonsolvent protocol, adding chloroform and ethanol, followed by centrifugation and decantation. This purification cycle was repeated three times, and small amounts of oleic acid were then added to replace weakly-bonded oleylamine ligands. Finally, Sb nanocrystals were re-dispersed in chloroform, forming a stable colloidal solution.

To prepare the larger Sb nanoparticles, the synthesis described above was modified to reduce the nucleation rate and to enhance the growth of Sb nanoparticles. To reduce the nucleation rate, mixture 3 (a solution of reducing agent) was eliminated from the recipe. Mixture 2 was injected twice (10 s after mixture 1 and also after 15 min of growth of Sb nanoparticles) to enhance growth due to the presence of greater quantities of precursor for longer times. Furthermore, the reaction conditions were set to a higher temperature (280 °C) and a longer time (1 h) to trigger Ostwald ripening mass transfer. All other conditions were identical to the conditions for small nanocrystal synthesis.

2.4 X-ray Diffraction

Ex situ and *in situ* X-ray diffraction was vital for this research to determine the overall phase evolution of the active materials. *In situ* XRD was used to study battery electrodes during reaction with the alkali ions, while *ex situ* XRD was used to confirm that the expected reaction had occurred. X-ray diffraction is caused by the elastic scattering of

x-rays by atoms in a periodic lattice, as can be seen in Figure 2.2. The scattered monochromatic x-rays from this structure that are in phase with each other lead to the constructive interference. This develops a pattern that corresponds to the lattice spacings which can be derived using Bragg's law which is defined as,

$$2d \sin\theta = n\lambda \qquad \text{(Eq. 2.1)}$$

where d is the spacing between diffracting planes, θ is the incident angle, n is an integer called the order of reflection, and λ is the wavelength of the incident x-ray beam. Using this d-spacing, and pre-existing knowledge of what elements would be present, the structure of the tested material can be determined through the use of an extensive international database made by the International Center for Diffraction Data (ICDD). Reference files from this service were used in order to characterize the synthesized materials as well as the reaction products of the experiments performed throughout the following studies.

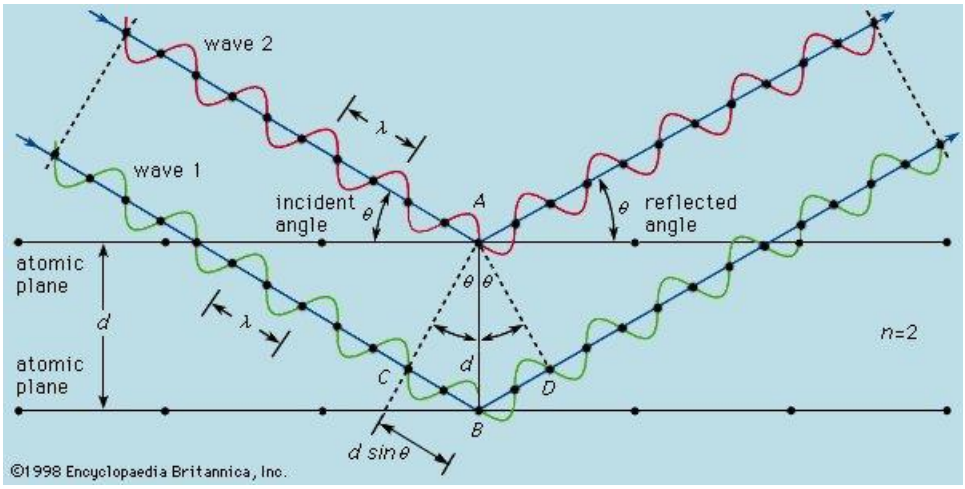

Figure 2.2: Schematic representation of Bragg's Law with the incident beam coming from the upper left of the frame. This figure was taken from reference[94].

XRD scans for the following experiments were generally performed using a PANalytical Empyrean instrument with a Cu Kα radiation source ($\lambda_{K\alpha 1}$ = 1.54 Å), unless otherwise stated in the following chapters. For *ex situ* experiments, after lithiation, sodiation, or potassiation, electrodes were removed from their coin cells and rinsed with the appropriate solvent in an Ar-filled glove box. The electrode material was then scraped from the copper metal foil onto a glass slide and covered by a thin Mylar layer to avoid atmospheric exposure during the X-ray experiment. This Mylar layer allowed for the transmission of the X-rays with minimal signal damping outside of the large peak seen at $2\theta = \sim 26°$.

CHAPTER 3. DISTINCT NANOSCALE REACTION PATHWAYS IN CONVERSION BATTERY MATERIAL

3.1 Introduction

As discussed in Chapter 1, new materials need to be developed in order to satisfy the growing demand for cost effective battery system with long cycle life and high energy density.[1–6] Previous research has looked at using high-capacity electrode materials, such as conversion-type Cu_2S with a theoretical specific capacity of 335 mAh/g, to replace current materials. Additionally, this material is reactive with sodium, which lowers the cost of the full battery cells made of this material by substituting aluminum for copper current collectors. In this study, which was published in the Journal of Materials Chemistry A in 2017, *in situ* TEM and *in/ex situ* XRD combined with *ex situ* electrochemical methods revealed the nanoscale-to-macroscale transformation mechanisms of Cu_2S with Na.[25] During the slow sodiation, Cu_2S was observed to form a continuous Na_2S phase with Cu metal particles contained within the Na_2S phase. It was found that the larger associated volume changes associated with the sodiation of Cu_2S nanocrystals induces a different reaction pathway to occur when compared to lithiation. This different resulting morphology was found to not cause accelerated capacity decay when used in standard electrochemical cells. This result of a stable Na/Cu_2S battery emphasizes the importance of understanding the detailed reaction mechanisms and morphological evolution of electrode materials in different alkali-metal batteries, which is critical for the engineering of high-capacity batteries with long cycle life.

3.2 Cu_2S Electrochemistry

3.2.1 Comparison of Li vs Na Cells

Metal sulfide materials are an attractive class of electrode materials for Na-ion batteries. The higher standard electrochemical potential of the Na/Na^+ redox couple compared to the Li/Li^+ couple makes some sulfides more appropriate as anode materials in Na cells compared to Li cells.[45,95] Pyrite FeS_2 has recently been shown to exhibit excellent cycle life and high capacity in Na cells, especially when using glyme-based electrolytes.[70–72,96] Cu_2S has demonstrated good reversibility in Li cells (>150 cycles with negligible capacity decay),[28] but only limited cycle life in Na cells (~20 cycles).[62] Thus, Cu_2S has been selected as a model material for examining fundamental reaction mechanisms with both Na and Li in an effort to determine the direct reason for this difference in electrochemical stability.

Preliminary electrochemistry data can be seen in Fig. 3.1 showing the difference in behavior of the Cu_2S material during electrochemical reaction with Li and Na. Electrodes were prepared using 80 wt% Cu_2S, 10 wt% SuperP conductive carbon, and 10 wt% polyvinylidene difluoride (PVDF) binder mixed in *N*-Methyl-2-pyrrolidone (NMP) solvent and applied to copper foil. In Fig. 3.1a, the galvanostatic curves show the initial discharge and charge of the Cu_2S/Li and Cu_2S/Na cell, and Fig. 3.1b and c show cyclic voltammograms from the Li and Na half cells. The curves in Fig 3.1a. are plotted with different potential scales with respect to the standard potentials of Li/Li^+ (-3.04 V vs. SHE) or Na/Na^+ (-2.71 V vs. SHE). Both ions are expected to exhibit a theoretical specific capacity of 335 mAh/g, if both cases undergo the following reaction,

$$Cu_2S + 2X^+ + 2e^- \rightarrow X_2S + 2Cu \qquad \text{(Eq. 3.1)}$$

where X is the alkali metal in the half-cell. The Na/Cu_2S initial discharge capacity was higher than this theoretical specific capacity due to the formation of a solid-electrolyte interphase layer that occurred at the lower potentials of the sodium half-cell. During the initial cycle the different shapes of the Cu_2S/Li and Cu_2S/Na galvanostatic curves in Fig. 3.1a indicate different reaction mechanisms. The shape of the lithiation galvanostatic curve shows a long, flat plateau during discharge and then two plateaus during charge (the higher plateau generally associated with the CuS/Li reaction), while the cell undergoing sodiation shows two moderately sloping regions during discharge and a charge curve with multiple steps. These differences in the initial cycle can be further seen in the differences of the peaks seen in the cyclic voltammetry (CV) plots in Fig. 3.1b and c, where the Li/Cu_2S CV shows sharper peaks associated with the flatter plateaus observed in their discharge/charge curves.

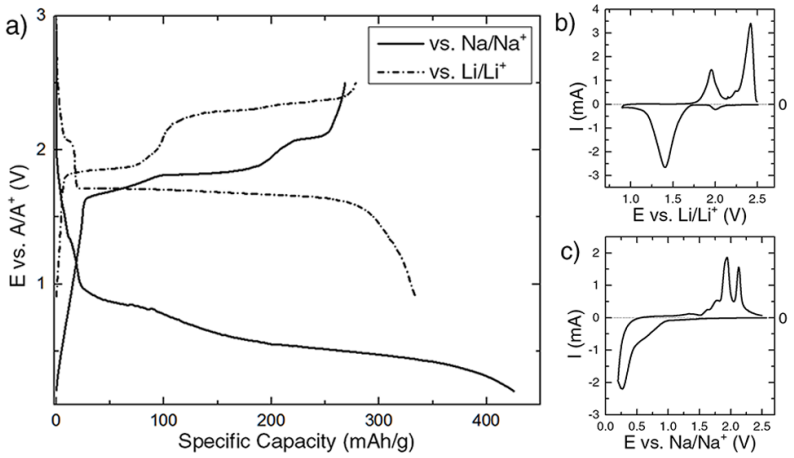

Figure 3.1: (a) Galvanostatic curves for the Cu_2S electrodes in Na and Li half cells during the first cycle at a slow C/20 rate (full charge or discharge in 20 hours). **(b and c)** Cyclic

voltammograms of the first cycle of the Li/Cu_2S half cell (b) and the Na/Cu_2S half cell (c), with a voltage sweep rate of 0.1 mV/s.

From past work on the lithiation of Cu_2S, it is known to undergo a displacement reaction, which is a conversion-type reaction.[19,26,27] In this reaction, the inserted Li^+ displaces the Cu^+ ions, expelling them to the surface where they are reduced to Cu metal which results in a mixture of Li_2S and Cu metal.[26] The overall crystal structure undergoes only minor changes during this process. This reaction is enabled by several factors: (i) the low chalcocite crystal structure of Cu_2S (which consists of a hexagonal sulfur sub-lattice with Cu^+ ions distributed throughout[59–61]) is very similar to the Li_2S structure, (ii) the Cu_2S and Li_2S phases have similar molar volumes with a difference of only ~2.7% volume, (iii) and the ionic conductivities of Li^+ and Cu^+ in the Cu_2S structure are very high (~10^{-7} cm^2 s^{-1}).[19,28] Previous *in situ* studies on the lithiation of Cu_2S by McDowell et al. showed that the exact morphology of the Cu_2S is maintained as it transforms to Li_2S through this displacement-type reaction.[19] This is unique because most sulfide materials' initial crystal structure is destroyed during reaction, resulting in a nanoscale phase-separated mixture. The fast ion diffusion associated with the displacement reaction is thought to contribute to the low hysteresis seen in the lithiation case. Meanwhile, in the Na/Cu_2S system the galvanostatic curves show a much more substantial hysteresis further suggesting that a different reaction mechanism is taking place.

3.2.2 Cycling Behavior of Cu_2S/Na

Examination of the electrochemical cycling behavior of a typical Na/Cu_2S cell showed outstanding cyclability in an electrolyte of 1.0 M $NaPF_6$ in diglyme solvent. Figure 3.2a shows that the Cu_2S electrode in a Na cell was stable for >400 cycles, which is superior to any previously reported copper sulfides for Na-ion batteries. After around 300 cycles, the coulombic efficiency (CE) increases beyond 100%, which could be the result of the shuttle effect which has commonly been observed in lithium-sulfur batteries.[97] The shuttle effect is mainly caused by the dissolution and then migration of polysulfide in the organic liquid based electrolyte during cycling, all of which then leads capacity fade over time.[98] However, since the CE remains near 100% for hundreds of cycles suggests that this effect is not a major factor. From Fig. 3.2b, the galvanostatic charge/discharge curves for the 1st, 2nd, 10th and 20th cycles show that the curves change shape over the first few cycles before settling around the 10th cycle. This indicates that the reaction processes change initially as the specific capacity levels out to ~270 mAh/g. Fig. 3.2c shows that the electrochemical behavior was also found to be consistent over different cycling rates. Even at the relatively fast discharge rate of 1C most of the capacity is retained.

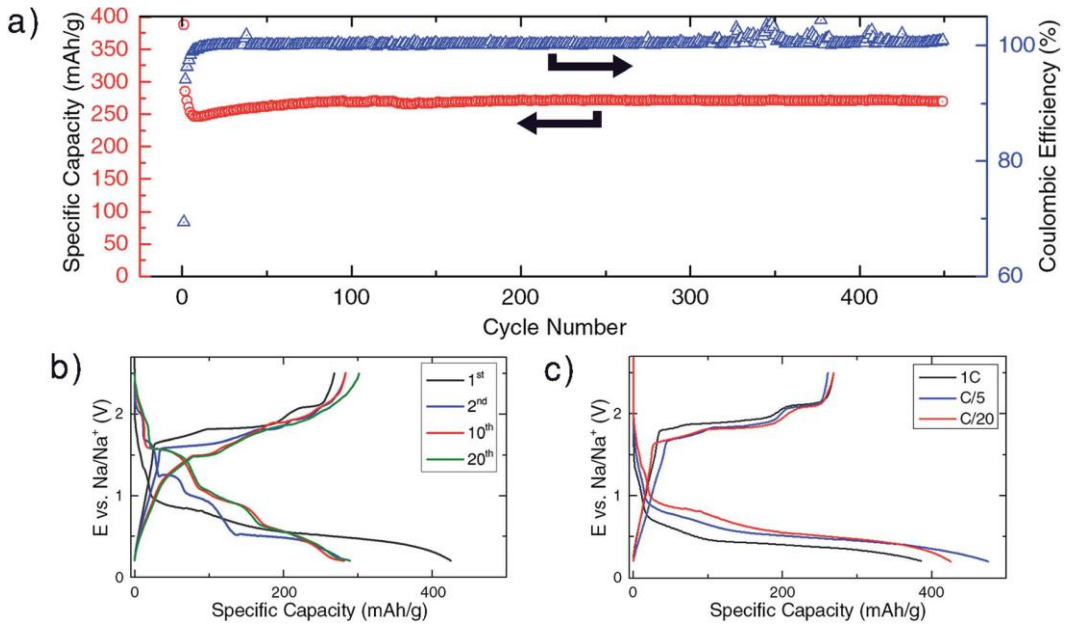

Figure 3.2: (a) The specific capacity (red) and coulombic efficiency of a Na/Cu_2S half-cell undergoing galvanostatic cycling at a rate of 1C. **(b)** The discharge curves of the 1st (black), 2nd (blue), 10th (red) and 20th (green) discharge/charge curves tested at C/20. **(c)** Cycling rate tests at 1C (black), C/5 (blue) and C/20 (red).

3.2.3 Effect of Different Electrolytes on Cu_2S Electrochemistry

A comprehensive study was also performed on various types of electrolytes used for both the Na/Cu_2S and Li/Cu_2S based on what has been used in other systems. In the first attempt it was found that Na/Cu_2S cells using monoglyme solvents exhibit good cyclability which can be seen in Fig. 3.3. However, using a carbonate electrolyte (EC/DEC) common for Li-ion batteries, the cycling stability seen in Figure 3.4 was significantly diminished as the battery experiences significant capacity decay by just the fifth cycle.

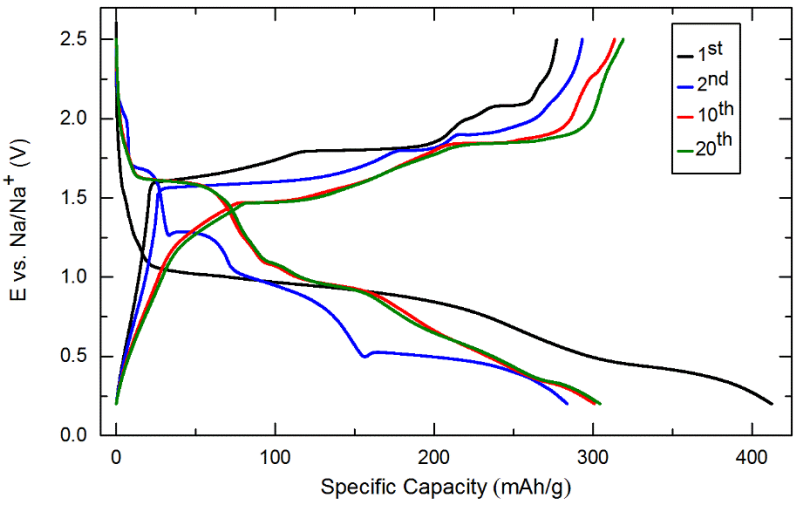

Figure 3.3: Galvanostatic discharge/charge curves of a Na/Cu_2S cell with an electrolye consisting of monoglyme solvent with 1.0 M $NaPF_6$ salt at a rate of C/20.

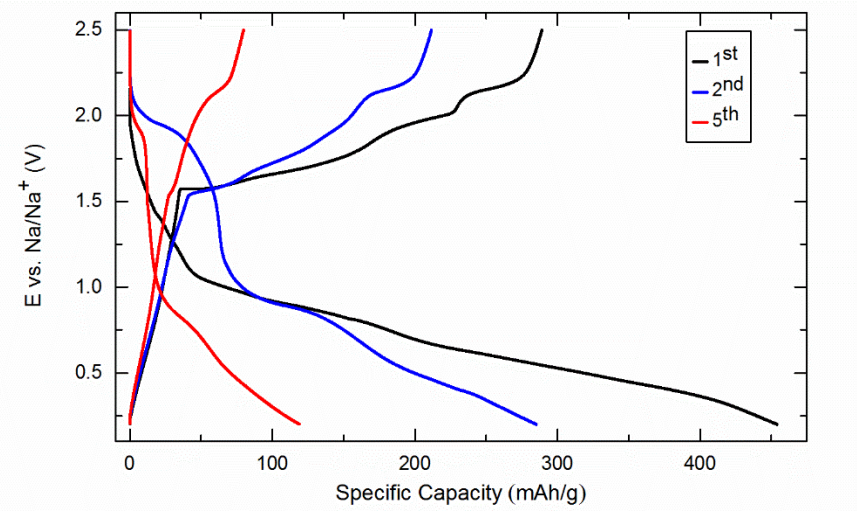

Figure 3.4: Galvanostatic cycling (the first, second, and fifth cycle) of a Na/Cu_2S cell with EC/DEC solvent and 1.0 M $NaClO_4$ salt at a rate of C/20.

Other recent work has shown that ether-based solvents (such as the glymes used here) also allow for outstanding cycle life of other Na-ion battery materials, including FeS_2

and Na metal.[64,70,96,99–102] This is thought to be due to the protective nature of the solid-electrolyte interphase (SEI) layer formed when using glyme solvents and Na salts.[100] Although almost all previous studies of Cu_2S cells with either Li or Na have shown capacity decay with cycling,[103] one recent report on Li/Cu_2S cells using a mixed dioxolane/monoglyme electrolyte showed excellent cycle life (>150 cycles with negligible capacity decay).[28] The following data in Figures 3.5 confirms that the use of this dioxolane/monoglyme electrolyte in Li/Cu_2S cells (Fig. 3.5) also enhances cycle life when compared to the EC/DEC electrolyte (Fig. 3.6). It is shown here that unprecedented cycling stability can also be attained during cycling of Na with Cu_2S when using ether-based (glyme) solvents, despite the significant differences in the electrochemical curves.

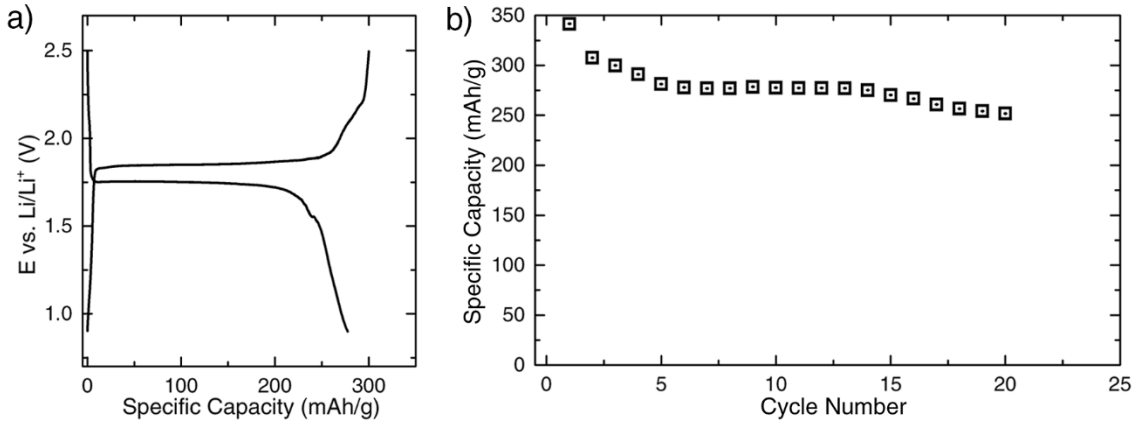

Figure 3.5: Galvanostatic cycling of a Li/Cu_2S half-cell using an electrolyte consisting of 1.0 M LiTFSI in DOL/DME. The cell was cycling at a rate of C/20. **(a)** Discharge/charge curves from the 10th cycle. **(b)** Specific capacity over 20 cycles.

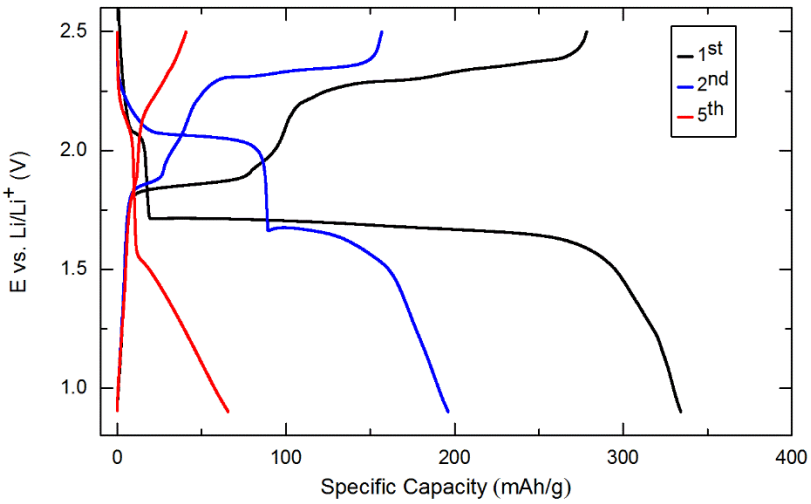

Figure 3.6: Galvanostatic cycling (the first, second, and fifth cycle) of a Li/Cu_2S with EC/DEC solvent and 1.0 M $LiPF_6$ salt at a rate of C/10.

3.3 Phase Evolution of Cu_2S Sodiation

To determine the overall phase evolution of the Cu_2S active material within these electrodes, *ex situ* and *in situ* X-ray-diffraction (XRD) was utilized for both Na/Cu_2S and Li/Cu_2S cells.

3.3.1 *Ex Situ* XRD of Na/Cu_2S and Li/Cu_2S

Fig. 3.7 shows *ex situ* XRD traces of pristine Cu_2S which corresponds to the Bragg peaks of the low chalcocite Cu_2S and djurleite $Cu_{1.97}S$ phases, which both have monoclinic structures. These phases are often found intermixed and have similar crystals structures and diffraction patterns due to both featuring a hexagonal-close-packed sulfur sublattice, with different interstitial copper ordering.[59] In Fig. 3.7a, a scan of a fully lithiated Cu_2S

electrode was taken and the Bragg peaks corresponding to Cu metal and Li_2S can clearly be seen with minor peaks from Li_2O and unreacted Cu_2S, as previously reported.[103] Other oxide and sulfide materials that undergo conversion-type reactions with lithium often form very small metal crystals, usually less that ~5 nm in diameter, upon full reaction.[19,31,104] Particles this small are generally difficult to detect with standard XRD, indicating that the intense Cu Bragg peaks are the result of the formation of relatively large metal Cu crystals in the electrode.

Meanwhile the *ex situ* XRD scan of the sodiated Cu_2S half cells can be seen in Fig. 3.7b. The scan clearly shows Cu peaks along with Na_2S peaks that are convoluted with peaks of other phases such as Na_2O. These lower intensity peaks are an indication of poorly crystalline and/or small crystallite size. These scans indicate that, while the sodiated product shows lower relative intensity, the reacted products of each case are similar. Cu_2S electrodes in both Li and Na cells undergo phase transformations that result in a similar alkali metal sulfide and copper metal.

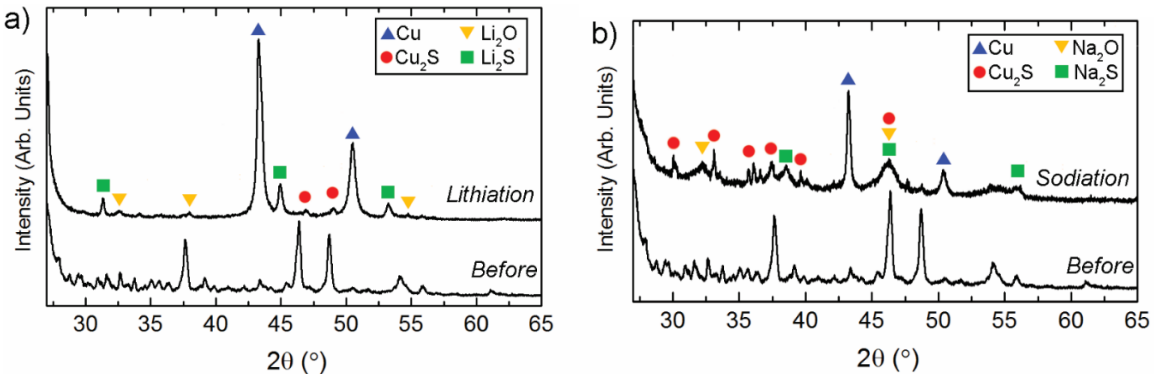

Figure 3.7: *Ex situ* XRD of Cu_2S/Li **(a)** and Cu_2S/Na **(b)** half cells showing the (111) and (200) Cu Bragg peaks after reaction. The partially visible large peak at $2\theta = \sim 26°$ is a result of the polymer cover used for these scans. In both (a) and (b) the "Before" plot was

confirmed to be primarily made up of the low chalcocite phase (JPCDS no. 04-007-1284), with a minority component of djurleite (JPCDS no. 00-023-0959).

3.3.2 *In Situ* XRD of Na/Cu_2S and Li/Cu_2S

To further investigate the phase transformation mechanisms during the beginning of the discharge process, *in situ* XRD was carried out using a laboratory X-ray instrument and the resulting scans can be seen in Figure 3.8a and b. These experiments were performed with a Bruker D8 Advance X-ray Diffractometer that uses a beryllium window that allows for X-ray transmission. The Cu_2S electrodes were fabricated on Al current collectors rather than Cu for these tests, since the growth of Cu within the electrode was intended to be measured using these experiments. Let it be known that the *in situ* XRD electrochemical cells exhibited similar discharge potentials and shapes, but the specific capacity values were lower (~175 mAh/g, Fig. 3.8c and d). The Li cell also featured a longer initial plateau at ~2 V vs. Li/Li^+ (above the primary plateau), during which the Bragg peaks of Cu_2S did not change (this was likely caused by more substantial side reactions in this *in situ* cell).

Figure 3.8a and b show a small portion of the XRD traces collected during the lithiation and sodiation, respectively. This region of the XRD traces contains two peaks associated with Cu_2S peaks, a large peak associated with the Al foil current collector, along with the Cu {111} peak that grows during discharge. From these *in situ* XRD experiments the key finding is that the Cu_2S peaks in both the Na and Li cells start to shift to lower 2θ values near the beginning of the reaction process. This shift suggests intercalation of Na^+ and Li^+ ions within the Cu_2S structure which slightly increases the volume. For both Li and Na, this peak shift occurs near the beginning of the reaction, approximately at the potential

of the primary plateau for the Li/Cu_2S reaction (~1.8 V vs. Li/Li^+) and at the beginning of the long sloping region for the Na/Cu_2S reaction (~1.0 V vs. Na/Na^+). The shift of the Cu_2S peaks is followed by a gradual diminishment in intensity, with corresponding growth in intensity of the Cu (111) peak. Thus, it appears that both Na^+ and Li^+ first intercalate into Cu_2S, followed by gradual disappearance of the Cu_2S phase and growth of Cu metal. The intercalation process causes a volume expansion of ~1.5% in both cases. Initial lithium insertion has also been observed to precede conversion reactions in other materials, such as MoS_2 and CuS.[105] It is difficult to detect such a subtle change with *ex situ* XRD alone, and the combination of *ex situ* and *in situ* XRD here is helpful in revealing these transformation processes.

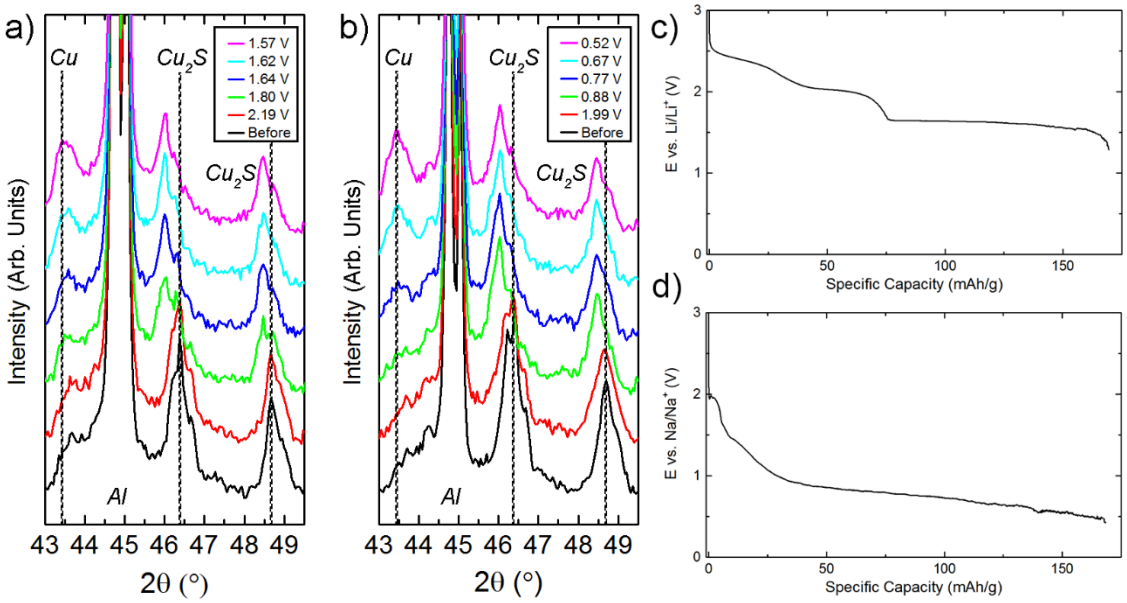

Figure 3.8: *In situ* XRD traces during the initial discharge of **(a)** a Li/Cu_2S half-cell at C/30, and **(b)** a Na/Cu_2S half-cell at C/20. In both cells, the discharge process sees a slight shift of the Cu_2S peaks to lower diffraction angles seen in between the red and green traces, an increase in Cu (111) Bragg peak intensity and a decrease in the intensity of the Cu_2S peaks. **(c)** The initial discharge that is associated with the Li/Cu_2S *in situ* XRD scan seen

in (a). **(d)** The initial discharge that is associated with the Na/Cu_2S *in situ* XRD scan seen in (b).

3.4 Electron Microscopy Analysis of the Cu_2S Reactions

From the previous data the structural changes during the reaction of Li and Na with Cu_2S appear to be quite similar. As stated previously however, it is critical to understand the morphological changes, since the nanoscale morphological evolution and phase distribution can determine the overall reversibility of a reaction in large-volume-change electrode materials.

3.4.1 *Ex Situ* Scanning Electron Microscopy of First Cycle

Ex situ scanning electron microscopy (SEM) was used to examine morphological changes in discharged and charged electrodes, as shown in Figure 3.9 and 3.10. This experiment made use of coin cells cycled to the discharged or charged state, which were then disassembled inside an Ar-filled glove box. The electrodes were then cleaned, mounted onto SEM stubs and loaded into a Zeiss Ultra 60 Field Emission SEM where the imaging was conducted. From these images it can be seen that after discharge, the Li- and Na-reacted electrodes have significantly different morphologies, with the lithiated electrode featuring long, one-dimensional Cu metal structures in addition to larger sulfur-containing particles which are identified using EDS color mapping in Figure 3.10. The sodiated electrodes do not show these dendrite-like Cu structures. These one-dimensional Cu metal structures have been shown to grow during the displacement reaction of Cu_2S

with Li;[26] interestingly, Cu^+ can diffuse between neighboring Cu_2S particles to form these dendrite-like Cu crystals.[19] The lack of such structures in the sodiated electrode again suggests that Cu_2S is sodiated via a different reaction process.

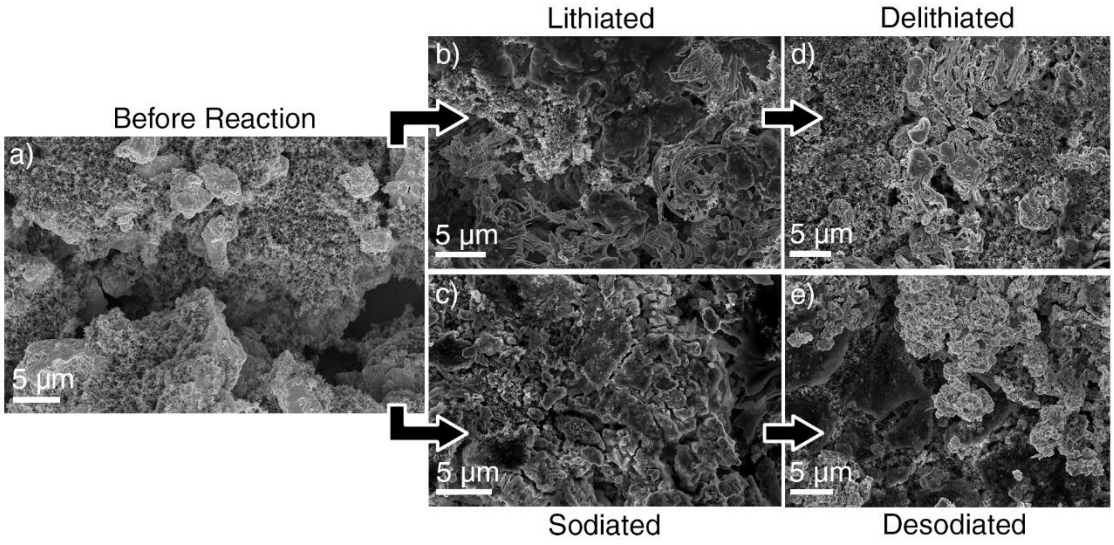

Figure 3.9: *Ex situ* SEM images of Cu_2S electrodes in the pristine state **(a)**, after discharge in lithium **(b)** or sodium **(c)** cells, and after charge in lithium **(d)** or sodium **(e)** cells.

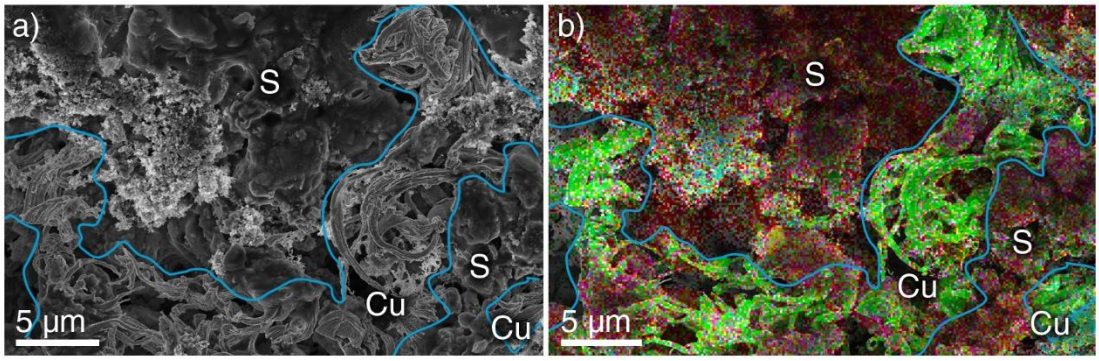

Figure 3.10: (a) Magnified SEM image of the lithiated Cu_2S electrode from Figure 3.9b. **(b)** The same image colorized with EDS signal emitted from different parts of the sample. Red corresponds to sulfur EDS signal, and green corresponds to Cu EDS signal. From the

morphology and the EDS signal, it is clear that the Cu_2S material has phase separated after lithiation.

3.4.2 *In Situ* TEM of Cu_2S Sodiation

The differences of the morphology between the sodiation and lithiation of the Cu_2S were further examined using *in situ* TEM to examine the sodiation process of Cu_2S. In order to perform TEM experiments, electron transparent Cu_2S nanocrystals were synthesized using the process discussed in Chapter 2.3. The *in situ* TEM experiments were performed using the procedure previously discussed in Chapter 2 using Na metal coated with an oxide/hydroxide layer was attached to the one probe.[15,88] Figure. 3.11a-d show snapshots from a video of a group of Cu_2S nanocrystals undergoing sodiation. In this experiment the nanocrystals near the Na probe react first, and the sodiation reaction front travels further with time as the Na diffuses along the carbon grid. Sodiation of these particles causes the formation of Cu metal (the darker phase) and Na_2S (the lighter phase dispersed throughout). These phases were confirmed through the use of selected area electron diffraction (SAED). The indexed pattern of this region can be seen in the SAED pattern in Figure 3.11e. Some of the Cu particles are larger than Cu_2S particles, which indicates that Cu^+ ions diffuse through the contacting Cu_2S particles to grow at single locations. This behavior is likely enabled by the known fast Cu^+ diffusion in Cu_2S,[106] and is reminiscent of the growth of Cu nanowires observed after lithiation which was seen in Figures 3.9 and 3.10 and has also been previously observed with *in situ* TEM by McDowell et. al.[19] Most of the Cu_2S particles in these images, however, undergo a local phase separation during sodiation that results in the formation of intermixed Na_2S and Cu on the

nanoscale. Statistical analysis of the Cu particle size after sodiation shows that most of the particles are below ~5 nm in width, but that a substantial fraction of particles exist that are between ~7 and ~50 nm in width, as shown in the histogram in Figure 3.12.

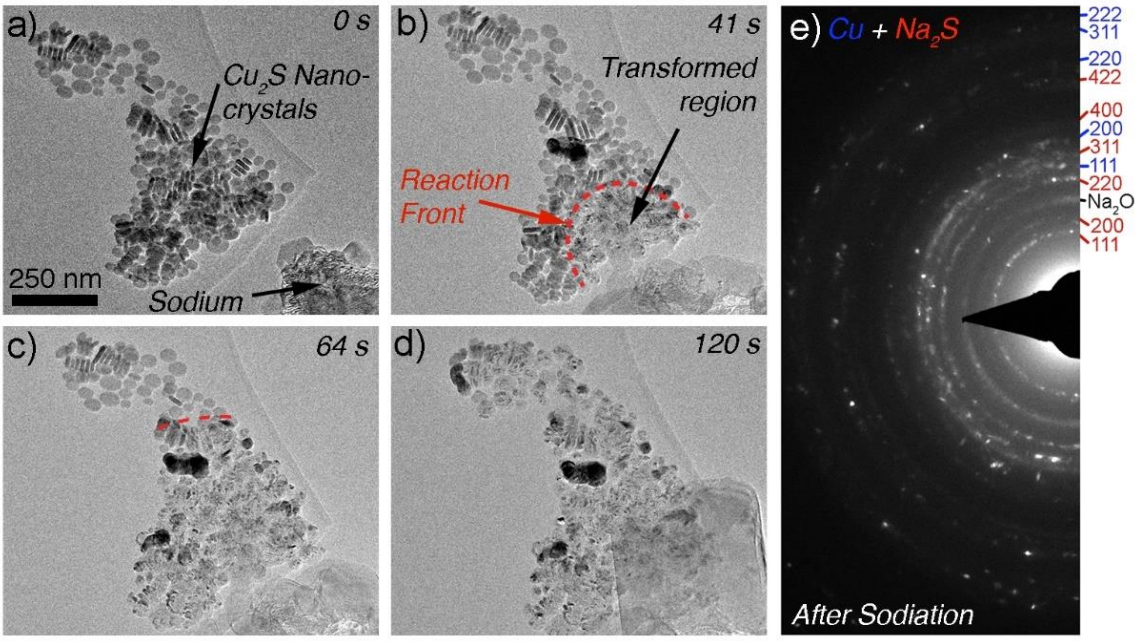

Figure 3.11: (a-d) Snapshots of the sodiation reaction of a group of Cu_2S nanocrystals on a thin amorphous carbon layer. **(a)** Before reaction, the Na/Na_2O is seen at the bottom right of the frame. **(b)** Sodiation has begun at the point of contact, a distinct reaction front (in red) separates the reacted and unreacted material. **(c)** The reaction front continues to move up the group of Cu_2S. **(d)** The entirety of the particle group has reacted, leaving the phase-separated regions of Na_2S and Cu metal. **(e)** The SAED pattern after full sodiation confirms the presence of Cu, Na_2S, and Na_2O (a result of the sodiation of surface oxides).

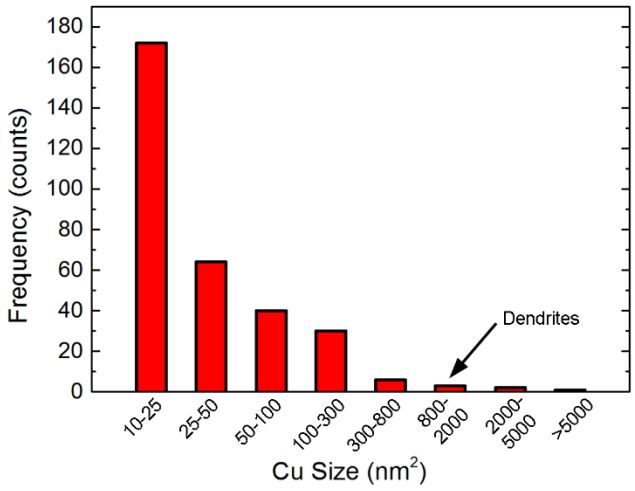

Figure 3.12: Histogram of the measured area of Cu particles after sodiation of the Cu_2S nanocrystals from the data in Figure 3.11.

To examine this transformation at the single-nanocrystal scale, further experiments were undertaken at higher levels of magnification. Figure 3.13 shows a series of images taken from a recording of a smaller group of nanocrystals reacting with Na. These nanocrystals are located further from the Na source than those in Figure 3.11, and therefore Na is introduced more slowly and uniformly into this group of particles comparatively. At the start of the reaction process and thin ~5 nm coating with light contrast grows around all the particles (Fig. 3.13b). After the growth of the outer coating, a small Cu metal particle nucleates and grows to about ~15 nm in diameter on the surface of one of the Cu_2S particles in the upper left region of the frame. At this point, the particles are still not fully reacted. The last step of the reaction process involves the sodiation of the remaining Cu_2S within some of the particles, which causes Cu metal to grow in the particle interior, expanding against the compressive action of the shell material in the process (Fig. 3.13c and d). At this time, the shell material begins to crystallize and the antifluorite lattice of Na_2S become

visible in the shell (the image and associated Fourier-filtered image can be seen in Fig. 3.13e and f). The difference in mass contrast between the darker Cu (higher atomic number) and lighter Na_2S (lower average atomic number) is also evident. Thus, the final phase distribution features a continuous Na_2S phase with Cu particles distributed within and on the surface of the Na_2S, as shown by the schematic in Fig. 3.13g. It is hypothesized that the Na_2S shell that forms hinder the diffusion of the Cu species to the exterior surface of the particles during sodiation. This is likely the reason why Cu metal grows within the interior of many of the particles near the end of the sodiation reaction process. If the Cu species could easily diffuse through the shell, it would be more energetically favorable for the Cu metal to grow on into the external free volume available at the surface rather than growing internally. This Na_2S shell growth was seen over multiple experiments and the final reacted morphology remained consisted whether the material was exposed to the electron beam during reaction. This indicates that the development of this morphology is not changed due to exposure from the electron beam. This type of similar surface layer formation was also reported in a study conducted on the sodiation of NiO performed by He et. al.,[107] although the layer formed was an oxide, rather than sulfide species. In this study, they also postulated that this layer blocked the transport of the Na ions.

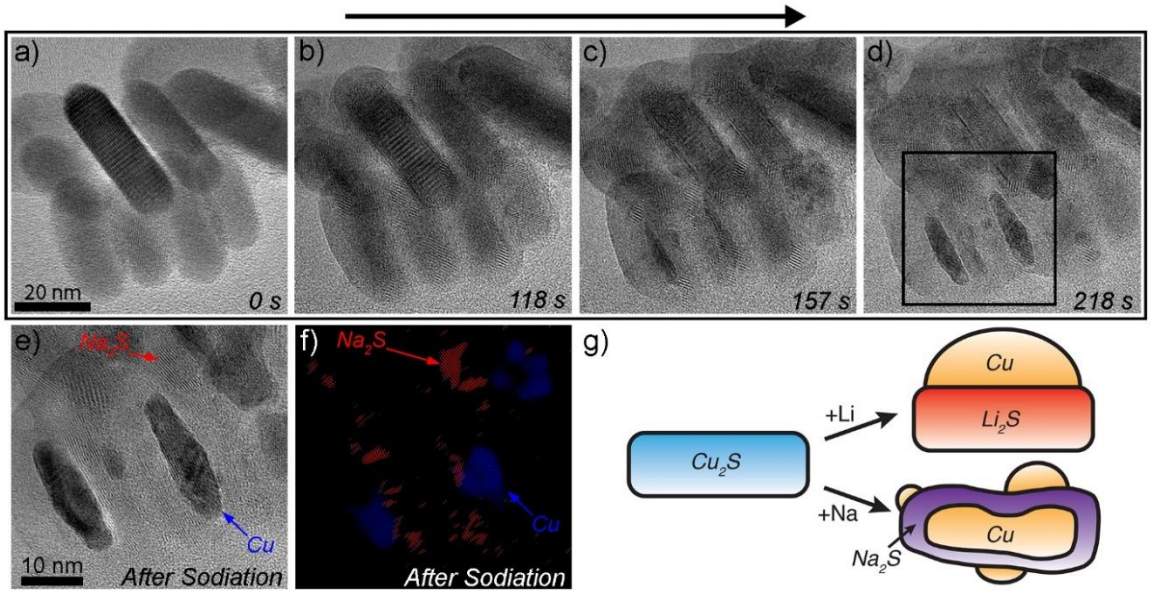

Figure 3.13: (a–d) Higher-magnification in situ TEM imaging during the sodiation of a small group of Cu_2S nanocrystals. **(a)** Before sodiation. **(b)** Initial sodiation has occurred, causing the formation of an amorphous surface layer surrounding the Cu_2S crystals. **(c)** Further sodiation results in the growth of the surface layer, as well as the nucleation and growth of Cu metal particles inside the surface layer and on the surface. **(d)** After complete sodiation, darker Cu metal regions have further expanded in the interior of the surface layer, and the surface layer has crystallized to form Na_2S. **(e)** Magnified view of the boxed region in panel (d), showing the darker Cu metal surrounded by lighter Na_2S. **(f)** Colorized Fourier-filtered image of panel (e), where {111} Na_2S planes are shown in red, and overlapping {111} and {200} Cu planes are shown in blue. The colored planes only appear in certain sections of the phase regions because these sections happen to be aligned correctly for lattice imaging. **(g)** Schematic of the lithiation and sodiation process of Cu_2S causing different structural/morphological evolution.

In the first sodiation process seen in Figure 3.11 it is evident that many of the Cu particles nucleate and grow on the surface of the Cu_2S particles which is in contrast to the results seen in Figure 3.13 where much of the Cu grows inside the Na_2S shell. This is likely the result of the much faster sodiation process seen in Figure 3.11 compared to Figure 3.13.

In the reaction observed in Figure 3.11 a group of particles ~800 nm in size is completely sodiated in ~120 seconds, while the reaction in Figure 3.13 a group of particles ~100 nm in size reacted in approximately the same amount of time. Because of the fast-moving sodiation front in Figure 3.11 and the relatively sharp Na concentration gradient associated with it, individual Cu_2S particles are likely exposed to non-uniform Na concentrations across their width. This is expected to result in sodiation of one side of a particle before a uniform Na_2S shell can grow across the entire particle, which would allow for Cu^+ species to escape to the surface and be reduced to Cu metal. This even causes Cu^+ ions to diffuse between Cu_2S particles across longer distances, as evidenced by the growth of the larger Cu particle beyond the reaction front in Fig. 3.11c. The growth of this larger particle is similar to the growth of the large one-dimensional Cu structures in the lithiated electrode seen in Figure 3.12. However, since active materials in real battery electrodes are surrounded by Na^+-containing liquid electrolyte, it is expected that the sodiation process in such electrodes will proceed in a manner more akin to that shown in Figure 3.13 (where a conformal Na_2S shell grows). This is supported by the *ex situ* SEM imaging of sodiated electrodes, which did not show the growth of large Cu crystals, as was observed in the lithiated electrodes as seen in seen in Figure 3.9 and 3.10.

This data allows for detailed comparison of the sodium and lithium reaction processes. As shown in a recent study[19] and previously discussed, the displacement mechanism during lithiation of Cu_2S is enabled by the similar crystal structures and molar volumes of the Cu_2S and Li_2S phases. The displacement mechanism allows for Cu_2S crystals to be transformed directly into Li_2S crystals by replacing the cations around a nearly invariant sulfur sublattice; this results in Li_2S crystals with nearly exactly the same

size and morphology as the initial Cu_2S crystals (Fig. 3.13g). While Na_2S has the same cubic crystal structure as Li_2S (antifluorite, space group $Fm\bar{3}m$), the molar volume of Na_2S is 1.5 times larger than that of Li_2S. Therefore, the larger volume expansion required during the Cu_2S/Na_2S transformation prevents a displacement mechanism from being active. Rather the Cu_2S crystal structure is destroyed during the growth of the Na_2S phase on the surface as can be seen in the snapshots of Figure 3.13a – e and the schematic in Fig. 3.13g. Thus the sodiation reaction can be better described by the more general conversion reaction mechanism, but there are still significant differences when comparing the final morphology of the sodiated Cu_2S to conventional conversion materials.[105] As mentioned previously, conventional conversion materials (FeS_2, Co_3S_4, NiO, etc.) undergo phase separation on the nanometer scale to form mixed metal/sulfide (or oxide) phases with metal particle size < ~5 nm.[19,88,107] However the sodiation of Cu_2S causes much larger Cu particles to grow both on the surface and in the interior of the original nanocrystals. This is likely caused by the much faster diffusion of Cu^+ in the Cu_2S structure compared to the metal ion species diffusion rate in other conversion-type reaction materials. Furthermore, the high mobility of Cu^+ compared to other transition metals may play a key role in ensuring good reversibility during cycling with Na.

As a last note it is critical to compare the initial electrochemical discharge curves to the newly revealed morphological changes observed in the *in situ* TEM experiments to get a whole picture of the reaction taking place within these battery systems. In the first discharge curve of the lithium cells, a constant potential plateau that corresponds to the continuous growth of Cu metal and transformation of Cu_2S to Li_2S is observed. However, the first Na discharge curve is sloping and shows two distinct regions with a steeper slope

in between. It is speculated that the region at lower potential may coincide with the growth of Cu metal within the particles. This is likely due to the higher associated overpotential caused by the expansion against mechanical constraint when compared to the near-surface growth seen in during lithiation. However, this conclusion requires further investigation of the influence of mechanical stress on the sodiation process. In addition, the changes in the galvanostatic curves of the Na cells over the first few cycles are likely due to changes in morphology and/or structure of the active material during cycling, which is implied by the destruction of the Cu_2S lattice during the first discharge (Fig. 3.13). This contrasts with the reaction of Cu_2S with Li, where the active material maintains a similar structure and morphology during discharge and shows similar potential plateaus during cycling (Fig. 3.5–6). The higher potential of the Li discharge process makes it a candidate as a positive electrode in Li cells (the related material CuS has previously been utilized for primary Li cells),[108] while the lower potential for the Na discharge would make it ineffective as a positive electrode. In Na cells, Cu_2S may be useful as an anode, but further work must be pursued to decrease the voltage hysteresis between charge and discharge.

3.5 Conclusions

In this chapter, the study on Cu_2S revealed the nanoscale-to-macroscale transformation mechanisms during reaction of Cu_2S nanocrystals with Na using in situ TEM and *in situ* XRD combined with *ex situ* and electrochemical methods. During slow sodiation, Cu_2S was observed to form a continuous Na_2S phase with Cu metal particles contained within the Na_2S as well as on the surface. This is fundamentally different than

the lithiation reaction of the same material, which features the growth of large one-dimensional Cu metal structures. Despite the significant structural and morphological changes during sodiation/desodiation, it was found that Cu_2S exhibits excellent cycle life in Na batteries when cycled in a glyme-based electrolyte. Thus, the larger atomic radius of Na compared to Li, and therefore the more substantial volume changes during reaction, does not necessarily cause accelerated capacity decay, but causes the reaction to proceed via a different pathway. The results from these experiments emphasize the importance of understanding the detailed reaction mechanisms and morphological evolution that conversion-type materials undergo for Na batteries, which is critical for engineering next-generation Na-ion batteries with long cycle life.

CHAPTER 4. FRACTURE BEHAVIOR IN CONVERSION MATERIAL WITH LARGER ALKALI-METAL IONS

4.1 Introduction

The previous chapter focused on understanding the effect that sodium alkali-metal ions have on the reaction pathways of a conversion-type material. However, this Cu_2S material undergoes a unique displacement-type reaction with lithium that is not typical for conversion-type sulfide material. To explore the effect of cation size on a typical conversion material that is of interest, the reaction of FeS_2 with lithium, sodium, and potassium was explored. FeS_2 has previously been shown to be a promising high-capacity electrode material for primary Li batteries,[67] and it also has a relatively long cycle life in other Li^+- and Na^+-based systems.[63,64,67–69,73] While this material is known to undergo a conversion-type reaction during lithiation,[19,64,66] the reaction pathways involved with the sodiation and potassiation remain unknown.

Here in this study that was published in Joule in 2018, the dynamic nanoscale reaction mechanisms of FeS_2 with three alkali-ion species (Li^+, Na^+, and K^+) was investigated using a combination of *in situ* TEM and electrochemistry, similar to the study conducted on Cu_2S, however modeling, and mechanical testing was conducted with the help of collaborators here at Georgia Tech. This work shows that the conversion reaction is active for all three alkali metal ions and that the phase transformation during discharge proceeds by a similar two-phase mechanism in each case. However, the mechanical integrity of individual FeS_2 nanocrystals was found to sharply diverge when reacting with different alkali metals. Interestingly, although lithiation causes smaller volume expansion

than the reaction with Na^+ or K^+, fracture only occurred during reaction with Li^+. Modeling of the reaction-induced deformation showed that this unexpected behavior is due to fundamental differences in the evolution of the reaction front shape during reaction with the alkali ions and could also be influenced by different mechanical properties of the reacted phases. These results indicate that despite larger volume changes, unforeseen nanoscale reaction pathways may mitigate mechanical degradation and allow for the effective use of conversion and alloying materials for rechargeable Na- and K-based batteries.[31]

4.2 Electrochemical Behavior of FeS_2

The discharge behavior of FeS_2-based active electrodes in electrochemical half cells was examined for comparison to the later *in situ* TEM results. These cells were fabricated with alkali metal counter electrodes and commercial FeS_2 powder in the working electrodes, along with organic electrolytes containing different alkali metal salts. This was done using the experimental procedure described previously. In this study the electrolytes used for the tests are as follows: 1.0 M $LiPF_6$ in 1:1 v/v ethylene carbonate/diethyl carbonate, 1.0 M $NaPF_6$ in diethylene glycol dimethyl ether, and 1.0 M KPF_6 in a 1:1 v/v mixture of ethylene carbonate/diethyl carbonate. For these experiments the lower voltage limits were 0.6 V vs. Li/Li^+ for Li/FeS_2 cells, 0.5 V vs. Na/Na^+ for Na/FeS_2 cells, and 0.5 V vs. K/K^+ for K/FeS_2 cells. Figure 4.1 shows the galvanostatic discharge curves from Li, Na, and K half cells. The electrochemical conversion reaction of FeS_2 with alkali metal ions is expected to behave according to the following equation:

$$FeS_2 + 4M^+ + 4e^- \rightarrow Fe + 2M_2S \qquad \text{(Eq. 4.1)}$$

where M is the alkali metal of interest. The full conversion to M_2S would involve electrochemical reduction of both the Fe^{2+} cation and the S_2^{2-} species.

All three discharge curves show relatively flat initial plateaus at different potential values, followed by sloping sections. The Li discharge behavior is consistent with prior studies, some of which have also reported an additional higher-potential plateau at slow discharge rates.[67] The discharge of the Li cell shows the longest plateau, while the Na and K cells exhibit shorter plateaus. These flat potential plateaus in all three cases indicate two-phase reactions, which correspond to the two-phase reactions and sharp reaction fronts. The standard potentials of Li/Li^+, Na/Na^+, and K/K^+ are -3.04 V, -2.71 V, and -2.93 V vs. SHE, respectively. Since the initial plateaus in the galvanostatic curves are at different potentials in Fig. 4.1, this suggests that the energetics of the two-phase reaction are similar for all three cases, with the varying standard potentials of the alkali metal redox couples influencing the positions of the plateaus. The two-phase mechanism is active for all three cases. Finally, the theoretical specific capacity for the reaction of FeS_2 to form Fe and the associated alkali metal sulfide is 894 mAh g^{-1} in all three cases. Figure 4.1 shows that the Li cell comes the closest to this theoretical capacity, and as the size of the alkali metal ion increases, the specific capacity decreases. This may be due to kinetics limitations due to the larger ionic size of Na^+ and K^+.

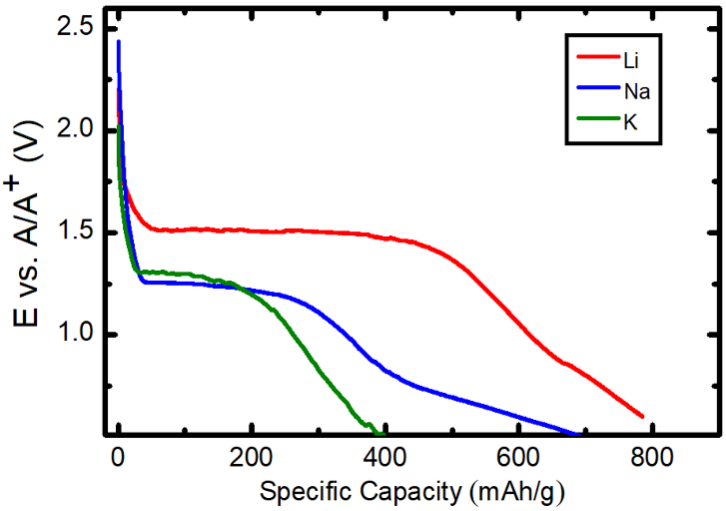

Figure 4.1: Galvanostatic discharge curves for FeS_2 electrodes in Li, Na, and K half cells at a rate of C/20 (full discharge in 20 h). The discharge curves are plotted on the same graph with different potential (*E*) scales, where A/A^+ corresponds to Li/Li^+, Na/Na^+, and K/K^+.

4.3 Phase Evolution of FeS_2

The overall phase evolution of the FeS_2 active material in these electrochemical cells was examined next using *ex situ* XRD. Figure 4.2 shows *ex situ* x-ray diffraction (XRD) data from a pristine electrode and electrodes after discharge in Li, Na, and K cells. The pristine commercial FeS_2 material (black trace) displayed Bragg peaks corresponding to cubic pyrite, as well as a minor FeS phase component. After lithiation (Fig. 4.2, red), all the sharp FeS_2 peaks disappeared and broad, weak peaks associated with Li_2S (ICDD 04-008-3440) emerged, indicating that poorly crystalline Li_2S was present after the reaction. Fe peaks were not visible due to the small size of these crystals. The XRD trace from the Na cell after discharge (Fig. 4.2, blue) also showed the disappearance of the FeS_2 peaks,

but there were no observed crystalline reaction products. After discharge in a K cell (Fig. 4.2, green), the FeS_2 Bragg peaks did not completely disappear, but only decreased in intensity while no other peaks appeared. This indicates that the active material did not fully react in the K cell, which is supported by the lower specific capacity of this cell compared to the other two. However, the decreased intensity of the peaks still shows that the electrochemical reaction of FeS_2 occurred in the K cell, which has not been reported before. The FeS_2 active material is likely undergoing a conversion reaction under electrochemical conditions.

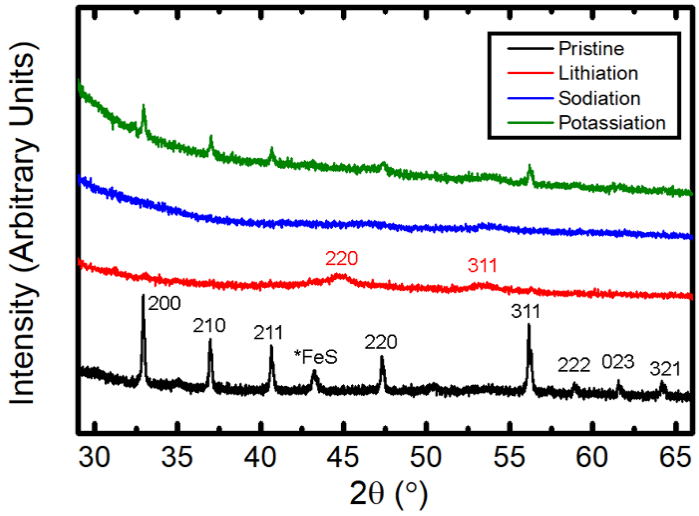

Figure 4.2: *Ex situ* XRD of FeS_2 electrodes before and after discharge in Li, Na, and K half cells.

4.4 *In Situ* TEM of FeS_2 Nanoscale Reaction Mechanisms

FeS_2 nanocrystals used for *in situ* TEM investigations were synthesized using the synthesis method described in Chapter 2.3. This synthesis produces cube-shaped nanocrystals with relatively uniform size. These nanocrystals were used as the active

material for the *in situ* TEM experiments utilizing the experimental setup seen in Figure 4.3a, and previously discussed in Chapter 2. An unreacted FeS_2 nanocrystal is shown in Fig. 4.3b, and the associated fast Fourier transform (FFT) is displayed in Fig. 4.3c. The FFT shows that the material is cubic pyrite (ICDD 04-004-6511, space group $Pa\bar{3}$), and the crystal is viewed along the [100] zone axis. Thus, the faces of these cube-shaped nanocrystals are the {100} crystallographic planes. A selected area electron diffraction (SAED) pattern from a collection of pristine FeS_2 nanocrystals is shown in Fig. 4.4e. Lithium conversion reaction processes are known to produce biphasic structures with finely interspersed metal and sulfide or oxide phases after reaction.[19,25,88,89] While Li^+ and Na^+ are known to react with FeS_2 via a conversion mechanism,[19,68] the mechanism during reaction with K^+ has not been reported.

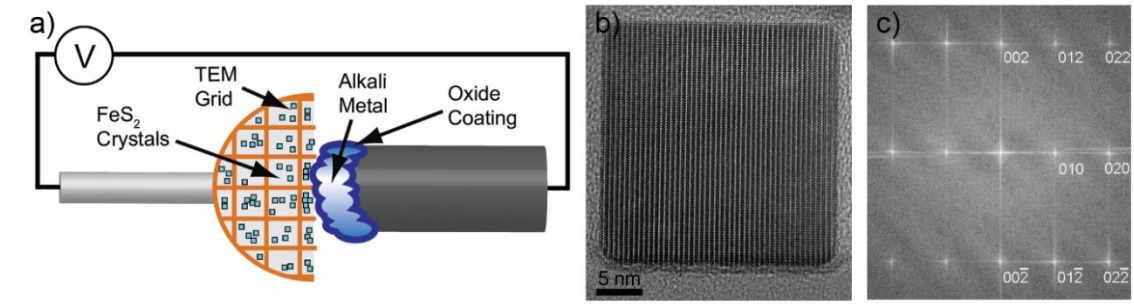

Figure 4.3: (a) Schematic of the *in situ* TEM experimental setup. **(b)** High resolution TEM image of an individual unreacted cubic FeS_2 crystal. **(c)** The fast Fourier transform (FFT) of the unreacted FeS_2 crystal in (b) showing that the material is cubic pyrite viewed along the [100] zone axis.

4.4.1 *In Situ* TEM of FeS_2 Lithiation

First the nanoscale lithiation reaction of FeS_2 was examined. Figure 4.4a-d shows two cubic FeS_2 nanocrystals reacting with Li^+. The key feature of this reaction the existence of a sharp reaction front between the internal FeS_2 crystal (the darker region) and the outer reacted mixture phase with the expanded volume (the lighter region). This reaction progress can be tracked as the sharp front moves inward until the end of the reaction. The shape of the shrinking internal FeS_2 crystal during the reaction process remains approximately cubic regardless of size, as seen in Figure 4.4a-d where two different sized particles can be seen. At a certain point as the internal particle is consumed, a crack is seen to nucleate in the bottom right corner of the larger particle and top left of the smaller (Fig. 4.4c). At this point the reaction proceeds very quickly as the crack grows, exposing more of the internal FeS_2 crystal. Additionally, the particle begins to fracture at multiple places and by the end of the reaction, only a cluster of several fragments of the reacted phase remain (Fig. 4.4d). It is also worth noting that in the image of the fully reacted particle in Figure 4.4d, the middle of the larger particle only exhibits darker contrast due to it being thicker than the other regions.

The lithiated phase that formed during the reaction process is a biphasic structure consisting of Li_2S and Fe phases intermixed at the nanoscale. This structure is evident in the speckled contrast of the reacted region in Figure 4.4a-d; the darker specks correspond to nanoscale Fe particles, in agreement with prior work.[19] Before the reaction, sharp FeS_2 diffraction spots were produced by the pristine material (Fig. 4.4e). The SAED pattern of lithiated FeS_2 in Fig. 4.4f shows broad rings that arise due to diffraction from Li_2S, but no diffraction spots from body-centered-cubic Fe were detected. A recent study by Butala et.

al. used X-ray diffraction and pair distribution function analysis to conclude that the small Fe clusters produced through this electrochemical conversion reaction are in fact disordered,[109] which aligns with our observations. The detection of Li_2S was confirmed by the XRD performed earlier which detected poorly crystalline Li_2S after full reaction. The theoretical volume expansion for the full conversion reaction is 2.6 (*i.e.*, the volume of the final Li_2S and Fe phases together is 2.6 times that of FeS_2). It was difficult to estimate the volume expansion of most of the particles because of morphology changes due to fracture, but measurement of nine particles that did not fracture yielded an observed volume expansion of 1.8±0.4 after lithiation. The discrepancy between observed and theoretical volume expansion potentially arises due to incomplete reaction of the sulfur species. Finally, a plot that shows the occurrence of fracture as a function of particle size is shown in Fig. 4.4g. Fracture was observed during lithiation for all sizes tested (between 20 nm and 100 nm), but some particles with initial size <50 nm did not fracture. In an effort to provide statistical relevance to these results, many experiments were performed and another such experiment showing similar fracturing behavior in smaller particles can be seen in Figure 4.5.

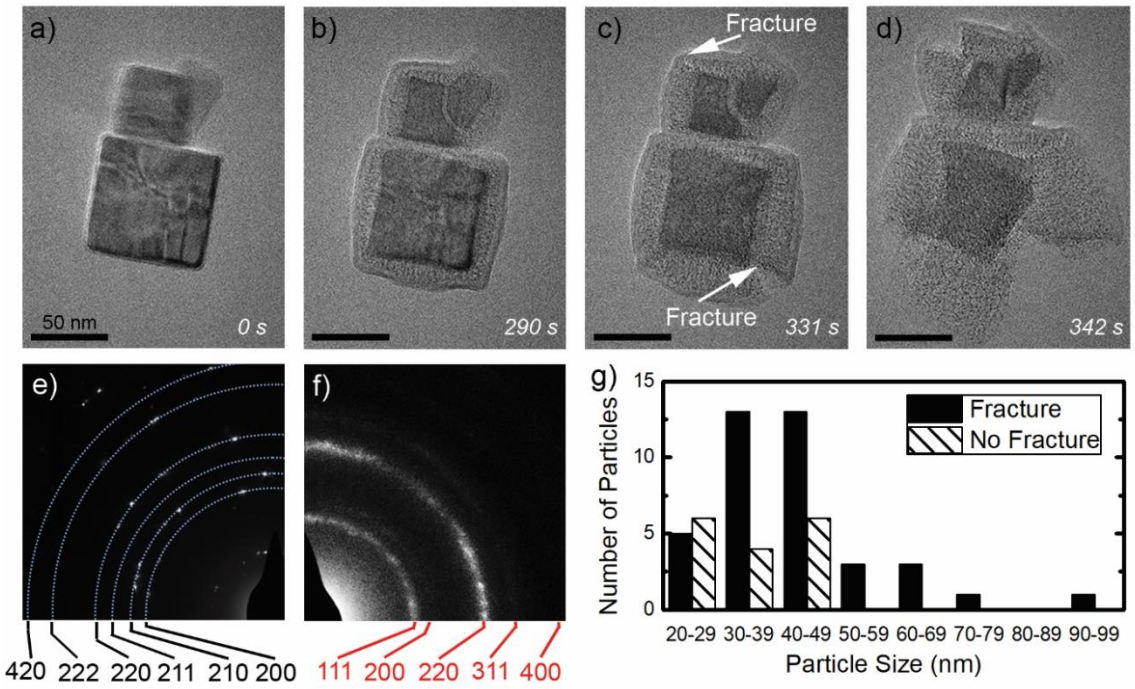

Figure 4.4: (a-d) Snapshots of the lithiation of two FeS_2 nanoparticles. **(a)** The particles prior to reaction with lithium. **(b)** Lithiation has begun, and a sharp reaction front is visible between the internal FeS_2 crystal and the reacted mixture of Li_2S and Fe. **(c)** Cracks have formed at the bottom right corner of the larger crystal and the top left corner of the smaller crystal. **(d)** The frame after full lithiation of the larger particle (the small particle still has FeS_2 within the interior); additional cracks have initiated and grown. **(e)** The selected area electron diffraction (SAED) pattern of a group of pristine FeS_2 particles. **(f)** The SAED pattern of the lithiated FeS_2 crystals showing broad rings corresponding to Li_2S. **(g)** A plot displaying the occurrence of fracture after lithiation as a function of the initial particle size.

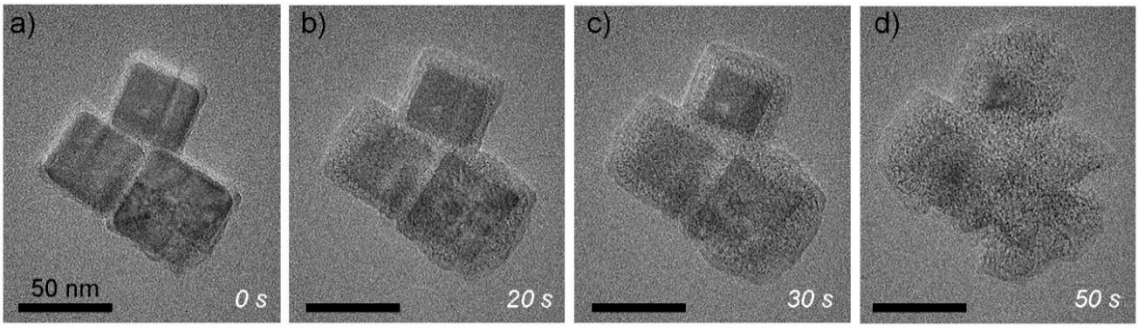

Figure 4.5: (a-d) Snapshot images from an *in situ* TEM experiment of the reaction of a group of particles with lithium.

High-resolution imaging of the reacted material revealed Li_2S lattice fringes, and the Fe particles were embedded within this Li_2S matrix (Fig. 4.6). In Figure 4.6a a sample high-resolution image can be seen after full lithiation. Using the image processing software, ImageJ, a fast Fourier transform (FFT) was performed on this image, the crystalline Li_2S {111} planes were then isolated. From this an inverse FFT was performed, resulting in the Fourier-filtered crystallinity map seen in Fig. 4.6b. The size and distribution of these Fe particles were then analyzed. To determine the average size of the Fe particles after reaction, the contrast threshold was changed to only highlight the Fe particles due to their darker contrast, and then the image was binarized. Using the command "Analyze Particles" in the software, the area of any continuous group of black pixels was automatically recorded, allowing for calculation of the average particle size and standard deviation. Figure 4.6c shows a map of the analyzed Fe particles associated with the image of the lithiated FeS_2 in Fig. 4.6a. The spatial distribution of Fe particles was found by calculating the FFTs of material that had been fully reacted, as well as FFTs of the lithiated carbon grid. The FFT of the reacted carbon grid was then subtracted from the FFT of the

reacted particles. This resulting image then contained the characteristic rings and spots associated with the planar spacing of the sulfide reaction products, as well as a tight diffuse ring that corresponded to the average spacing of the Fe particles in the reacted product mixture. From these images, the average size of the Fe particles in the matrix was found to be 1.0±0.25 nm, and the separation between Fe particles was ~2.5 nm. Particles of these size are consistent with previous studies on conversion-type material reaction products including the previous work that confirmed the disordered nature of the Fe particles.[109]

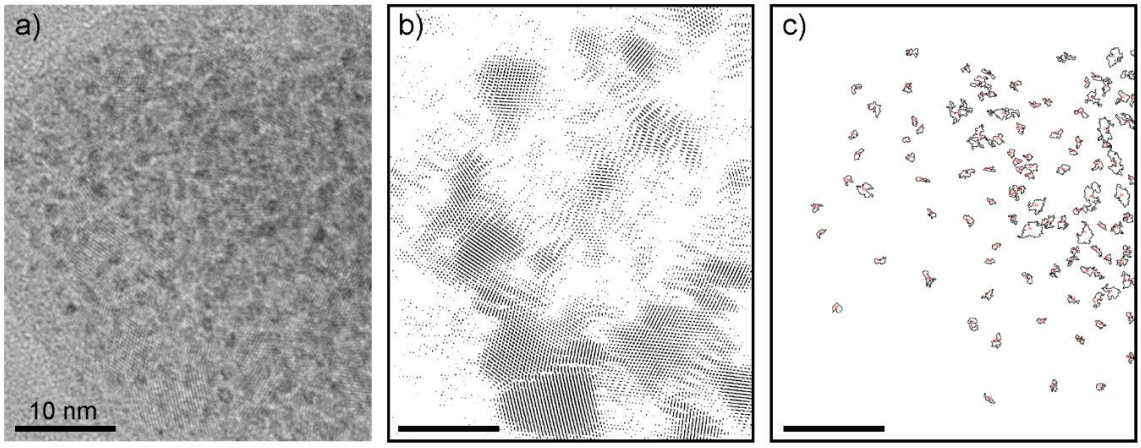

Figure 4.6: (a) High-resolution TEM (HRTEM) image of FeS_2 after reaction with Li. **(b)** Inverse FFT showing the lattice fringes that correspond to {111} Li_2S planes in (a). **(c)** Map of Fe particles in (a).

4.4.2 *In Situ* TEM of FeS_2 Sodiation

In situ TEM results from the sodiation of FeS_2 nanocrystals are shown in Figure 4.7. In Figure 4.7a, crystals in the bottom right of the frame had already begun to react, since the Na ions were diffusing along the carbon support from this direction from a source that was ~1 micron away. Similar to the previous section on the lithiation of this material

sharp reaction fronts are visible between the interior FeS_2 regions and the reacted regions in Figure 4.7b and c during sodiation. The FeS_2 crystals in the interior of the particles did not retain cubic shapes during the reaction. Instead, the initially cubic FeS_2 crystals transformed to spherical or ellipsoidal shapes, as shown in the magnified inset of Figure 4.7c. This is in contrast to the lithiation case seen in the previous section in which crystals retained cubic shapes during the reaction. After the reaction was complete, the sodiated particles were observed to merge together (Fig. 4.7d). However, unlike the lithiation case, fracture did not occur despite a larger measured average volume expansion of 2.7±0.3. The theoretical volume expansion for the formation of Na_2S and Fe is 3.8, which again suggests that some of the material undergoes incomplete reaction. After reaction (Fig. 4.7d), contrast due to the two-phase mixture of Na_2S and Fe particles was evident. The SAED pattern after sodiation in Fig. 4.7e features weak rings corresponding to Na_2S, indicating that the Na_2S was present but had poor crystallinity. This poor crystallinity was likely not detected by the *ex situ* XRD performed due to the small crystallite size of the reacted Na_2S. The resulting Fe particles were found to be approximately 0.58±0.15 nm in size, which is smaller than the lithiation case. The average Fe-Fe particle separation within the matrix was also smaller, at ~1.8 nm. Once again additional experiments were performed and another example of this sodiation reaction can be seen in Figure 4.8.

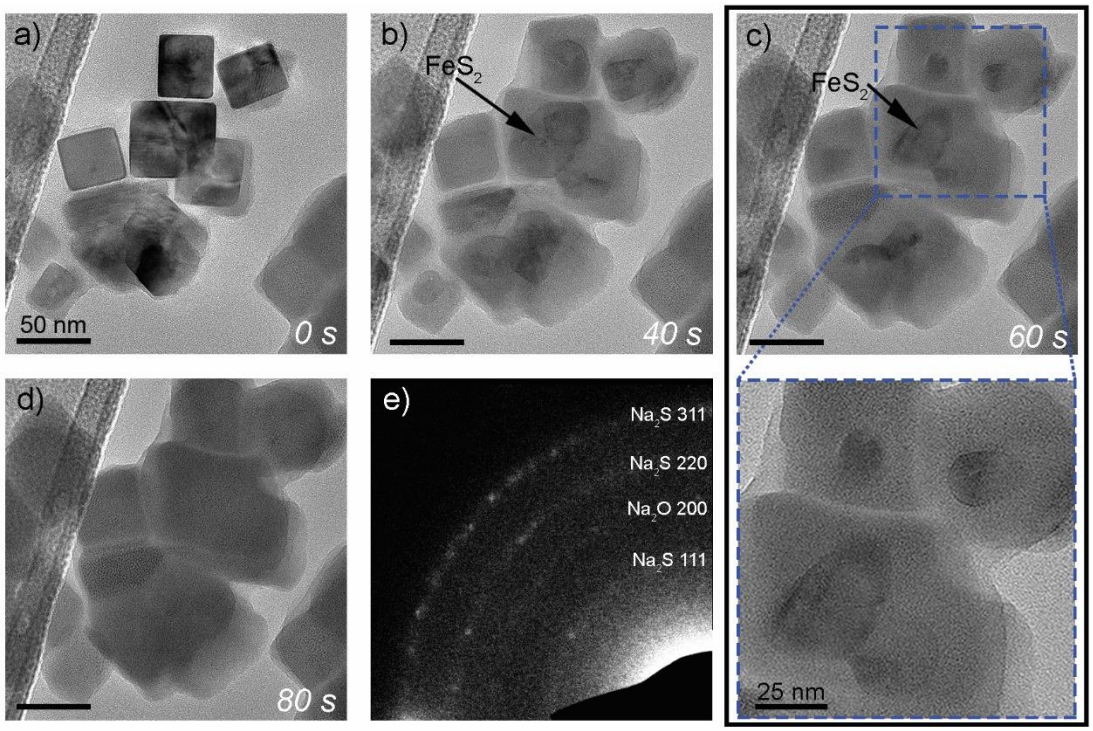

Figure 4.7: Snapshots of the sodiation of a group of FeS_2 particles. **(a)** Four unreacted FeS_2 particles are in the upper half of the frame, and the sodiation front is approaching from the lower-right corner of the frame. **(b)** The particles are shown in the midst of sodiation, and a sharp reaction front is visible between the unreacted crystals and the reacted phase. **(c)** Continuation of the sodiation reaction. The internal FeS_2 crystals within the particles have lost their initial shapes, and they have formed spherical or oblong shapes, as seen in the magnified inset. **(d)** All particles have reacted and the sodiated particles have merged together. **(e)** SAED pattern of the sodiated material showing diffuse rings that indicate the presence of Na_2S and Na_2O, which likely arises due to reaction of oxygen-containing groups on the surface of the carbon support.

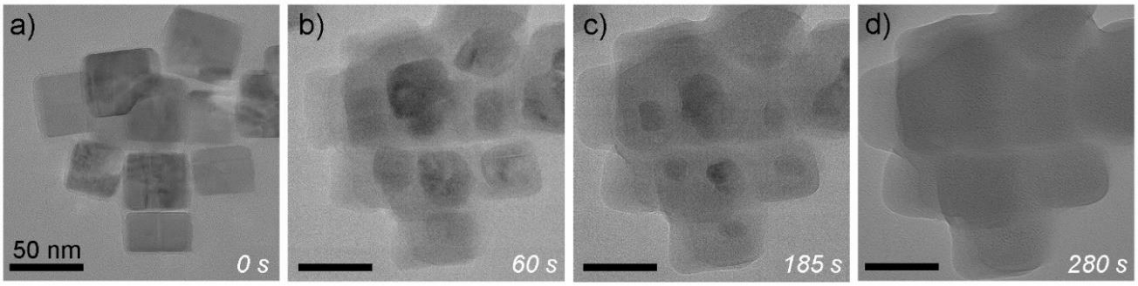

Figure 4.8: (a-d) Snapshot images from an *in situ* TEM experiment of the reaction of a group of particles with sodium.

4.4.3 *In Situ* TEM of FeS_2 Potassiation

The reaction of FeS_2 with K^+ was also examined with *in situ* TEM, and data from a typical experiment are shown in Figure 4.9. Figure 4.9a shows two overlapping FeS_2 crystals on the edge of the carbon support; the K probe is visible at the top of the frame. It was found that potassiation required direct contact to be made between the oxide/hydroxide layer on the surface of the K probe and the FeS_2 crystal, as shown in Figure 4.9b. This contact requirement was likely due to the slow diffusion of K^+ ions through the carbon support film, which is in contrast to the Li^+ and Na^+ cases. During contact and biasing in Figure 4.9a-b, the reaction initially progressed rapidly before slowing in Figure 4.9c-d. A sharp reaction front formed between the FeS_2 crystals and the reacted phase, which is similar to the lithiation and sodiation process. During potassiation, the "rounding-off" of the corners of the FeS_2 crystal was also evident, as shown in Figure 4.9c. After full reaction (Fig. 4.9d), fracture did not occur despite the large average volume expansion of 3.1±0.6, as measured across many experiments. As in the lithiation and sodiation cases, this observed volume expansion is lower than the theoretically-predicted value of 5.4. The

SAED pattern of the final reacted phase in Figure 4.9e shows a diffuse ring that corresponds to an amorphous product, which is consistent with the XRD performed. No image contrast from separate Fe and potassium sulfide phases was evident, indicating a single-phase amorphous product that contains K, Fe, and S. Once more additional experiments required direct contact and led to an expanded amorphous reacted product as seen in Figure 4.10.

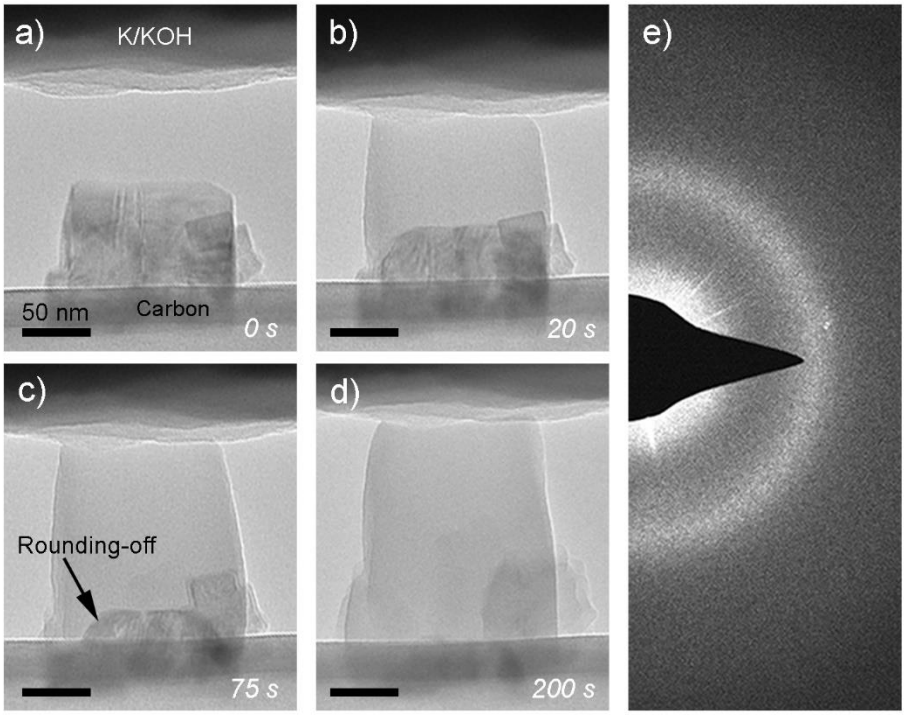

Figure 4.9: (a-d) Snapshots of the potassiation of FeS_2. **(a)** A pristine FeS_2 particle with a smaller overlapping particle on the right side. **(b)** Potassiation has begun after contact and biasing, and a sharp reaction front between the lighter reacted phase and the FeS_2 crystal is evident. **(c)** An image after further reaction; the edges of the FeS_2 crystal are blunted. **(d)** Image after full reaction of the FeS_2. **(e)** The SAED pattern of the final reacted amorphous product.

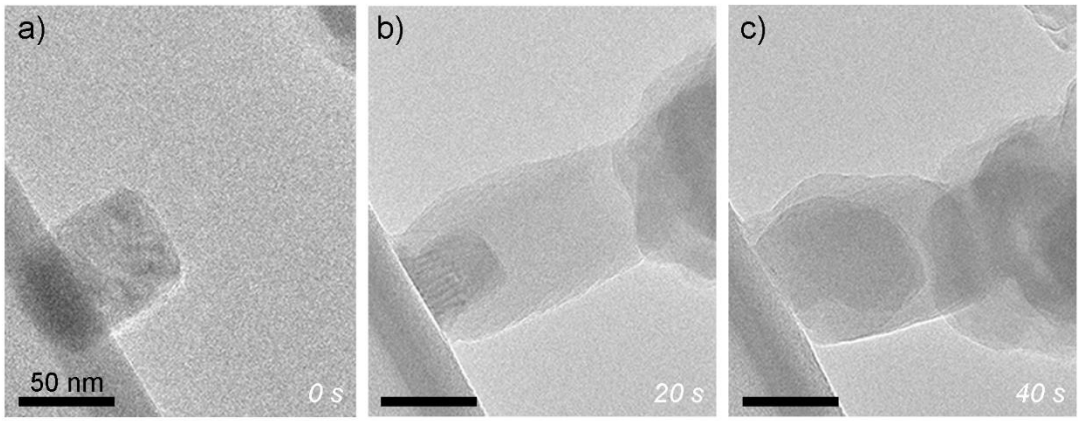

Figure 4.10: (a-c) Snapshot images from an *in situ* TEM experiment of the reaction of a particle with potassium. In the images, the FeS_2 particle is on the left, and the potassium electrode is on the right.

4.4.4 Comparison of the *In Situ* TEM of FeS_2

This investigation of the reaction process with all three alkali ions under similar conditions allows for valuable comparisons to be made regarding reaction mechanisms. For each case a sharp reaction front is observed which is consistent with the electrochemistry performed. Multiple aspects of these reactions behave according to rational trends when moving from Li^+ to K^+. For instance, it was found that the average size of the Fe particles in the product phase decreased as the alkali ion size increased. In tandem with this observation, the crystallite size of the alkali sulfide product also decreased with increasing alkali ion size. In all cases, the particle size in the product phase did not change after initial reaction, and it did not depend on FeS_2 crystal size. The formation of the product phase at the reaction front likely involves the short-range migration of Fe atoms to form clusters as the alkali sulfide is formed around it. The decrease in Fe particle size

when reacting with larger ions therefore indicates that the size and/or mobility of the alkali ion influences the extent to which Fe is able to migrate within the reacted phase to form clusters, with the smallest ion (Li^+) enabling the easiest migration. In addition to this trend, the magnitude of volume expansion increased with alkali ion size, as expected. Finally, it was observed that all three alkali ion species reacted with FeS_2 via a two-phase reaction with an associated sharp reaction front; this indicates that the reaction kinetics is controlled by short-range interactions and bond-breaking near the reaction front. Two-phase reactions also occur in other large-volume-change battery materials such as Si and Ge.[15,23,87,110]

4.5 Linking Fracture to Phase Transformation Processes

While the trends mentioned in the previous section can be easily explained by the increase in the size and mobility of the alkali ions, the morphology changes and fracture processes observed in these experiments are difficult to rationalize using these criteria alone. In the dozens of particles studied for each alkali species, fracture during reaction only occurred during lithiation. Fracture did not occur during either sodiation or potassiation despite the larger volumetric expansion associated with these reactions and regardless of particle size (the largest particles that were tested were ~120 nm). This is counter-intuitive, as larger volume expansion is generally associated with greater stress values that could more effectively drive crack formation. Since fracture has been linked to electrochemical degradation processes in batteries,[111–113] these observations have implications for the beneficial use of FeS_2 in Na- and K-based systems. However, the question remains regarding the cause of this divergent fracture behavior. Several factors

were explored in depth in the following sections, including the effect of the mechanical properties of the reacted phase and the effect of the shape evolution that took place during reaction.

4.5.1 Mechanical Properties of the Reacted Phase

In an attempt to make sense of this fracture behavior the mechanical properties of the lithiated, sodiated, and potassiated materials were measured. If the sodiated and potassiated materials properties are drastically different from the lithiated this could influence fracture characteristics. While the mechanical properties (*e.g.*, yield strength, elastic modulus) of a number of different lithium alloy materials have been measured,[18,111,114–116] the mechanical properties of conversion materials, as well as Na and K electrode materials, have been less-studied.

To gain a basic understanding of the mechanical properties of electrochemically reacted FeS_2, nanoindentation experiments were carried out with the help of our collaborators in Prof. Shuman Xia's group here at Georgia Tech. The result of these experiments can be seen in Figure 4.12. FeS_2 thin films with thicknesses between 200 and 400 nm were grown by sulfurizing sputtered Fe films. Fe films were sputtered onto Ta foil substrates, and sulfurization was carried out in a tube furnace by heating the Fe films to 500 °C while exposing them to sulfur vapor entrained in Ar flow, a sample image of this pristine film can be seen in Figure 4.11. Sulfur powder was placed upstream of the Fe films in the tube furnace, and Ar was flowed at 40 sccm while the pressure was maintained at 1200 mTorr.[117] These films were then directly used as working electrodes in Li, Na, and K

half-cell-type coin cells. Discharge was performed using currents of C/20 with 0.6 V as the cell potential cutoff value (Figure 4.13 shows typical thin-film discharge curves). After discharge, the working electrodes were removed in an Ar-filled glove box with <0.1 ppm H_2O and O_2 content, and the films were indented in the same glove box using a Hysitron nanoindentation system with a Berkovich indenter tip. Residual liquid electrolyte was immediately removed from the film surfaces using Kimwipe tissues after extraction of the samples from the coin cells. All films were tested without washing with extra solvent to avoid delamination of films and to minimize the chance of excessive side reactions. Surface scanning with the indentation tip was utilized to identify relatively smooth regions for accurate indentation measurements. It is worth noting that the grain size effects would likely affect the overall mechanical properties through the Hall-Petch relationship, but multiple indentation tests were used to limit this effect. Additionally, the inverse Hall-Petch relationship tells us there is a critical grain-size past which the hardness decreases with decreasing grain size. Therefore, the general trend from these studies relative to each other are the key finding from these experiments. The pristine and reacted films demonstrated similar topographic morphology, suggesting minimal presence of a solid electrolyte interphase (SEI) layer.

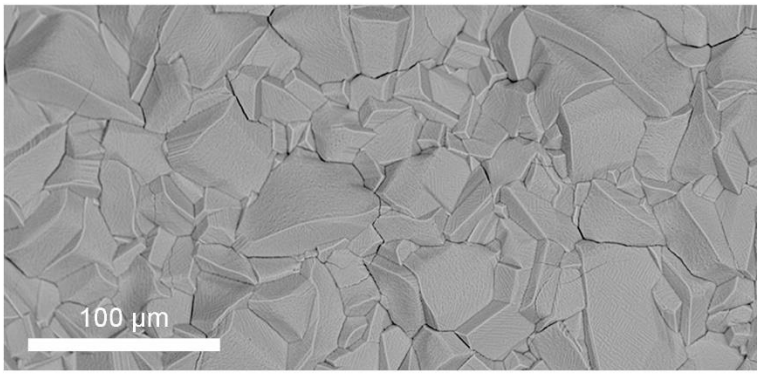

Figure 4.11: SEM image of the FeS_2 film on the Ta foil sulfurized at 500°C prior to electrochemical reactions in half-cells.

A peak load of 40 µN at a constant loading/unloading rate of 8 $\mu N \cdot s^{-1}$ was used during nanoindentation tests. The loading/unloading curves can be seen in Figure 4.12a, where the lithiated, sodiated, and potassiated curves are found to be very similar. Using this plot, the reduced modulus can be found and is plotted in Figure 4.12b. From the peak load, P_{max}, used for these tests and the resulting contact area, A_c, of the indent left the hardness values, H_c, was obtained using the following equation, $H_c = P_{max}/A_c$. The hardness value for these reacted films is compared to a pristine film in Figure 4.12c. For each film, data were collected from at least five indents conducted at different locations on the film to ensure the measurements were not affected by local morphological variations.

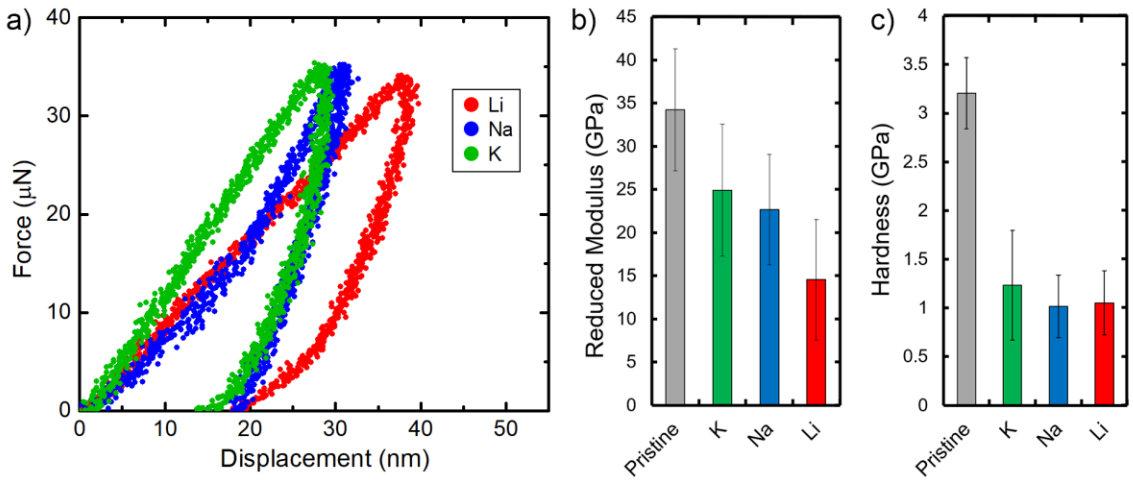

Figure 4.12: Nanoindentation experiments performed on electrochemically reacted FeS_2. **(a)** Representative force vs. displacement indentation curves of lithiated (red), sodiated (blue), and potassiated (green) FeS_2 films; the lithiated film shows the most significant displacement. **(b)** A bar chart showing the elastic modulus of each of the reacted films compared to pristine FeS_2. **(c)** A bar chart showing the hardness of each of the reacted films compared to pristine FeS_2. Each of the reacted films have similar hardness.

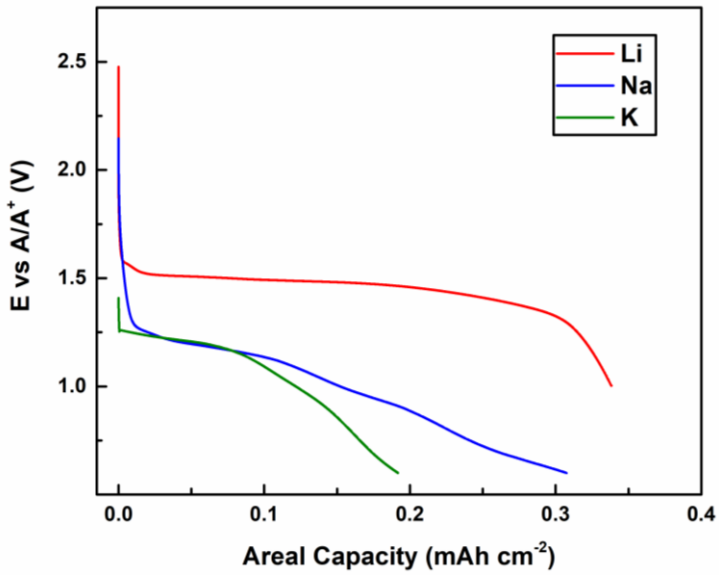

Figure 4.13: Galvanostatic discharge curves for ~400 nm thick FeS_2 thin film electrodes from Li (red), Na (blue), and K (green) half cells. These thin film electrodes were used for

nanoindentation tests. The cells were discharged at a rate of 15 μA/cm^2, with the discharge capacities normalized to the area of each electrode.

As shown in Figure 4.12, the lithiated FeS_2 film exhibited slightly lower elastic modulus but similar hardness compared to the sodiated and potassiated material. Thus, the three materials should flow at similar stress values. Since lithium was the only alkali ion to induce fracture in the nanocrystals during reaction, these findings suggest that the differences in mechanical properties are not the result of the mechanical properties of the reacted phase. It is worth noting that comprehensive mechanical investigation of these materials must be undertaken to fully understand the effects of mechanical properties; for instance, measurement of fracture toughness is necessary.

4.5.2 Shape Evolution Effect on Fracture Behavior

One factor that likely contributes to the observed differences in fracture behavior is the evolution of the shape of the reaction front during reaction. During lithiation, the internal crystalline FeS_2 generally maintained a square or rectangular shape throughout the reaction process; in other words, the {100} planes of the crystal structure were maintained at the reaction front. As previously discussed, the corners of the FeS_2 crystals became blunted during sodiation and potassiation, leading to crystals that were circular or oblong (in projection) during reaction. This indicates that the {100} planes did not preferentially exist at the reaction front. To provide statistical evidence for these observations across many tested particles and to quantify the extent of crystal shape changes, Figure 4.14 is a

plot that captures the shape of the internal FeS_2 crystals during reaction as a function of particle size. Each data point in the plot is from a distinct particle, which illustrates the generality of the observations presented in the previous *in situ* TEM figures. These points are from the subset of particles in which the internal crystal shape during the reaction was able to be measured. The "crystal shape descriptor" is plotted on the *y*-axis; this value is defined as the rectangular area in which the crystal is inscribed, divided by the actual area of the FeS_2 crystal. Based on the inset schematics in Fig. 4.14 for crystals surrounded by reacted material, the crystal shape descriptor *Y* would be calculated as

$$Y = wh/A, \qquad \text{(Eq. 4.2)}$$

where *wh* is the square or rectangular area in which the crystal is inscribed, and *A* is defined as the actual FeS_2 crystal area. Thus, for crystals that retain a rectangular shape during reaction, the shape descriptor would remain close to 1.0. For crystals that transform into spherical or oval shapes, the shape descriptor would be larger. The plot in Fig. 4.14 shows the maximum crystal shape descriptor during the reaction, and each data point corresponds to a different measured crystal.

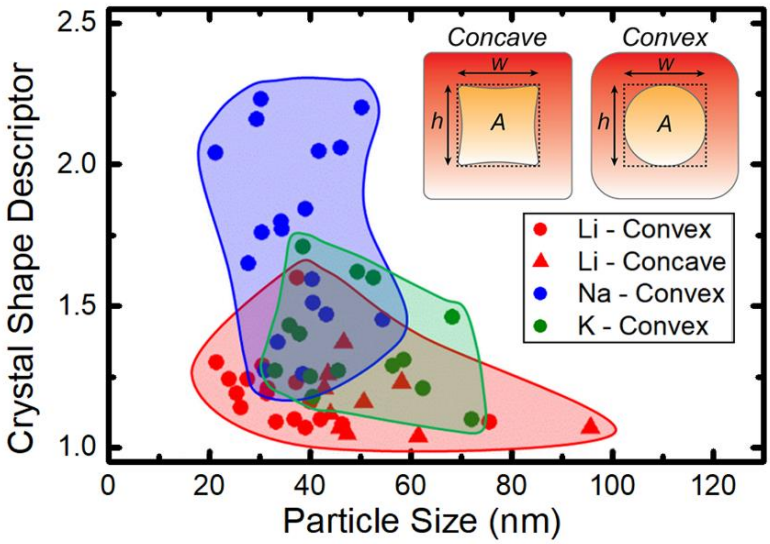

Figure 4.14: Statistical plot that quantifies the change of the FeS_2 crystal shape during reaction with each of the alkali ions. The crystal shape descriptor, *Y*, is defined as $Y=wh/A$, where *wh* is the rectangular area that the crystal is inscribed within and *A* is the actual remaining FeS_2 crystal area. A crystal descriptor greater than 1.0 indicates a more oval or spherical crystal shape.

The data in Figure 4.14 show that, across all experiments, reaction with different alkali species resulted in quantitatively different internal crystal shapes. Lithiation resulted in crystal shape descriptor values that were close to 1.0 (generally less than 1.35) across all sizes, which indicates that the crystals retained shapes that were close to rectangular or square. The crystal shape descriptor values for sodiation were higher than lithiation (ranging between ~1.25 and ~2.25), while the values for potassiation fell between the other two cases (ranging between ~1.10 and ~1.70). Thus, sodiation featured the most extensive transformation to oval and circular crystal shapes. It should be noted that irregular oval shapes led to high crystal shape descriptor values around 2.0. Finally, for the lithiation case, crystals that evolved to take either convex or concave shapes were observed (see the

schematic inset in Fig. 4.14). The concave shape only appeared when particles exceeded about 42 nm in size.

It is clear that the different alkali ions caused different internal crystal shapes to evolve during reaction. These variations can be attributed to differences in the atomic-scale dynamics of bond-breakage at the reaction front between the reacted material and the FeS_2 crystal. The square or rectangular shapes during lithiation are due to preferential reaction of the {100} planes of the FeS_2 crystal, which results in the retention of these facets at the reaction front. This suggests that the kinetics of the reaction in these small particles is interface-limited, as is seen in other large-volume-change materials, such as silicon.[23] The preferential lithiation of the {100} planes likely occurs due to a favorable atomic arrangement at these planes that promotes reaction with Li^+. In contrast, the lack of sharp facets during reaction with Na^+ and K^+ indicates that the {100} planes do not react preferentially, even though the kinetics are likely still interface limited. The "rounding-off" or blunting of corners during sodiation and potassiation could be caused by higher concentrations of alkali ions available for reaction near the corners/edges due to increased ion transport pathways from the particle surface at these locations, which could influence interfacial reaction rates. This suggests that blunting of corners naturally arises in the absence of planes of preferential reaction in such two-phase transformation processes.

Based on this collected data the evolution of crystal shape and the occurrence of fracture are likely related. Fracture was observed only during reaction with lithium, and lithiation was the only case in which the internal crystal shape remained as a square or rectangle. Interestingly, cracks were often observed to initiate at corners of the nanocrystals during lithiation. These observations suggest that the highly anisotropic expansion of the

FeS_2 during lithiation is related to the fracture process. The preferential expansion at cube faces during lithiation causes tensile stress concentrations at the surface between reacting faces (*i.e.*, at the corners), which could cause cracks to preferentially initiate at the corners. Prior work has been performed to describe the stress state within particulate battery materials during two-phase, large-volume-change reactions such as that observed here in FeS_2.[16,18,57,58,118] These studies show that the reacted product phase near the reaction front experiences significant compressive stress, while the surface of the particle experiences tensile stress. While these studies were generally conducted on alloying-type materials, the stress has been found to be generated in these materials if the volume changes occur via an inhomogeneous route, i.e. through a sharp reaction front, as is the case with the FeS_2 nanocrystals. This sharp reaction front allows for the formation of a concentration gradient within the structure, leading to internal strain. Since this type of reaction occurs during the lithiation of the FeS_2 nanocrystals these findings are applicable.

Previous work has also demonstrated that anisotropic expansion of a material during electrochemical reaction can dramatically influence the fracture behavior. Specifically, fracture preferentially occurred at the surface of crystalline Si nanopillars between preferentially-expanding crystal facets.[15,16,55] In contrast, amorphous Si has been observed to undergo isotropic expansion, and it is much more resistant to fracture.[30] This observation of anisotropic behavior in an amorphous material is similar to the behavior seen in the sodiation and potassiation of FeS_2. The more amorphous nature of the reacted product could result in isotropic expansion effect, however in both of these reactions a sharp reaction front is still seen, unlike in amorphous Si nanoparticles, leading one to conclude that this is not solely responsible for the fracture resistance observed. Overall,

our observation of fracture at the corners of FeS_2 cubes during lithiation is consistent with prior work, but the differences among different alkali ions has not been observed.

4.5.3 Effect of Rate and Particle Size on Fracture Behavior

These experiments also provide information related to rate and size effects on fracture. The fracture process for the two-phase reactions reported here appears to be insensitive to reaction rate or phase transformation kinetics. This is because the evolved stress depends primarily on the extent of reaction, since the concentration of alkali ions in the reacted phase is approximately constant.[58] Reaction rates were generally faster for lithiation compared to sodiation and potassiation, but rates also varied among different particles for a given alkali ion as shown in Figure 4.15 which shows plots of reaction kinetics. However, only lithiation (with varying reaction rates) resulted in fracture, indicating that reaction kinetics do not play a significant role in the fracture process. Regarding size effects on fracture, some smaller lithiated FeS_2 crystals avoided fracture (as shown by the statistics in Fig. 4.4g). This is consistent with prior research, as a similar size dependence for fracture during the first lithiation has also been reported for nanoscale crystalline Si particles and wires. For Si, however, fracture can be avoided altogether for sizes < ~150 nm.[16,119] In general, smaller particles contain less total deformation-induced strain energy to drive the formation of new crack surfaces, which reduces the probability that the particles will fracture. This analysis suggests that regardless of the active ion used, there will be a critical size above which fracture will occur. For the sodium and potassium experiments discussed here, the critical size was evidently not reached. Beyond avoiding

mechanical degradation, the use of very small (~5 nm) FeS_2 crystals has previously been suggested to be beneficial for long-term cycling because the particle size is on the same length scale as the diffusion length of Fe during reaction, enabling facile conversion.[64] Thus, both chemical and mechanical aspects of electrochemical reactions must promote stability for effective long-term cycling.

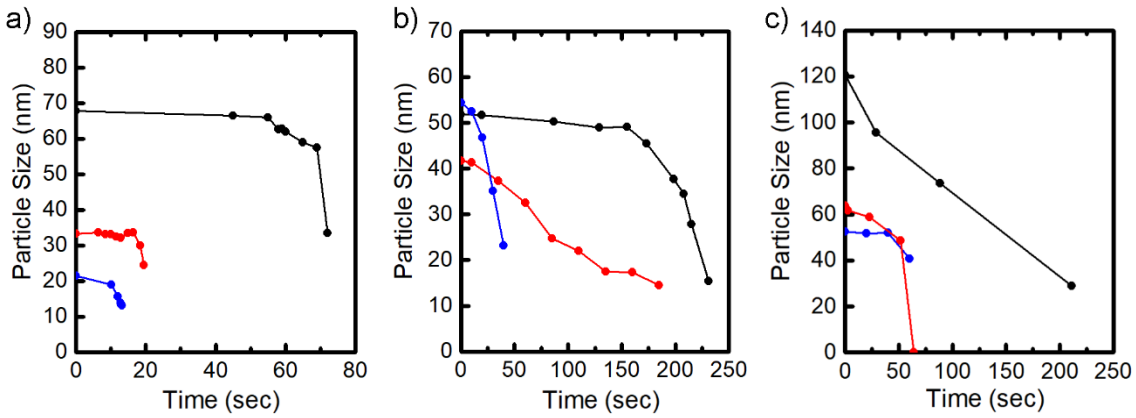

Figure 4.15: Measurements of the size of the internal FeS_2 crystal during reaction of individual particles with Li^+ **(a)**, Na^+ **(b)**, and K^+ **(c)**. The measurements do not go to zero in most cases because the internal crystal size was not able to be measured after a certain extent of reaction (*e.g.*, due to fracture and/or rotation of the particle). Na^+ and K^+ reactions were generally slower than Li^+ reactions; however, for a given alkali ion, the reaction rates varied from particle to particle. Reaction rates in these *in situ* experiments can depend on various factors, such as the distance of the particle from the ion source.

4.6 Modeling Stress Evolution During Reaction

To quantify the effects of crystal shape evolution on stress during reaction, chemomechanical simulations were carried out using the finite element method to model concurrent ion transport, reaction front migration, volume expansion, and stress generation with the help of collaborators at Georgia Tech. These simulations captured the two-phase

reaction at sharp phase boundaries through the use of concentration-dependent diffusivity, as previously demonstrated.[120] To specifically compare the effects of reaction front shape on stress evolution, simulations were carried out with the same volumetric expansion (using a representative volume expansion value of 2.2) but with different reaction front shapes. Since the magnitude of volume expansion influences stress evolution, simulating the same volume expansion enables direct comparison of the effects of reaction front shape. More details on the simulation model constructed can be seen in Appendix A.1.

Chemomechanical simulation results are shown in Figure 4.16 for a cubic particle in the midst of reaction. Considering the symmetry of reaction and stress generation with respect to the {100} cube faces, we only modeled one-eighth of a cube, as schematically shown in Fig. 4.16a. Here, the red outer boundary represents the particle surface and the blue internal boundary approximates the position of the reaction front; the solid red lines denote the boundary of the modeled region. Figure 4.16b-c show simulation results for the case of lithiation, in which the reaction front is aligned with the {100} facets and the unreacted crystalline core has sharp corners. The contour plot of the normalized Li concentration in Fig. 4.16b shows that there is a sharp increase in Li concentration at the reaction front, and three mutually perpendicular {100} reaction fronts intersect to form a sharp corner of the unlithiated core. A contour plot of the lithiation-induced hydrostatic tensile stress is shown in Fig. 4.16c. Note that the hydrostatic tension becomes the in-plane tension near free surfaces, such that its contour plot can effectively reveal the three-dimensional, symmetric distribution of surface tensile stresses around a corner of the cubic particle. Figure 4.16c shows that large tensile stress concentrations arise around the surface locations that coincide with the underlying sharp corner of the unlithiated core, and they

are induced by the large expansion near the intersecting {100} reaction fronts during lithiation. Such stress concentrations can drive fracture at the edge or corner of FeS_2 particles, as observed during *in situ* TEM experiments. In contrast, Fig. 4.16d-e show simulation results for the case of reaction front evolution with a "blunted" reaction front shape (as is the case with sodiation and potassiation). The contour plot of the normalized Na/K concentration (Fig. 4.16d) shows that the corner of the unreacted crystal core has been rounded off to feature a less-sharp reaction front angle. The corresponding contour plot of the hydrostatic tensile stress is shown in Fig. 4.16e. Comparing Fig. 4.16c and e, the stress concentrations at the particle surfaces are weaker for the rounded reaction front (sodiation or potassiation) compared to the sharper corner (lithiation). This manifests as tensile stress that is more spatially distributed and lower in magnitude (Fig. 4.16e). These simulations are consistent with the TEM observation of fracture in lithiated FeS_2 particles as opposed to the lack of fracture in sodiated and potassiated FeS_2 particles. Table 4.1 contains values of the maximum tensile stress during reaction for both cases, and these data show that the cubic reaction front produces higher stresses throughout the reaction.

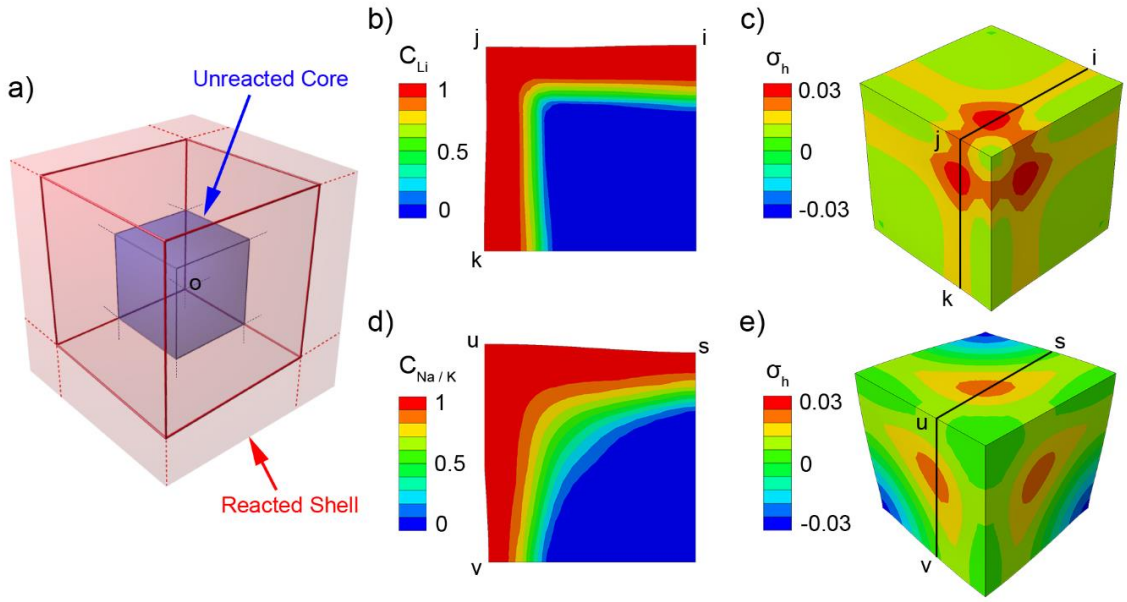

Figure 4.16: Chemomechanical finite element simulation results showing stress generation during reaction of a cubic FeS_2 particle with different reaction front shapes. **(a)** Schematic of two-phase lithiation/sodiation, with a sharp reaction front (colored in blue) between a cubic unreacted core and a lithiated/sodiated/potassiated shell (colored in red). Only one-eighth of the cubic particle is modeled (outlined by the solid red lines), given the symmetry of the reaction and stress generation processes. The "*o*" symbol marks the center of the full cubic particle. **(b, c)** Simulation results of the reaction when the inner crystal retains a cubic shape with a sharp corner (*i.e.*, the lithiation case). A contour plot of Li concentration C_{Li} (normalized by the concentration of Li at the full extent of lithiation) at a representative cross section is shown in (b), and a contour plot of hydrostatic tensile stress σ_h (normalized by Young's modulus) is shown in (c). The position of the cross section in (b) is marked by the black lines in (c). **(d, e)** Simulation results of the reaction when the inner crystal develops a rounded-off or blunted corner (*i.e.*, sodiation or potassiation). A contour plot of ion concentration $C_{Na/K}$ at a representative cross section is shown in (d), and a contour plot of hydrostatic tensile stress σ_h (normalized by Young's modulus) is shown in (e). The cross section in (d) is marked in (e).

Table 4.1: Maximum surface hydrostatic stress at varying extents of reaction for the two modeling simulations considered: 1) an internal crystal with a cubic shape and 2) an internal crystal with a rounded shape. The extent of reaction is defined as the ratio of the volume of the reacted region to the total volume, in which the reacted region is defined as where the normalized ion fraction is greater than 50% of the maximum. These hydrostatic stress quantities are given as fractional values of the Young's modulus. The cubic crystal with sharper corners shows larger stress values in all cases.

	Extent of Reaction				
	0.14	**0.18**	**0.21**	**0.25**	**0.28**
Cubic, σ_h	0.0146	0.0216	0.0307	0.0329	0.0332
Rounded, σ_h	0.0002	0.0024	0.0114	0.0204	0.0279

4.7 Conclusions

Similar to the previous chapter, this study has revealed the different nanoscale reaction pathways that occur during lithiation, sodiation, and potassiation of FeS_2 using a combination of *in situ* TEM, chemomechanical modeling of stress evolution, electrochemistry, and mechanical testing. FeS_2 nanocrystals were observed to undergo conversion-type reactions via a two-phase mechanism with the movement of a sharp reaction front in all cases. The key result of this study is that despite significantly larger volume changes during sodiation and potassiation, particles were only observed to fracture during lithiation. This result runs counter to conventional wisdom that suggests that larger volume changes in battery materials necessarily lead to larger stresses and more significant mechanical degradation. The shape of the reaction front was quantified and was found to

contribute to these differences in mechanical failure; the reaction front during lithiation was found to maintain a rectangular shape with {100} facets, while the reaction front during sodiation and potassiation evolved to an oval shape with blunted corners. Chemomechanical modeling of stress evolution showed that a rectangular phase front should lead to higher tensile stresses at the corners/edges of particles, which leads to fracture as observed in the lithiation case. It is also possible that differing fracture toughness of the various product phases contribute to the divergent fracture behavior.

Similar to the study conducted on the Cu_2S conversion-type material, FeS_2 nanocrystals demonstrated behavior that was drastically changed by the increase in the alkali-metal ion size. In both cases the increase of the ion alters the reaction pathway, both leading to a new morphological evolution process. Interestingly, while the volumetric expansions were a great deal larger in the sodiation/potassiation reaction, the difference in the structural evolution leads to more stable morphologies. These findings are important since they indicate that even though high-capacity alloying and conversion materials exhibit larger volume changes in Na-ion and K-ion battery systems, these volume changes may be manageable and do not necessarily induce particle failure. As demonstrated herein, it is critical to understand how detailed nanoscale reaction mechanisms influence morphological changes; this information can then be used to tailor the shape, size, and structure of materials for batteries. The discovery of the different nanoscale reaction pathways in FeS_2 crystals and how these pathways influence fracture is a critical step towards engineering these materials for use in next-generation Na- and K-based battery systems.

CHAPTER 5. SPONTANEOUS AND REVERSIBLE HOLLOWING OF ALLOYING MATERIAL WITH LITHIUM

5.1 Introduction

As has been previously discussed, high-capacity anode materials for Li-ion batteries have long been held back by limited cyclability caused by large volume changes during ion insertion and removal. Previous chapters have examined the nanoscale reaction mechanisms that these types of materials undergo in effort to better understand the effect these large-volume-changes have on the cyclability. However, these materials undergo the displacement and conversion-type reaction mechanism. In this chapter the high-capacity alloying material antimony was examined during reaction with lithium. Antimony is known to have a theoretical specific capacity of 660 mAh/g after full reaction of the Li_3Sb which occurs at around 1.0 V, other phases are possible and are discussed in section 1.5, however this study observed the direct reaction to Li_3Sb.[74–76] Previous studies have found that monodispersed Sb nanocrystal electrode leads to better cycle life that larger Sb nanocrystals.[74] However, the mechanistic reasons underlying this improved cycling behavior remain unclear, as the high surface area of small nanocrystals can often result in poor CE and cycling behavior.[34,79]

Here in this study, *in situ* transmission electron microscopy (TEM) was used to demonstrate that solid Sb nanocrystals spontaneously form uniform voids during lithium removal, and that these voids are reversibly filled and vacated during further electrochemical cycling. Void growth was found to be due to the presence of a thin and

resilient native oxide shell that accommodates the initial particle expansion but acts as a mechanical constraint to prevent shrinkage of the particle upon delithiation. This spontaneous hollowing was found to be size-dependent, with Sb particles <~30 nm forming voids but with larger particles simply shrinking and mechanically buckling or crumpling the shell. A chemomechanical model was developed that explained both the hollowing behavior and the observed size dependence, and conventional electrochemical tests confirm that this behavior results in improved CE and cyclability. These new findings demonstrate that small Sb particles exhibit transformation mechanisms that are fundamentally superior to those of many other alloy anode materials, and this behavior may obviate the need for complex nanoscale processing for next-generation, high-energy battery anodes. These results emphasize the importance of understanding the nanoscale reaction mechanisms of these types of large-volume-change electrode materials.

5.2 *In Situ* TEM of Lithiation and Delithiation

5.2.1 Cycling Behavior

For this study Sb nanocrystals with a 15.7±2.5 nm diameter were synthesized using a liquid-phase organometallic synthesis described in Chapter 2 by my collaborators from ETH Zurich.[74] After synthesis TEM images and XRD was performed on the nanocrystals (Figure 5.1a and b), and a histogram of the particles was also taken to find the average size of the synthesized particles. Figure 5.1b shows an *ex situ* XRD trace of the synthesized nanocrystals confirms the rhombohedral structure of this material (space group $R\bar{3}m$, ICDD 04-007-9028).

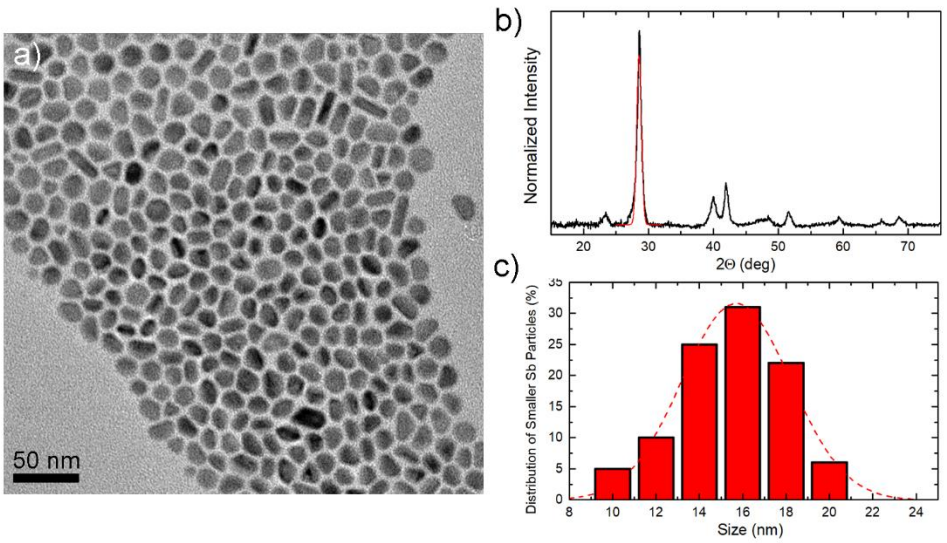

Figure 5.1: (a) TEM image of the smaller Sb nanocrystals. **(b)** XRD trace of the smaller particles showing the $R\bar{3}m$ rhombohedral structure. The Gauss fit of the main Bragg reflection reveals that the average size of the Sb crystalline domain is 11 nm. **(c)** Histogram of the synthesized particles showing the distribution of particle size, including oxide layer.

In situ TEM was carried out to observe the nanoscale reaction mechanisms of these Sb nanocrystals with Li.[85] These experiments utilized a probing-biasing TEM specimen holder, in which a tungsten probe covered with metallic lithium was brought into contact with a TEM half-grid on which Sb nanocrystals were dispersed (Fig. 5.2a). A bias was then applied to drive Li^+ through the oxide layer on the surface of the lithium metal, and the ions were reduced and diffused through the carbon film on the half grid to react with the Sb nanocrystals (see Chapter 2 for details).[25,31] As seen in the previous chapters these type of *in situ* TEM techniques have been used to investigate the reaction mechanisms of large-volume-change battery materials with various alkali ions.[29,31,42,88,104,119,121–123]

Figure 5.2b-e shows morphological transformations of a group of Sb nanocrystals during cycling. In this experiment, the Li probe contacted the edge of the carbon support film less than 1 μm from the bottom of the image frame. The pristine Sb nanocrystals (Fig. 5.2b) are spherical or oval and have a ~2 nm thick native oxide. A high resolution TEM image of a pristine Sb nanocrystal and this oxide layer can be seen in Fig. 5.9b later in section 5.2.3. Fig. 5.2c shows the same nanocrystals after lithiation, which involved a measured volume expansion of the Sb by a factor of 2.4 ± 0.2. The contrast of the lithiated particles is lighter because of the uptake of Li, and the oxide shells on the particles also grew in thickness (from ~2 nm to ~5 nm) due to reaction with Li. The bias was then reversed to remove Li, and the delithiated particles are shown in Fig. 5.2d. The delithiated particles exhibit a unique morphology that consists of a hollow shell of Sb at the inner surface of the oxide layer. Instead of simply shrinking in size during delithiation, as observed in other alloy materials,[29,30] a single void formed within the center of most particles, while the oxide layer did not appreciably change dimensions. The spontaneous formation of voided particles during delithiation was observed across all experiments (>10 experiments and hundreds of particles visualized). Some particles in Fig. 5.2d show two or three voids separated by Sb ligaments, but 92% of particles formed single voids over all experiments. Interestingly, upon the second lithiation (Fig. 5.2e), the outer ring of Sb expanded to fill the interior void in each of the particles without mechanically disrupting the outer oxide layer.

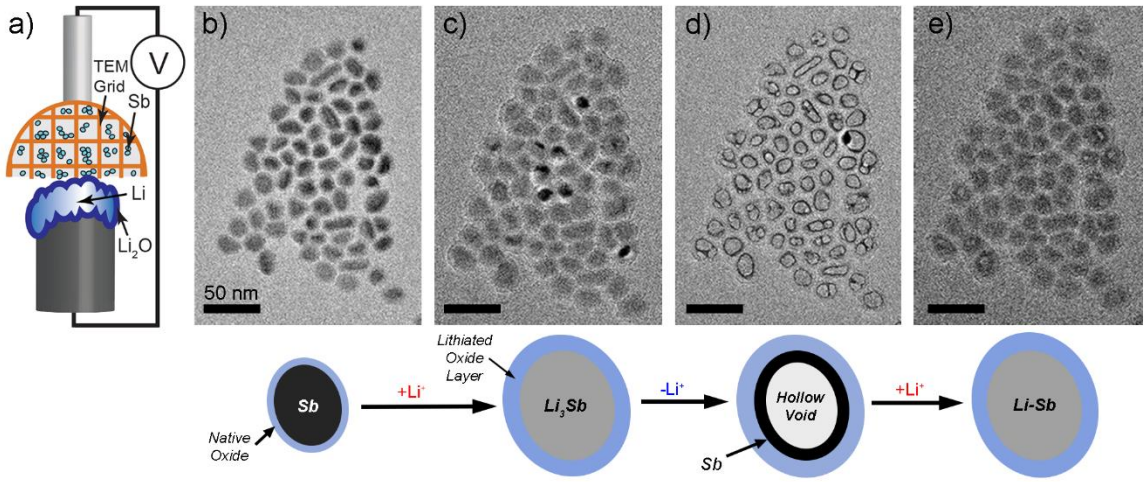

Figure 5.2: (a) Schematic of the *in situ* TEM experimental setup. **(b-e)** TEM images of a group of Sb nanocrystals during cycling with Li. **(b)** Sb nanocrystals prior to reaction, **(c)** after lithiation, **(d)** after delithiation, and **(e)** after second lithiation. These images and the schematics below the images show the expansion of the particles during lithiation (c), the formation of a hollow Sb shell at the inner surface of the surface oxide during delithiation (d), and expansion into the void during relithiation (e).

Additional experiments were performed during which the particles were cycled up to six times, revealing that the cyclic void formation and filling persisted during further cycling up to six full cycles in Figure 5.3. Throughout the six cycles performed within the TEM, no substantial changes in the overall volume occur after the after the initial expansion. Thus, after the first delithiation step, the Sb within these particles is able to expand and contract within the outer oxide shell without the shell substantially changing dimensions. This easily reversible hollowing behavior is ideal for stable SEI growth necessary to enable efficient battery cycling.

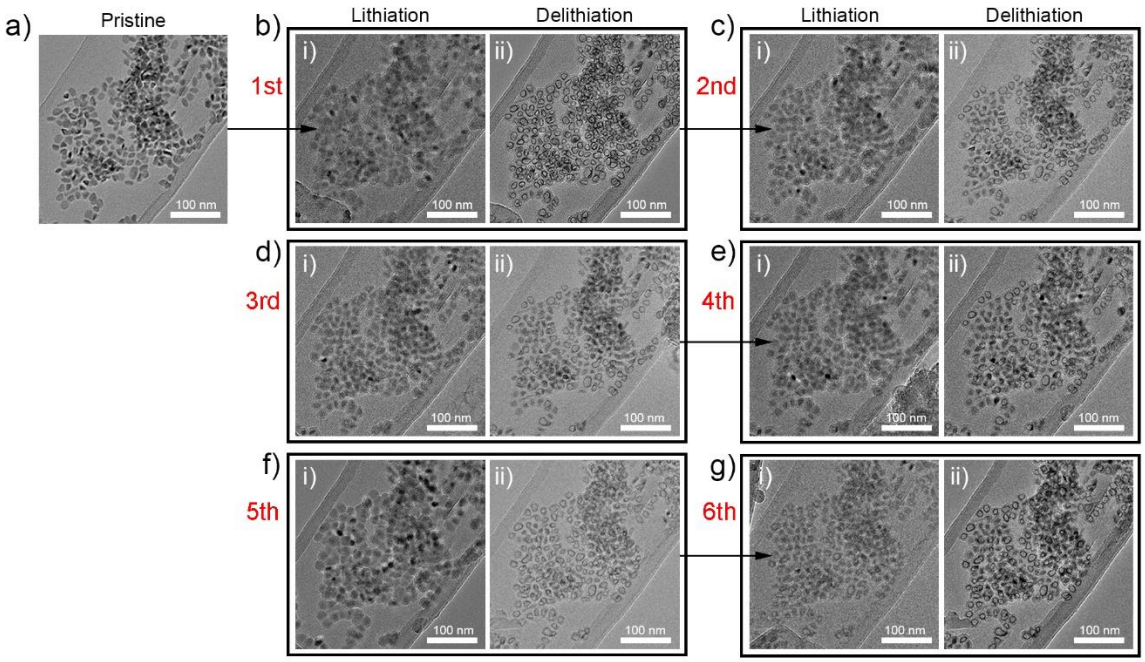

Figure 5.3: Morphology evolution of a larger group of Sb nanocrystals during repeated cycling. **(a)** Group of pristine Sb crystals before cycling. **(b)** The same cluster after the first lithiation (i) and delithiation (ii). **(c)** After the second lithiation/delithiation. **(d)** After the third lithiation/delithiation. **(e)** After the fourth lithiation/delithiation. **(f)** After the fifth lithiation/delithiation. **(g)** After the sixth lithiation/delithiation. Some particles in the large group are not fully lithiated or delithiated each cycle, resulting in a lack of volume change or hollowing behavior during that cycle.

5.2.2 Delithiation Process Analysis

To understand how the void formation during delithiation occurs further analysis was performed. Figure 5.4a-d shows a series of TEM images from a different experiment than those in Figure 5.2. The particles in Fig. 5.4a begin lithiated and most particles are completely solid, but some have small remaining voids from previous cycling. During delithiation in Fig. 5.4, particles visible across the frame begin to form voids at different times as Li is removed from them. During the initial 30 s of delithiation (Fig. 5.4b), voids

form and grow steadily in some particles, while other particles remain solid. After about 35 s of the experiment, voids have formed in many of the remaining particles (Fig. 5.4c), and these voids grow faster than those nucleated previously. After 63 s (Fig. 5.4d), almost all the particles are fully delithiated and feature the Sb layer at the inner surface of the outer oxide shell; these delithiated particles did not noticeably shrink in overall volume. The oxide shell remaining after delithiation is particularly visible in Fig. 5.4d on the particles at the top of the frame along the edge of the carbon support. Only a few particles remain void-free and lithiated at this point.

Individual void nucleation and growth events in the three characteristic particles are shown in the image snapshots in Fig. 5.4e-g. In the particles in Fig. 5.4f and 5.4g, voids are observed to grow completely within ~5 s after nucleation *via* the expansion of the dark Sb-rich ring near the void surface. The growth of the darker ring indicates that Li is mostly removed from a region within a few nanometers of the void surface, and this delithiated layer propagates into the Li-Sb. Voids likely nucleate at the interface between the Li-Sb and the oxide shell, as seen in Fig. 5.4e and f, but this is difficult to determine conclusively since nucleation at the top and bottom interfaces cannot be distinguished.

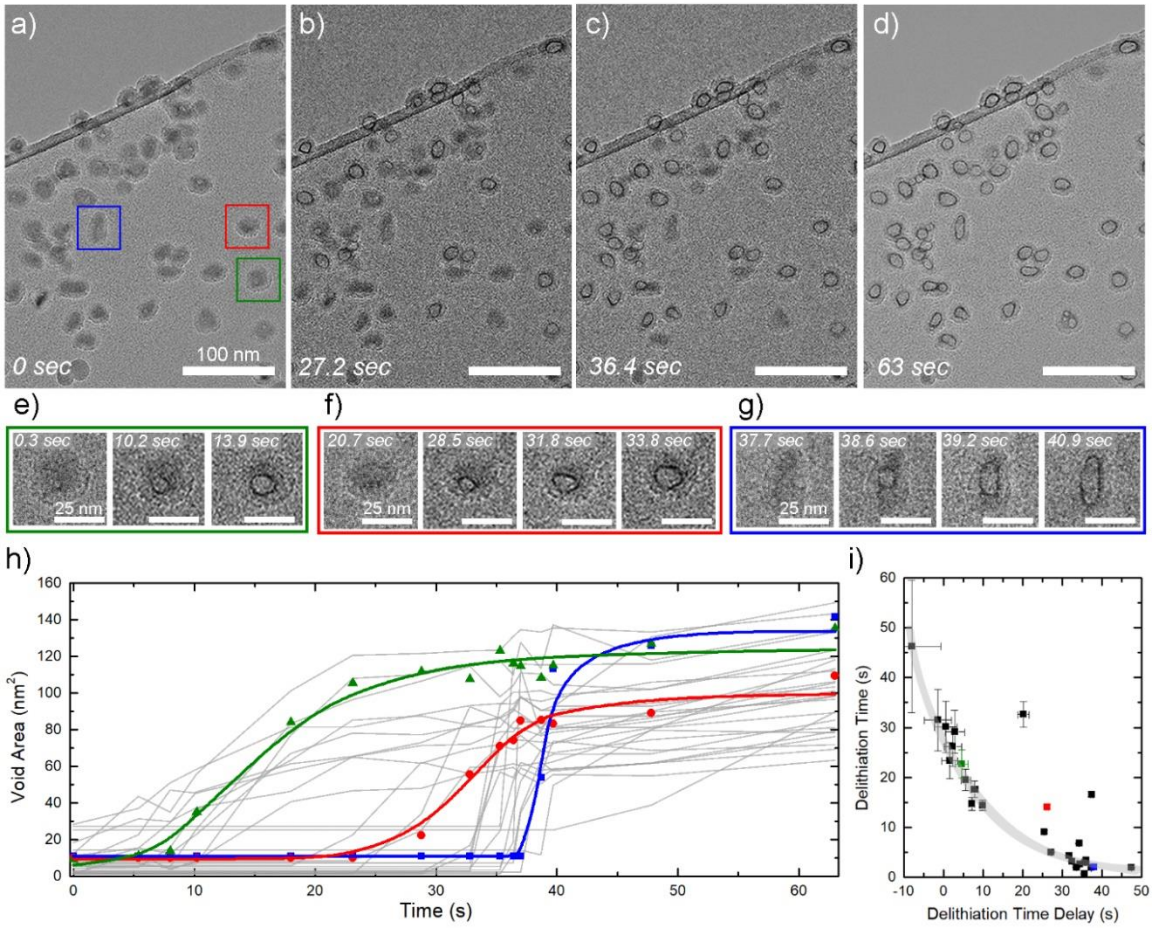

Figure 5.4: Analysis of the delithiation process of a group of Li-Sb nanocrystals. **(a-d)** Time-series of delithiation. Voids nucleate and grow in the particles at various times, resulting in the final sample (d) in which almost all particles have formed hollow singly-voided structures. **(e-g)** Magnified snapshots of three different particles, as denoted by the colored boxes in (a) and colored datasets in (e, f), showing the nucleation and growth process of the void in each particle. **(h)** Plot of the measured void area within each particle in the frame as a function of time. The three colored datasets correspond to the particles with colored boxes in (a), and these are fit and overlaid with a sigmoidal growth function. **(i)** Time required for delithiation of each of the particles extracted from each sigmoidal fit as a function of the delay from the beginning of the experiment; this plot shows that faster void growth occurs in particles that delithiate later. The gray shaded trajectory is a guide for the eye.

Figure 5.4h displays a plot of the measured void area within each of the particles with time. Each of these void growth trajectories was found using segmentation analysis. The segmentation analysis workflow is detailed in Figure 5.5. First, contrast was optimized in each frame using the MATLAB "imadjust" function (Fig. 5.5a). Next, ImageJ software was used to segment the pixels in the image as either belonging to the Sb-rich material, the oxide shells, or the vacuum/carbon background using the trainable Weka segmentation tool.[91,124] This was done by manually assigning different sample regions a "class" in the software, which then segments the image based on the manual selections (Fig. 5.5b). Based on each classifier, the probability that each pixel belongs to one of these defined "classes" is determined and is displayed on a 32-bit hyperstack.[91] The resulting probability map was then filtered of noise and binarized (Fig. 5.5c and d), leaving just the segmented delithiated Sb seen in Fig. 5.5e.

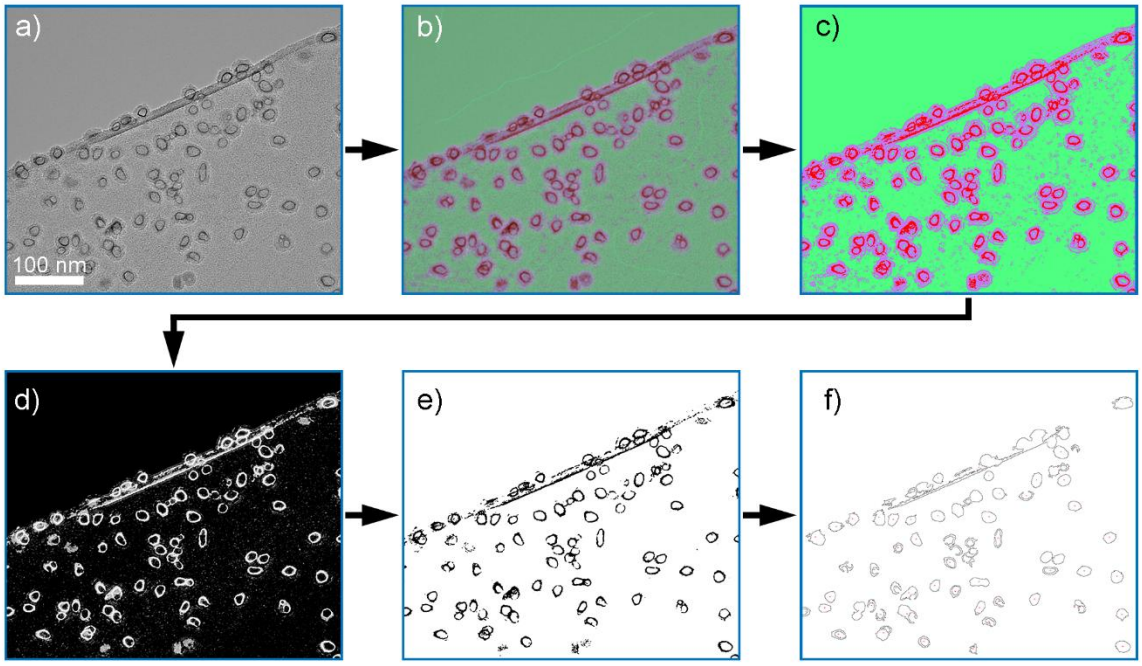

Figure 5.5: Example process flow for segmentation analysis of the data in Fig. 5.4. **(a)** TEM image of delithiated particles. **(b)** Overlay of a color map on the with three segmented categories: The dark Sb phase (red), the oxide shells (pink), and the background of vacuum and carbon (green). **(c)** Color map of the three segmented categories. **(d)** Probability map derived from the color map of the Sb classifier; this map shows only the Sb phase with some errors at the edge of the carbon grid. **(e)** The probability map from (d) after thresholding and binarization. **(f)** A pixel count was performed on the binarized image to obtain the particle size measurements. This was done automatically using ImageJ "Analyze Particles" function which counts the number of pixels that makes up each individual cluster, which it then labels as an individual "particle" and marks on the map in (f).

These segmented regions were then used for the measurements in Fig. 5.4h and Fig. 5.7. The void area with time in Fig. 5.4h is fit with the sigmoidal growth function,

$$y = \frac{A_1 - A_2}{1 + (x/x_0)^p} + A_2, \qquad \text{(Eq. 5.1)}$$

where y is the void area at a given time, A_1 and A_2 are the minimum and maximum void area, x is the time, x_0 is the time of the inflection point where $y = \frac{A_2 - A_1}{2}$, and p is the power parameter that represents the steepness of the growth function. To estimate delithiation time and time delay, we fitted a line to the growth region of the sigmoidal function (Equation 5.1). For the linear fits, we used three points, corresponding to 20%, 50%, and 80% of overall growth. The delithiation time delays thus correspond to the times where the linear fits are equal to A_1 parameters of the respective sigmoidal growth functions and the delithiation time delays correspond to a difference between times when linear fits are equal to the A_2 and A_1 parameters of the respective sigmoidal growth functions (both are shown plotted against each other in Fig. 5.4i). Several characteristic trajectories were selected and are shown overlaid as the colored trajectories in Fig. 5.4h. The selected particles' delithiation processes are individually shown in Fig. 5.4e-g. Fitting enabled quantification of the delithiation velocity of each particle, as represented by the power parameter *p* in the sigmoidal function (Fig. 5.6). This analysis showed that voids that formed earlier grew more slowly, while voids that formed in particles after ~30 s grew more quickly (Fig. 5.4i).

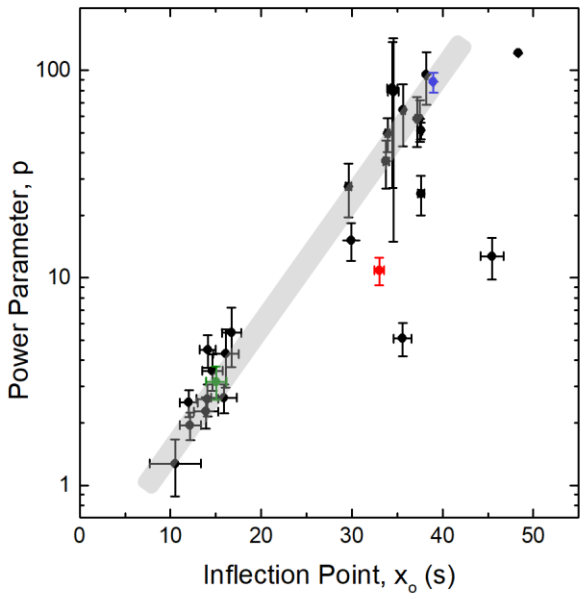

Figure 5.6: Plot of the power parameter, *p*, *vs.* the position of the inflection point (in seconds), x_0, from the sigmoidal growth curves in Fig. 5.4h. The fitting equation is Eq. 5.1. Each point corresponds to the growth trajectory of an individual void within a particle in Fig. 5.4h. Higher power parameters correspond to a steeper sigmoidal function and faster void growth. This plot shows that voids that form later in the experiment grow faster. The colored points correspond to the colored traces in Fig. 5.4h. The gray shaded trajectory is a guide for the eye.

Finally, Fig. 5.7 shows a plot of the volume of the Sb shell after delithiation *vs.* the volume of the initial lithiated Sb for each particle in the frame. These data reveal an average volume ratio of the Li-Sb to the delithiated Sb of 2.0±0.1, which is close to the theoretical value of 2.35. The average area of the initial Li-Sb cores was found to be only ~9% larger than the total areal contained within the delithiated shell. These measurements confirm that this darker shell is in fact delithiated Sb and that the overall particle size is largely unchanged during delithiation.

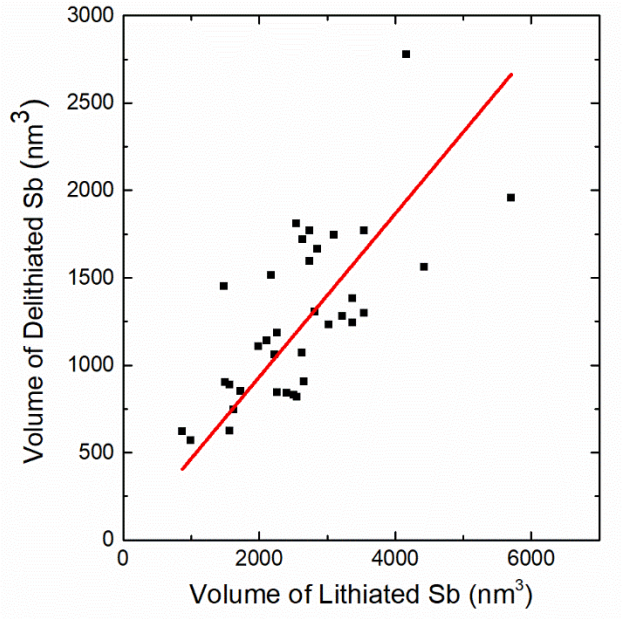

Figure 5.7: Plot of the volume of the delithiated Sb *vs.* the initial volume of the lithiated Sb for each particle in the frame in Figure 5.4. The volume of the delithiated Sb shells and the Li-Sb particles was estimated by assuming the shape of a spherical shell and sphere, respectively. The red line is a linear fit to the data.

From the detailed segmentation and analysis of these image data discussed above it was concluded that there was seemingly no preferred void nucleation site within particles and no effect of particle shape on void nucleation. Furthermore, there is no obvious dependence of the void nucleation events on the position of the particles with respect to the counter electrode (which was to the upper right of the frame) or with respect to each other. Without further information regarding local potential or mass loss from the particles, it is difficult to conclusively determine the origin of the faster delithiation of particles later in the reaction process. Since these particles do not form voids until later during this process, it is probable that more Li has been removed from these particles while they still retain their initial volumes. This would result in greater strain energy and a larger effective

driving force for void formation, which could influence void growth kinetics. More details related to the void growth mechanism will be discussed in the following sections

5.2.3 Structural Evolution During Reaction

Next the structural evolution of the Sb nanocrystals as they were lithiated and delithiated was examined. During *in situ* TEM cycling, SAED data was collected and several patterns at different points during the reaction can be seen in Figure 5.8. Plots of the integrated diffraction intensity vs. the scattering vector Q (nm^{-1}) taken from the patterns in Figure 5.8 are shown in Figure 5.9a. The plot from the unreacted particles shows diffraction peaks arising from the rhombohedral Sb structure (Fig. 5.8a and Fig. 5.9a, black trace). A typical pristine Sb particle with the non-crystalline native oxide layer is shown in Fig. 5.9b. After full lithiation, the crystalline Sb signal has disappeared, and peaks associated with the Li_3Sb phase have arisen, along with a strong Li_2O peak at ~3.75 nm^{-1} (Fig. 5.9a, red trace). The Li_3Sb phase is the thermodynamically expected phase for full lithiation of Sb. Li_2O is present because the initially amorphous Sb-oxide shell reacts *via* a conversion reaction to form Li_2O and Li-Sb phases. These observations are consistent with previous electrochemical studies which have reported the formation of Li_3Sb and Li_2O from Sb nanocrystals.[74] Upon delithiation (blue trace in Fig. 5.9a and SAED pattern in Fig. 5.8c), only peaks from Li_2O are visible. Thus, the surface oxide remains at least partially as Li_2O after delithiation; we also note that there may be Li_2O formed on the surface of the carbon grid.[31] Regardless, this indicates that the dark-contrast Sb shells that remain after delithiation are amorphous.

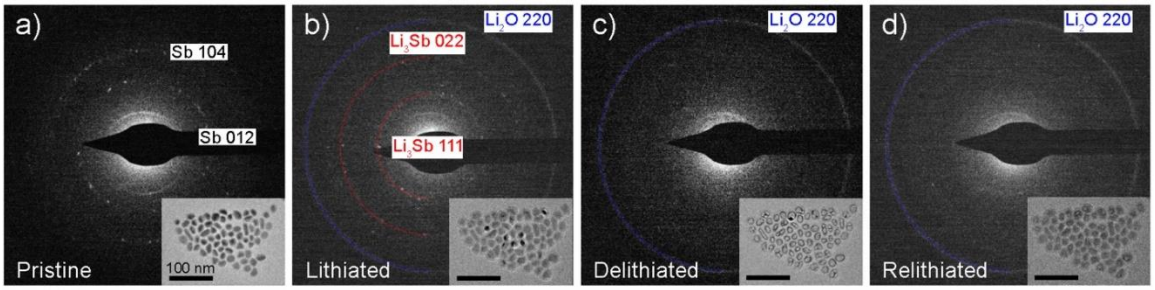

Figure 5.8: Selected area electron diffraction (SAED) patterns from an *in situ* SAED experiment with Sb particles along with the corresponding images. **(a)** SAED pattern of the pristine Sb nanocrystals with crystalline rings corresponding to the rhombohedral Sb structure (space group $R\bar{3}m$, ICDD 04-007-9028). The (012) ring corresponds to a d-spacing of 3.00 Å and the (104) ring corresponds to 2.13 Å. **(b)** SAED pattern after lithiation showing diffraction rings (3.80 Å and 2.32 Å) corresponding to the cubic Li_3Sb phase (space group $Fm\bar{3}m$, ICDD 96-153-7887), as well as another ring (1.66 Å) from polycrystalline Li_2O (space group $Fm\bar{3}m$, ICDD 04-004-4918). **(c)** SAED pattern of the delithiated cluster of nanocrystals with only the ring from Li_2O visible. **(d)** SAED pattern corresponding to the relithiated particle with no detectable Li_3Sb rings present, but with the Li_2O phase remaining.

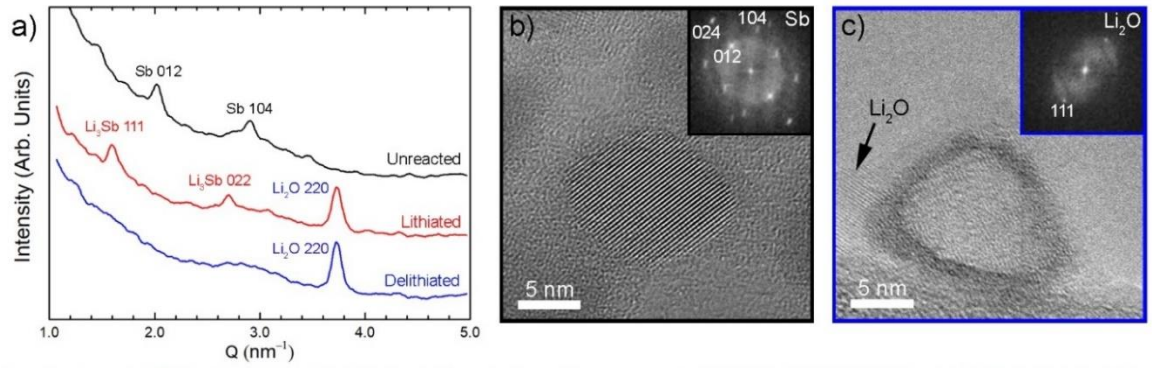

Figure 5.9: Structural evolution of nanocrystals and larger nanoparticles. **(a)** Integrated intensity of SAED patterns of the group of nanocrystals in Fig. 1 at various stages during cycling. **(b)** High-resolution TEM image of a pristine Sb nanocrystal; the FFT inset shows intensity resulting from the crystalline Sb phase. **(c)** High-resolution TEM image of a

delithiated nanocrystal; the darker ring is the Sb layer, which is surrounded by the lighter oxide layer. The visible lattice fringes in this layer and the inset FFT confirm that Li_2O is present.

To determine the composition of the dark-ring within the oxide layer, high-magnification images of a delithiated particle were taken and are shown in Figure 5.9c. This image shows the amorphous Sb layer inside the outer oxide shell, in which a Li_2O crystallite is visible. The Sb ring was found to be 4.1 ± 0.9 nm thick when averaged over the 37 delithiated particles seen the image in Fig. 5.4d. To confirm that Sb was still present within the shell morphology, *ex situ* energy-dispersive X-ray spectroscopy (EDS) was conducted on particles delithiated using the same cycling conditions (See Fig. 5.10). The STEM-EDS was conducted on an aberration-corrected JEOL 2200FS S/TEM at 200kV at Oak Ridge National Laboratory following *in situ* TEM cycling experiments with a FEI Titan S 300kV S/TEM using a similar probing/biasing specimen holder (Nanofactory Instruments). After cycling the Sb particles, the holder was removed from the microscope and placed in an argon-filled purge box. Samples were removed from the probing/biasing holder and loaded into a standard specimen holder for the JEOL instrument, which was sealed with an O-ring and then loaded into the TEM. The cycled specimen was exposed to air for less than 1 min during this transfer process. EDS HyperMaps were acquired using a Bruker-AXS silicon-drift detector system (SDD) with a nominal current of 140 pA.

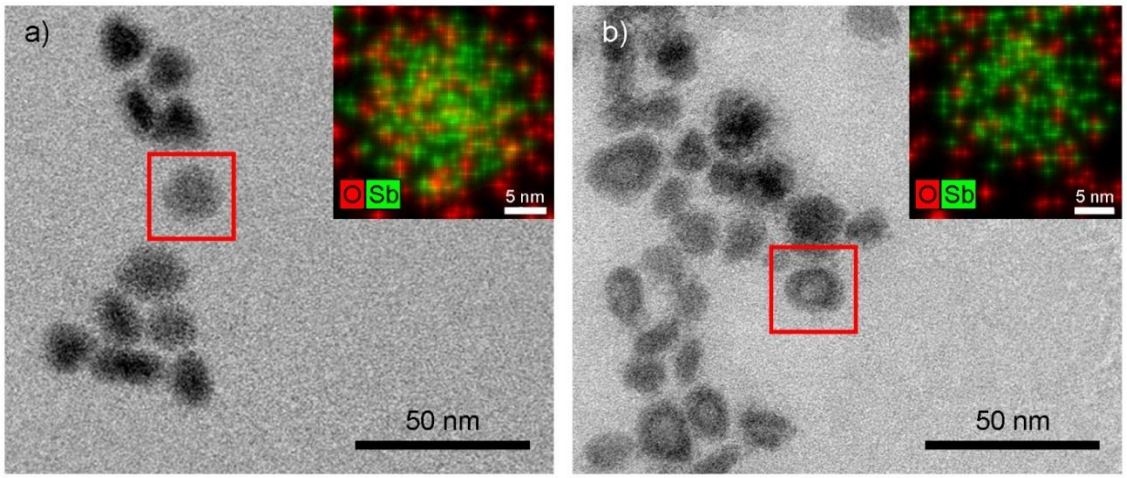

Figure 5.10: *Ex situ* scanning TEM energy dispersive X-ray spectroscopy (EDS) of delithiated Sb particles. **(a)** BF-STEM image of a cluster of unreacted Sb nanocrystals. The inset of (a) shows STEM-EDS data of the pristine Sb nanocrystal highlighted with the red box in (a). The EDS data show strong Sb signal (green) within the interior of the particle. **(b)** BF-STEM image of a particle that was lithiated and delithiated using *in situ* TEM, then removed from the microscope and moved through air to the STEM (the thicker morphology of the voided particles was consistently observed to be due to exposure to air). The inset of (b) shows STEM-EDS data of the delithiated particle within the red box. A slightly weaker Sb signal was detected within the interior where the void was formed, and the Sb is still present.

This analysis confirmed that Sb made up the darker region of the delithiated particles. This thin ring was concluded to be amorphous in nature due to the fact that no diffraction signal not crystalline planes could be seen after multiple tests. It was hypothesized that the thin nature of the Sb ring along with its adhesion to the outer oxide, as well as possible Li or O dopants, are likely responsible for its amorphous structure. Additional cycling was performed on the cluster of nanocrystals from which the SAED data were collected, and the Li_3Sb phase was not detected after the second and subsequent

lithiation steps (Fig. 5.8). Instead, only Li_2O was detected, suggesting that the oxide layer structure remains unaffected by any subsequent cycling. Frustrated crystallization of the Li_3Sb phase may be due to sub-stoichiometric lithiation, even though imaging showed significant volume expansion during subsequent lithiation steps (Fig. 5.2).

5.2.4 Particle Size Effect

To examine the effect that particle size has on the reaction process, larger Sb particles were synthesized and electrochemically cycled using similar TEM experiments. These particles were prepared with significantly wider size and shape distribution due to deliberate changes in the synthetic procedure and can be seen in Figure 5.11 to still be the same pristine Sb material.

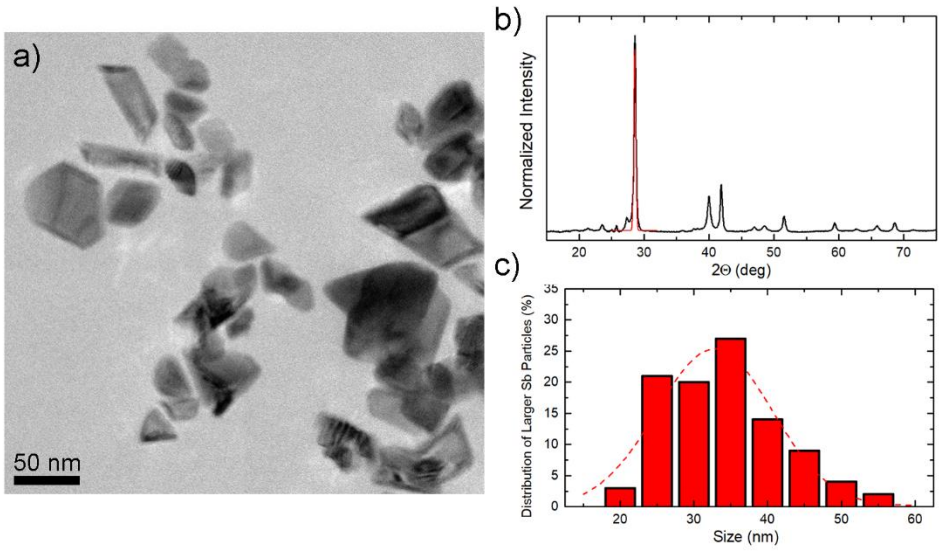

Figure 5.11: (a) TEM image of the larger Sb nanoparticles used for in situ TEM. **(b)** XRD trace showing that the larger Sb particles have the same structure as the smaller Sb nanoparticles. The Gauss fit of the main Bragg reflection reveals that the average size of

the Sb crystalline domain is 24 nm. **(c)** Histogram showing the distribution of particle sizes for the larger particles.

Figure 5.12a and b show a SAED pattern and an image of a cluster of larger Sb particles; After lithiation, these particles expanded to form the alloy phase, which has a lighter contrast due to the high Li content and also has an oxide layer visible on the surface (Fig. 5.12c). After delithiation (Fig. 5.12d), voids are observed within the interior of the smallest particles in the upper part of the image. However, most of the larger sections of these particles contracted and densified without forming interior voids, as seen in the middle particles in Fig. 5.12d. Figure 5.12e shows that much of the Sb was amorphous after delithiation, similar to the smaller particles (although a few diffraction spots are visible). These findings indicate that a critical size exists below which void formation is favored rather than particle contraction.

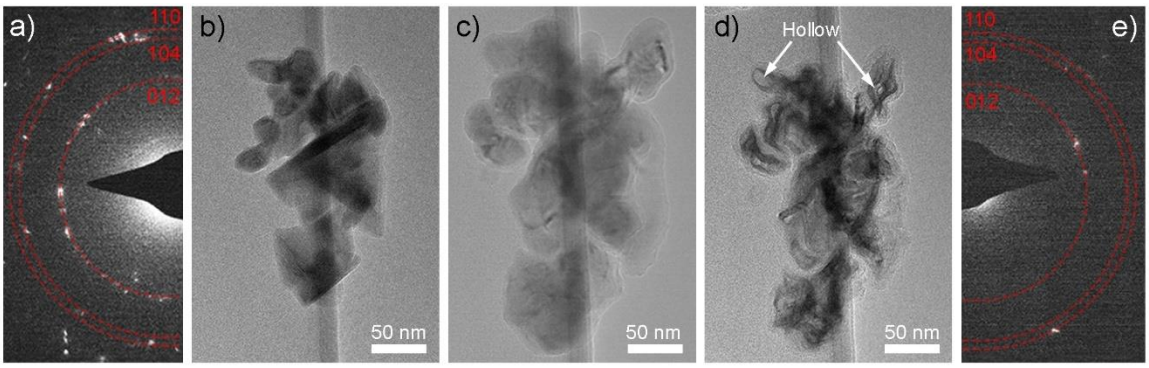

Figure 5.12: (a) SAED of larger pristine Sb nanoparticles supported at the edge of the carbon TEM grid. **(b)** Image of larger Sb particles of various non-uniform sizes and shapes. **(c)** The same group of larger particles after lithiation and volume expansion. **(d)** The same particles after delithiation. Most portions of the particles contract and remain dense, while

regions of initial size less then ~30 nm show evidence of hollow void formation. **(e)** SAED after delithiation, in which a few Sb diffraction spots remain.

Additional *ex situ* TEM experiments were also performed with the smaller Sb nanocrystals to determine whether the *in situ* cycling conditions contributed to the morphological changes. Here, Sb nanocrystals were deposited on a Cr-coated TEM grid and were cycled once as the active electrode in a conventional Li half-cell with a liquid electrolyte. To perform these experiments Cr was sputtered on carbon grids using a Unifilm Sputtering system. DC magnetron sputtering was performed under Ar plasma with a current of 0.045 A and a voltage of approximately 98 V using a 3-inch Cr source (Kurt Lesker, 99.95%). The base pressure was below 8×10^{-6} Torr and the process pressure was 5×10^{-3} Torr. The deposition rate was fixed at 0.1 nm/min, and the final thickness was around 20 nm. The Sb nanoparticles were then drop-cast onto the Cr-coated TEM grids inside an Ar-filled glove box.

Electrochemical tests used for the *ex situ* TEM were performed using CR2032 stainless-steel coin cells (MTI Corp.). The Cr-coated TEM grids on which the Sb nanocrystals were deposited were used as the active electrode with a stainless-steel current collector. Lithium metal (Sigma-Aldrich, 99.9%) was scraped clean of surface oxides, attached onto a stainless-steel current collector and used as the counter/reference electrode. A polymer separator film (Celgard) was soaked in electrolyte (1.0 M $LiPF_6$ 1:1 v/v ethylene carbonate/diethyl carbonate, EC/DEC, battery grade, Sigma-Aldrich) and used in each cell. These cells were assembled within an Ar-filled glove box (Vigor) with H_2O and O_2 levels <0.5 ppm and <0.1 ppm, respectively. The electrochemical tests were conducted on a Bio-

Logic VMP3 potentiostat at room temperature. The voltage was swept from open circuit to 200 mV at a rate of 1 mV/sec and held for 3 h. The voltage was then swept up to 2.0 V at the same rate and held there for an additional 3 h. This process caused lithiation and delithiation of the very small Sb mass on the working electrode. The cycled cells were then opened in the glove box and the grids were cleaned using 1,2-dioxolane (Sigma-Aldrich) and allowed to dry.

After a complete cycle, the TEM grid with the Sb nanocrystals deposited on it was removed from the coin cell in an Ar-filled glove-box and washed prior to being imaged. *Ex situ* imaging, seen in Figure 5.13, suggested that hollow void structures were also formed in these particles. Although the images feature poor contrast due to the relatively thick underlying Cr layer (20 nm) that was necessary to ensure electrochemical reaction and SEI growth, many of the particles show apparent void morphologies. The three particles at the bottom of the circled region have similar hollow morphologies to the particles shown in Fig. 5.10b, which was an *in situ* sample that was also transported through air for imaging; the air exposure slightly changed the morphology compared to *in situ* samples. The speckled contrast on the grid is the Cr layer. These results are important because they show that the hollowing transformation can occur even in the presence of liquid electrolyte and with SEI formation. Finally, void formation was observed in *in situ* TEM experiments in areas that had never been exposed to the electron beam, indicating that beam exposure did not play a significant role in morphology evolution

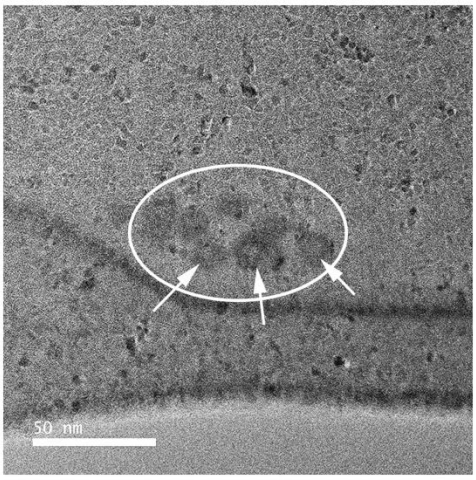

Figure 5.13: *Ex situ* TEM image of Sb particles that were electrochemically lithiated and delithiated within a conventional liquid-electrolyte coin cell with a lithium metal counter electrode.

5.3 Effect on Electrochemical Cycling

After confirming that the morphological changes that took place during the *in situ* TEM experiments occurred in electrochemically cycled lithium half-cells a series of *ex situ* electrochemical experiments were conducted to understand the effect these changes have on the cycling behavior. Sb-based working electrodes were constructed using three different forms of antimony active material for further comparison. These electrodes consisted of either small monodisperse Sb nanocrystals (~15 nm, including oxide layer), larger polydisperse nanoparticles (randomly distributed between 40 and 140 nm, see Fig. 5.14) or "bulk" Sb (325 mesh). The nanocrystals and nanoparticles to be used in the electrochemical studies first underwent ligand exchange.[125] 10 mL of Sb nanocrystals or larger nanoparticles in chloroform (~20 mg/mL) was mixed with 10 mL of K_2S (95%, Strem Chemicals) in formamide (99.5%, Sigma-Aldrich, ~5 mg/mL). The mixture was

stirred at room temperature for 1 h to allow complete phase transfer of the Sb material from chloroform to formamide. The formamide phase was then separated using a centrifuge and re-dispersed three times in toluene (99.5%, Sigma-Aldrich). The Sb material was then precipitated in ~10 mL of acetonitrile (99.5%, VWR) through centrifuging, and then re-dispersed in deionized water for use in the electrode slurries.

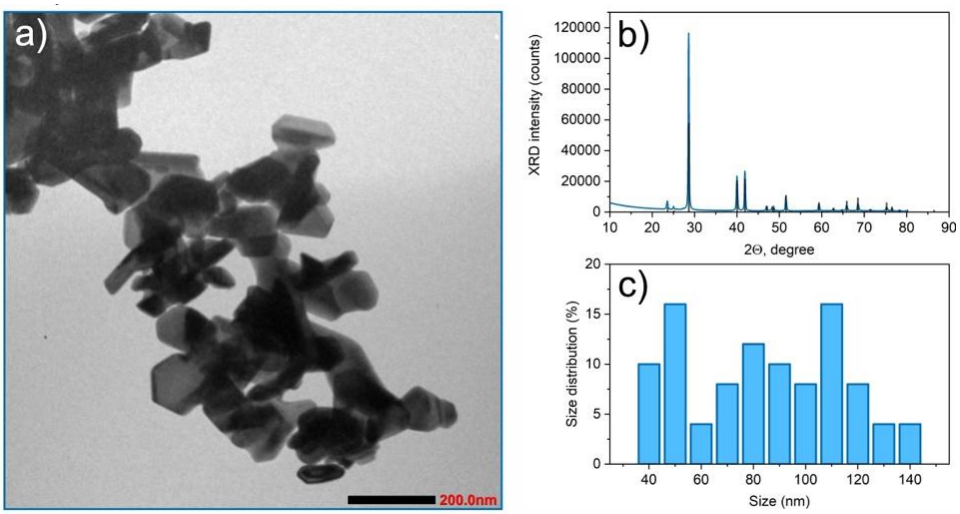

Figure 5.14: Characterization of larger nanoparticles synthesized via multiple injections for use in conventional electrochemical testing. **(a)** TEM image showing polydispersity. **(b)** X-ray diffraction shows that the material is single-phase Sb. **(c)** Histogram of particle size showing that the size is randomly distributed from 40 nm to 140 nm.

Electrode slurries were fabricated using 64 wt % active material, 21 wt % carbon black (Super P, TIMCAL), and 15 wt % sodium carboxymethyl cellulose binder (CMC, Sigma-Aldrich). These values were chosen to ensure sufficient electronic and ionic transport. The overall mass loading of active material was between 0.5 and 1.0 mg cm^{-2} in each cell. Slurries were made using deionized water and then spread onto a copper foil that was first cleaned using acetone, methanol, and isopropanol. After spreading the slurry, the

foils were heated at 80 °C in an oven for 12 h to dry. Electrode disks were punched and calendared using a roll press (MTI Corp.). Half cells with Sb working electrodes and Li foil counter electrodes were constructed using CR3032 stainless-steel coin cells (MTI Corp.) within an Ar-filled glove box (Vigor). Glass microfiber disks (GE Healthcare) were used as separators. The electrolyte was a 1.0 M $LiPF_6$ solution in a 1:1 v/v mixture of ethylene carbonate and dimethyl carbonate (EC/DMC, 99%, Sigma-Aldrich) with 3 wt % of fluoroethylene carbonate (FEC, 99%, Sigma-Aldrich). These cells were sealed with a hydraulic press within the glovebox. Galvanostatic electrochemical tests were performed using a Landt Battery Testing System at room temperature with voltage limits set between 0.05 V and 2.0 V versus Li/Li^+.

Figure 5.15a-c show galvanostatic discharge/charge curves for each type of electrode at a rate of 66 mA g^{-1} (C/10). All three samples show an initial discharge plateau at ~0.8 V vs. Li/Li^+ and a charge plateau at ~1.0 V vs. Li/Li^+. These features are ascribed to the lithiation of Sb and crystallization into the Li_3Sb phase, followed by two-phase removal of Li during delithiation. The small nanocrystals show a higher plateau (~0.8-1.4 V vs. Li/Li^+) during the initial discharge that corresponds to the conversion of the surface oxides to a lithiated phase (Fig. 5.15a). This feature is also observed in the data from the larger nanoparticles (Fig. 5.15b), but with a lower associated specific capacity because of the lower surface area of the larger particles. The oxide reaction is barely visible in the bulk particles (Fig. 5.15c). The oxide reduction process is clearly not reversible in the nanocrystals (Fig. 5.15a), with a first-cycle CE of 61%. This provides further evidence that the oxide shells retain their composition after the first lithiation (i.e., the Li in the shells is

not removed during delithiation), in agreement with the *in situ* TEM experiments that showed that the lithiated shells maintained their thickness and morphology during cycling.

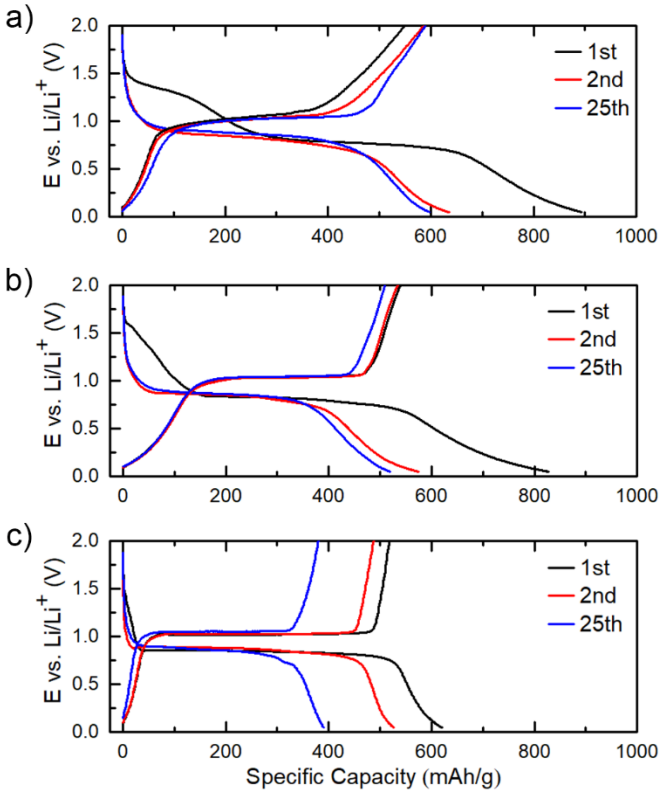

Figure 5.15: (a-c) Galvanostatic curves obtained at a current of 66 mA g^{-1} (C/10) from electrodes containing (a) 15 nm monodisperse nanocrystals, (b) 40-140 nm polydisperse nanoparticles, and (c) "bulk" particles (black: first cycle; red: second cycle; blue: 25th cycle).

To determine how the Sb nanocrystal electrode batteries compare to other antimony cells long cycle tests were performed. With cycling, both the small nanocrystals and larger nanoparticles exhibited specific capacity near the theoretical value (660 mAh g^{-1}) over >100 cycles, while the bulk particles showed steady capacity decay (Fig. 5.16a). Several sample corresponding galvanostatic curves at 1C shown in Fig. 5.16b-d and show the fast

capacity decay of the bulk antimony electrodes while the nanocrystals settle into a reversible galvanostatic profile even at these relatively fast rates of 1C. Both the nanocrystals and the larger nanoparticles consistently showed good cyclability when tested at a variety of rates (Fig. 5.17 shows data from many cells). This enhanced cycle life of nanoscale vs. bulk particles agrees with prior work by He et al which demonstrated that nanocrystal Sb electrodes exhibit this high rate capability and capacity retention demonstrated in this work as well.[74]

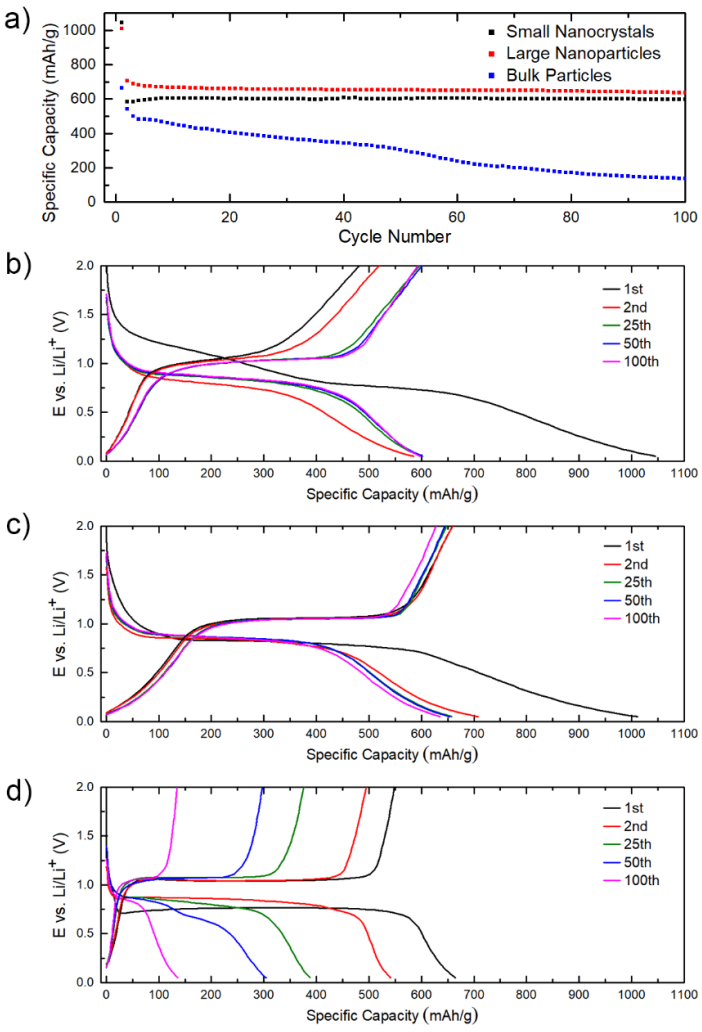

Figure 5.16: (a) Specific capacity with cycling at a current of 660 mA g^{-1} (1C) for the three types of electrodes. **(b-d)** Galvanostatic curves at a rate of 1C (660 mA g^{-1}) for Sb-based

electrodes corresponding to the specific capacity plots in (a). **(b)** Small ~15 nm monodispersed nanocrystals, **(c)** large 40-140 nm polydisperse nanoparticles, and **(d)** bulk 325 mesh particles.

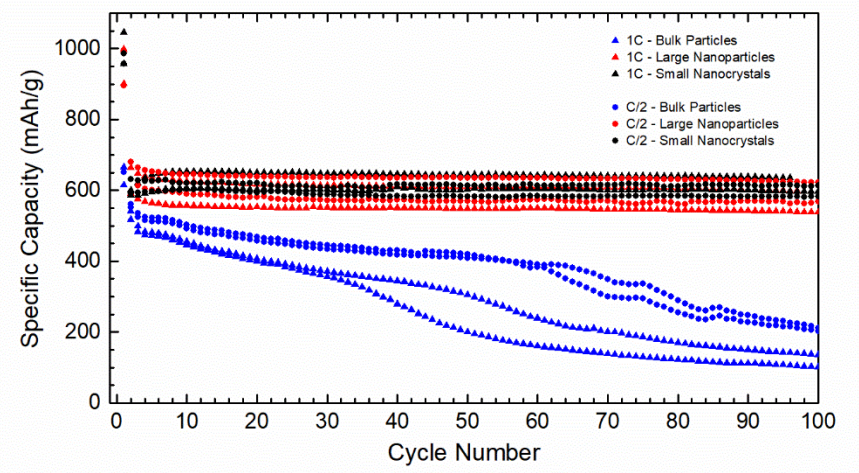

Figure 5.17: Specific capacity with cycling of Sb-based electrodes from multiple cells showing consistently long cycle life of the nanocrystals and larger nanoparticles. The electrodes were tested at 1C (triangles) or C/2 (circles).

The key new finding of these electrochemical investigations is related to the differences in CE with cycling of the different electrodes, and particularly the small nanocrystals vs. the larger nanoparticles. Figure 5.18 shows how the CE evolves with cycling at a charge/discharge rate of 660 mA g^{-1} (1C) for each of the three types of Sb electrodes. Critically, the smallest nanocrystals show consistently higher CE after the first few cycles compared to the larger nanoparticles. After ~30 cycles, the CE stabilizes with the smallest particles showing an average CE of 99.4%. After ~50 cycles, the larger nanoparticles begin to stabilize and show an average CE of 98.7%, almost a full percentage point lower than the smaller particles which show more reliable hollowing behavior. Both

types of smaller particles have higher CE than the bulk particles. Even though both the small and larger nanoparticles show excellent capacity retention during cycling in half cells, this higher CE value for the smallest particles means that an electrode would last approximately twice as many cycles before 80% capacity decay in full cells when compared to the larger nanoparticles. Further increases in CE could be achieved by tailoring electrolyte composition. This data represents the average of at least five cells to show the generality of these observations.

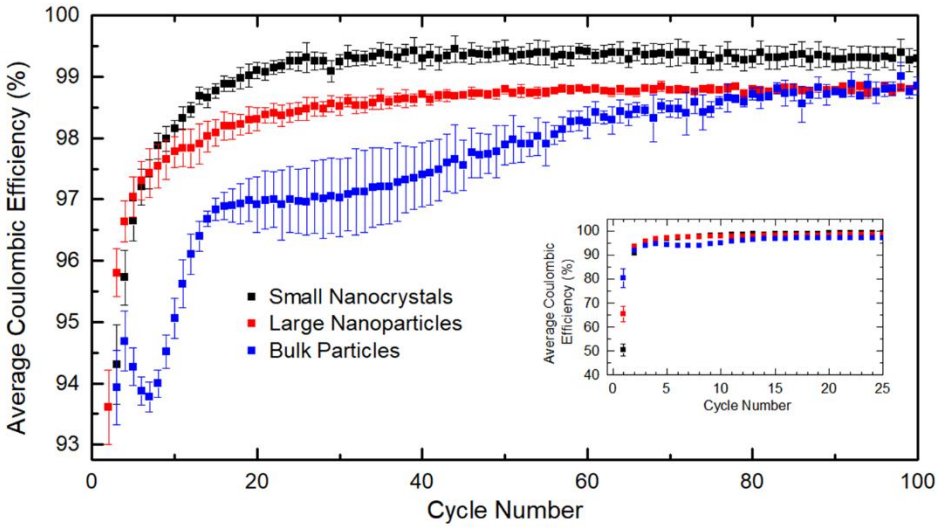

Figure 5.18: Coulombic efficiency of the three types of electrodes over 100 cycles at 1C. Each dataset is averaged over multiple cells (9 cells for the small nanocrystals, 7 cells for the large nanoparticles, and 5 cells for the bulk particles), with error bars representing the standard deviation for each cycle. The inset shows the same data but with an expanded range to show the CE of the first cycle.

The hollowing/refilling transformation observed with *in situ* TEM in the smallest particles (but not in the larger particles) likely plays a key role in enabling the higher

observed CE. After the first lithiation, the static outer surfaces of the smallest particles allow for the SEI to stabilize, while the continuous dimensional changes of the surfaces of the larger particles continue to promote SEI growth over many cycles, resulting in lower CE values. This result is particularly striking given the higher surface area of the smallest crystals; if SEI was growing at the same rate in the small and larger nanoparticles, the CE of the small particles would be expected to be much lower because of the higher surface area upon which SEI can grow. The high CE of these small nanocrystals is impressive when compared to a wide variety of other alloy anode materials; as an example, other small alloying nanoparticles exhibit rapid capacity decay when used without modification as can be seen in a study by Liu et. al.[36] that showed untreated silicon nanocrystals around the same size, after only a few cycles, experienced capacity retention of less than 50% the material initial discharge capacity. The unique hollowing/refilling process observed in the smallest Sb nanocrystals is clearly useful to enable superior cycling stability.

5.4 Chemomechanical Model of Void Formation

In order to explain these experimental observations of void growth a chemomechanical model was created by our collaborators in Prof. Ting Zhu's group here at Georgia Tech. This model specifically describes how the mechanical constraint of the oxide layer cause the smaller particles to form the voids seen during delithiation, while the larger particles experience buckling and collapse of the oxide layers to allow for particle shrinkage without void formation. A schematic showing these two possible reaction pathways can be seen in Figure 5.19, with pathway 1 representing the smaller particle

reaction and pathway 2 representing the buckling seen for the larger particle reaction. As Li is removed from the fully-reacted Li-Sb alloy particles, the Li-Sb phase in the core begins to shrink in volume, theoretically resulting in compressive stress within the outer oxide layer. In turn, the oxide layer applies increasing tension to the internal Li-Sb phase, which is approximately hydrostatic due to the uniform removal of Li at these small length scales. In the early stages of this process (*i.e.*, before void nucleation or oxide layer buckling), this situation can be considered to be similar to a spherical pressure vessel containing negative pressure.

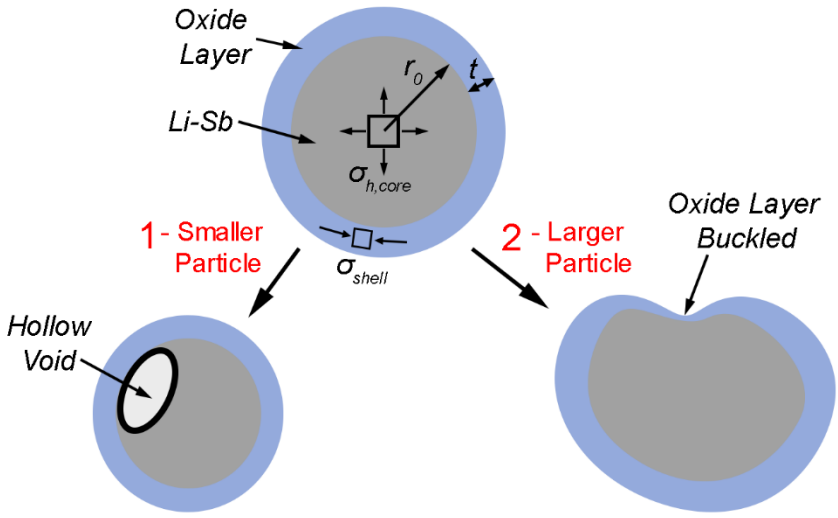

Figure 5.19: Schematic of two possible morphological trajectories during delithiation. As Li^+ is removed from the Li-Sb phase under constraint from the oxide (top), the Li-Sb alloy experiences hydrostatic tensile stress ($\sigma_{h,core}$) while the oxide shell experiences compressive stress σ_{shell}. As these stresses increase during delithiation, the morphological result can either be a hollow void that grows within the Li-Sb (pathway 1) or the buckling of the oxide shell and particle shrinkage (pathway 2).

5.4.1 Strain Energy Inducing Void Formation

In this situation, void formation within the Li-Sb phase can be energetically advantageous because it relieves strain energy within the particle core. However, void formation also involves the creation of new Sb surfaces, which results in an energy penalty equal to the void surface area multiplied by the surface energy γ_s. Here, the strain energy within the Li-Sb core of the particle changes was derived as a function of volumetric strain within the core. This analysis is purely linear-elastic and therefore does not capture plastic deformation/flow during Li removal. However, it does provide an estimate for the elastic strain energy magnitude expected in particles of different sizes early in the Li removal process, which is the pertinent aspect for our analysis. We first write the differential internal energy dU for the Li-Sb particle core as

$$dU = -\sigma_h dV, \qquad \text{(Eq. 5.2)}$$

where σ_h is the hydrostatic stress and dV is the differential volume. We can further write σ_h as

$$\sigma_h = -B\left[\frac{\Delta V}{V_0}\right] = -B\left[\frac{V-V_0}{V_0}\right]. \qquad \text{(Eq. 5.3)}$$

Here, B is the bulk modulus (we use 42 GPa, which is the value for pure antimony),[126,127] and $\Delta V/V_0$ is the volumetric strain. We define V_0 as the initial volume of the fully alloyed Li-Sb core of the particle. V is the ideal strain-free volume of the core after a certain amount of Li is removed (*i.e.*, the core shrinks); this theoretical volume change is shown in Figure 5.20a, b. In our model, hydrostatic tensile stress σ_h arises because the core is constrained to retain the same volume V_0 by the external shell even as Li is removed (Fig. 5.20c). We

note that with this convention, $V < V_0$ during delithiation, resulting in a positive value for tensile stress in Eq. 5.3.

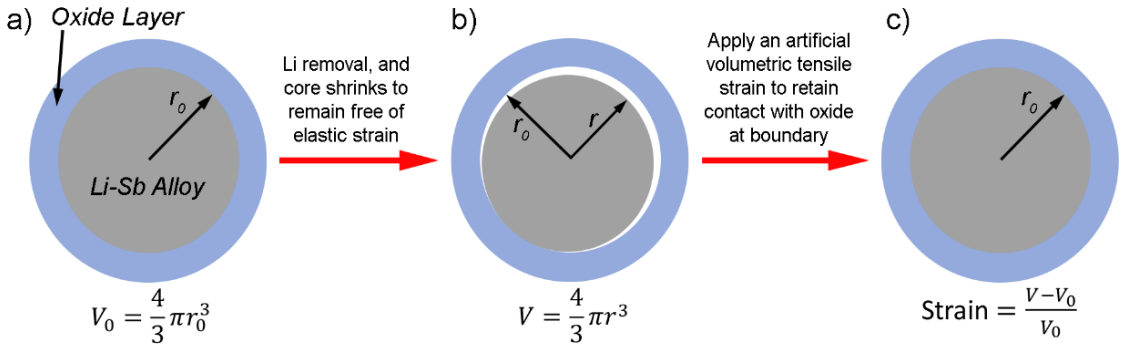

Figure 5.20: Schematics illustrating the origin of hydrostatic tensile strain within a spherical Li-Sb alloy particle during delithiation. **(a)** Schematic of reacted Sb particle after full lithiation. The volume V_0 of the Li-Sb core with initial radius r_0 is shown. **(b)** During the first stages of lithium removal from the Li-Sb particle, the Li-Sb core would shrink if we assume it is unconstrained by the oxide shell. As shown in this panel, this would result in a smaller spherical particle with radius r and volume V. In this theoretical case (unconstrained by the oxide shell), the Li-Sb remains free of elastic strain if we assume diffusion is very fast such that the particle shrinks uniformly. **(c)** In the experimental case, we observe that the oxide shell prevents contraction of the Li-Sb particle during delithiation. To model this effect, we can apply an artificial volumetric tensile strain to the Li-Sb core in (b) to expand the volume to V_0, as in (c). Thus, the end result is a hydrostatic tensile strain within the Li-Sb core.

By combining Eqs. 5.2 and 5.3, we can then write the differential internal energy as a function of elastic volumetric strain in the core:

$$dU = -\left[-B\left(\frac{V-V_0}{V_0}\right)\right]dV. \qquad \text{(Eq. 5.4)}$$

Integrating Eq. 5.4 gives the following for the internal energy as a function of strain-free volume:

$$U = B\left(\frac{V^2}{2V_0} - V + C\right), \qquad \text{(Eq. 5.5)}$$

where C is an integration constant. By considering the initial conditions $V = V_0$ when $U = U_0$, we can write

$$\Delta U = U - U_0 = B\left(\frac{V^2}{2V_0} - V + \frac{V_0}{2}\right) \qquad \text{(Eq. 5.6)}$$

Equation 5.6 gives the "strain energy," or the change in internal energy ΔU due to strain, as a function of the ideal strain-free volume of the core V. The strain energy ΔU increases due to the increase in volumetric strain within the core because the core is prevented from shrinking by the shell even as Li is removed. For a spherical particle, Eq. 5.6 can be written in terms of the radius as follows:

$$\Delta U = \frac{2}{3}\pi B\left(\frac{r^6}{r_0^3} - 2r^3 + r_0^3\right) \qquad \text{(Eq. 5.7)}$$

Given either expression for strain energy as a function of strain-free radius r or strain-free volume V, we can then find the strain at which strain energy and surface energy of newly-formed pores is equal. We approximate the surface energy of the void in a particle with initial radius r_0 as

$$E = 4\pi r_0^2 \gamma_s, \qquad \text{(Eq. 5.8)}$$

where γ_s is the total surface energy (for this model a γ_s of 0.23 J m^{-2} for pure antimony was used).[128] The surface area used here is slightly different than the true void surface area,

which would be the internal surface of the void, but this approximation captures the radius-squared dependence that dominates the total surface energy.

Based on this model, a void is favored to form when the total elastic strain energy in the constrained core exceeds the total surface energy of the new void. The energy required to form new void surfaces scales with the square of the particle radius, and thus larger particles require larger total strain energy to create new void surfaces. By setting Eq. 5.7 equal to Eq. 5.8, the critical volumetric strain required for the strain energy in the core to overcome the void surface energy can be found, which is the condition necessary for void formation. The critical strain required for a range of particle sizes can be seen in Figure 5.21 as the blue trace.

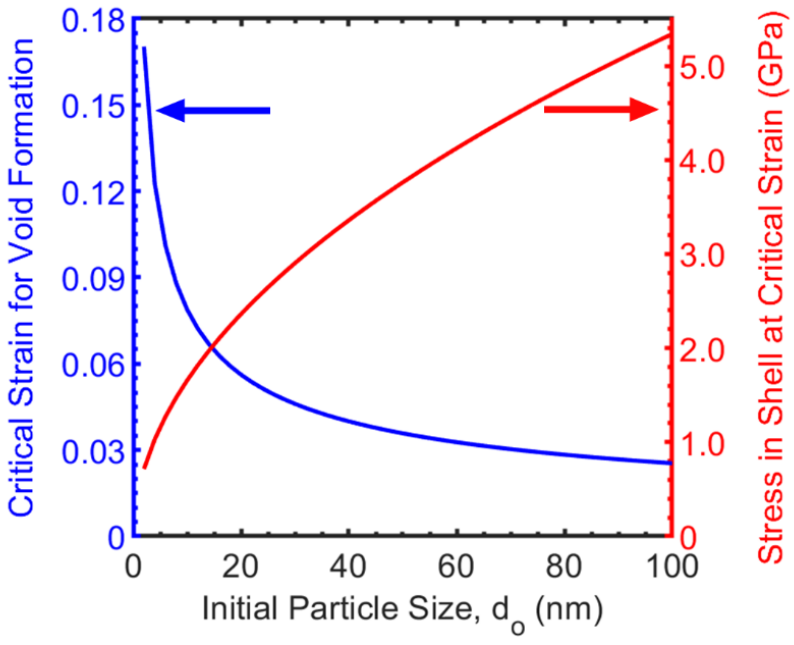

Figure 5.21: Plot of the critical strain required for void formation during delithiation as a function of initial particle diameter (blue curve, left axis) for a shell thickness of 5 nm. In

the same plot, the resulting stress in the oxide shell at this critical strain is shown as a function of particle size (red curve, right axis).

5.4.2 Stress in Oxide Shell

As mentioned at the beginning of the section 5.4, this situation can be modeled as a spherical pressure vessel in the early stages. Using the well-known mechanics of a thin-walled spherical pressure vessel,[129] we next estimate the stress within the oxide shell as a function of the volumetric strain within the Li-Sb particle core as

$$\sigma_{shell} = \frac{\sigma_{h,core} r_0}{2t} = \frac{-r_0}{2t}\left[B\left(\frac{\Delta V}{V_0}\right)\right]. \qquad \text{(Eq. 5.9)}$$

This equation relates the biaxial stress in the oxide shell σ_{shell} to the hydrostatic stress within the Li-Sb core $\sigma_{h,core}$. The initial Li-Sb core radius is given by r_0 and the oxide thickness is t (Fig. 5.19). The stress within the core is expanded in Equation 5.9 using the bulk modulus B of the metal (chosen to be 42 GPa based on that of pure Sb[126,127]) and volumetric strain $\Delta V/V_0$. Equation 5.9 shows that the stress in the shell increases as particle radius r_0 and volumetric strain increase when the shell thickness t is constant. Plotting Equation 5.9 for a variety of particle sizes and an oxide shell thickness t = 5 nm shows that larger particles generate much larger shell stresses (Fig. 5.21 and 5.22). This simple model provides a general understanding of how particle size affects stress within the shell even though the thin-wall criterion ($r_0/t \geq 10$) is not met for the smallest Sb particles, where the oxide shell thickness was ~4-5 nm and the diameter of the Li-Sb particles was 22 ± 2.0 nm.

We predict that void growth will occur in particles that exhibit sufficient volumetric strain energy to overcome the void surface energy without causing stresses to exist in the shell that are large enough to induce buckling. Prior theoretical work on elastic buckling of thin spherical shells under external pressure has shown that the critical shell stress required to cause buckling is[130]

$$\sigma_{shell,b} = \frac{E}{\sqrt{3(1-\nu^2)}}\frac{t}{r_0}, \qquad \text{(Eq. 5.10)}$$

where E is the Young's modulus of the shell and ν is Poisson's ratio. Thus, particles with greater radius r_0 can sustain lower shell stresses before buckling.

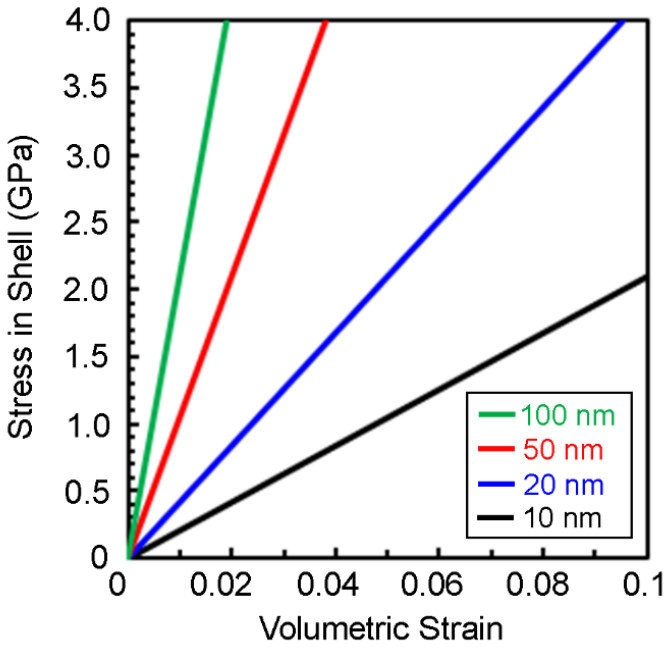

Figure 5.22: Plot of the calculated stress in the oxide shell with thickness of 5 nm as a function of volumetric strain for several different particle core diameters, as shown in the legend.

By comparing Equations 5.9 and 5.10, the tradeoff between void formation and shell buckling as a function of particle size for three different oxide layer thicknesses is shown in Figure 5.23 (t = 2, 5, and 8 nm). This plot shows the shell stress above which voids will form ($\sigma_{shell,v}$) as dotted lines, as calculated from Equation 5.9 and the volumetric strain values in Fig. 5.21. The plot also displays the shell stress above which the shell will buckle ($\sigma_{shell,b}$) as solid lines, from Equation 5.10. For smaller particles, the shell stresses at void formation $\sigma_{shell,v}$ are lower than the critical buckling stresses $\sigma_{shell,b}$ for a given shell thickness, leading to void growth during delithiation. For larger particles, on the other hand, the buckling stresses are lower than the stresses at void formation, which would favor shell buckling and particle shrinkage. The critical size below which void formation will occur is given by the crossover point of each pair of curves. This analysis leads to the conclusion that smaller particles can generate enough strain energy to drive the formation of new void surface area without generating enough stress to buckle the oxide shell, as observed experimentally. It is noted that plasticity effects could potentially shift the size-dependence of these results or reduce the maximum stresses experienced, but they would not affect the main conclusions regarding the tradeoff between void formation and shell buckling.

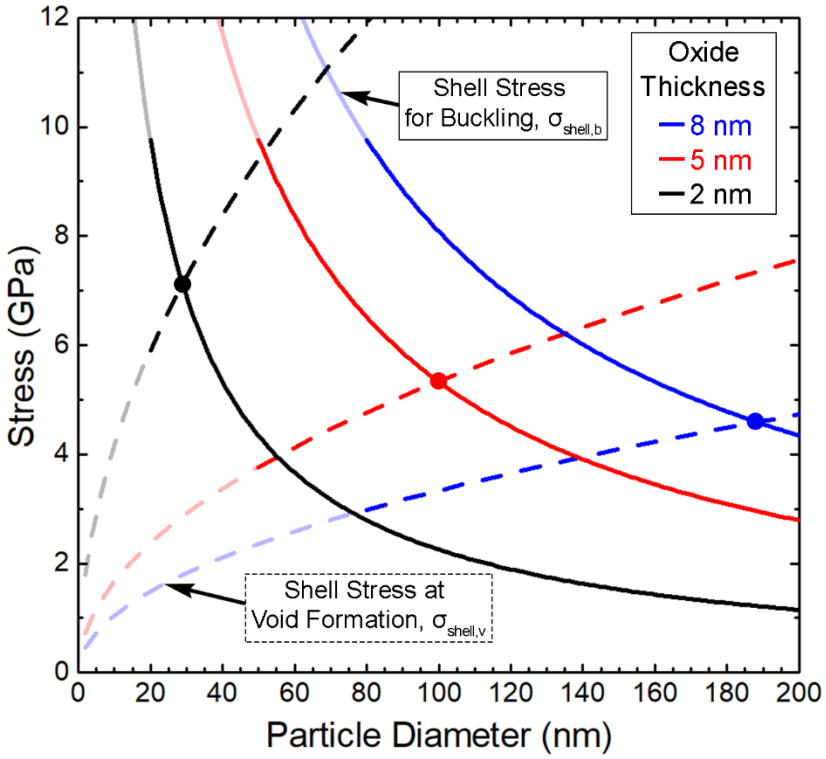

Figure 5.23: Plot of the shell stress above which voids will form ($\sigma_{shell,v}$) as a function of particle diameter for three different oxide thickness values (dotted lines), as well as the shell stress above which shell buckling will occur ($\sigma_{shell,b}$) as solid lines. For particle sizes below the crossover point of each pair of curves, void formation is favored. The $\sigma_{shell,b}$ curves are calculated with E = 100 GPa and ν = 0.2 for the Li_2O-Li_3Sb shell; these are estimates since the properties of this composite phase are not known, but the relevant trends hold for a range of chosen properties. The thin-walled pressure vessel criterion only applies when the radius of the vessel is significantly larger than the wall thickness. For this reason, the region for each oxide thickness where $r_0/t < 5$ is plotted in a lighter shade; non-uniform stresses within the shell are expected in these regions, but the general trends should remain.

Beyond explaining these experimental observations, this model provides useful predictions for development of high-performance alloy anode materials. Specifically, as

the oxide thickness t increases in Fig. 5.23, the critical size below which void formation is expected also increases. This is because thicker oxides can sustain higher stresses and can more effectively constrain the core. We note that shell thickness would need to be balanced with any impedance increases due to the thicker shells. For our nanocrystals, electrochemical impedance spectroscopy (EIS) results show that lithiation of the shell slightly increases charge transfer resistance, which then decreases after cycling (Fig. 5.24). Beyond shell thickness, shell materials that are stiffer and/or stronger would effectively raise the critical shell buckling stresses in Fig. 5.23 and could enable larger particles to undergo void formation. Buckling of spherical shells at the macroscale is known to be quite sensitive to imperfections and defects in the shell, which reduces the critical shell stress for buckling.[130] This could play a role in the observed shrinkage of the larger particles with non-uniform shapes in Fig. 5.12b-d, and it suggests that careful control over particle sphericity and shell structure/defects is necessary to promote void growth. Although this theoretical analysis is performed only considering elasticity, the size-dependence of void formation and buckling is expected to hold regardless of the precise shape of the buckling curves. Finally, this chemomechanical mechanism is distinct from the commonly-observed nanoscale Kirkendall effect, in which hollow nanocrystals can form due to differences in diffusion kinetics of different elements.[131,132]

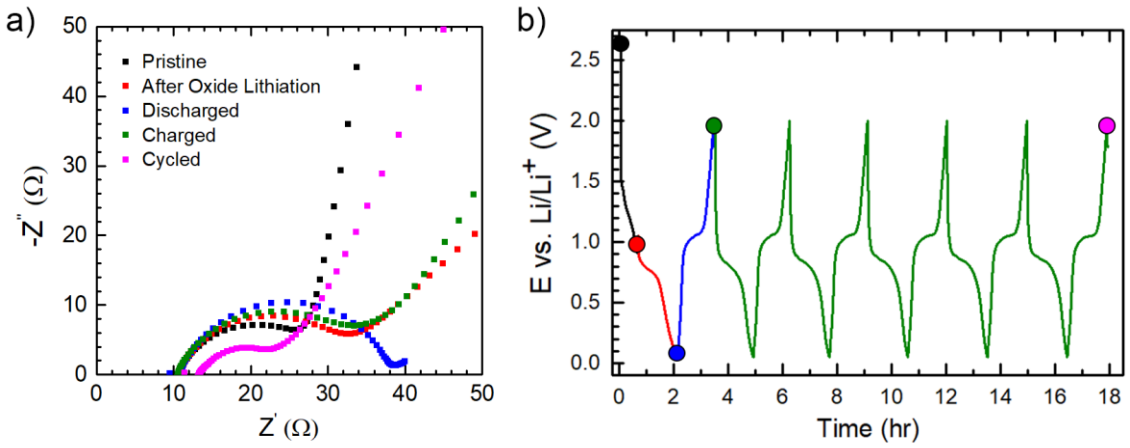

Figure 5.24: (a) Electrochemical impedance spectroscopy (EIS) of a nanocrystal-based working electrode in a half cell at different states of charge. The color of each EIS curve corresponds to the marker where it was collected during galvanostatic cycling in panel (b). Each curve features a single semicircle that was fit with a parallel resistor/capacitor equivalent circuit. We attribute this feature to the charge transfer process, and the extracted resistance is reported here. The black spectrum is from the pristine electrode (20.9 Ω), the red spectrum is from the electrode after initial lithiation of the surface oxide (24.8 Ω), the blue spectrum is after full discharge (28.0 Ω), the green spectrum is after full charge (27.7 Ω), and the pink spectrum is after six cycles (13.0 Ω).

5.5 Comparison to Other Material Systems

While the discovery of these transformations in nanoscale Sb appear to be in contrast to results on many other alloy materials which simply shrink upon delithiation and therefore support unstable SEI growth,[29,30] our chemomechanical model suggests that particle size and the mechanical properties of the oxide layer are critical for enabling this spontaneous void formation. Non-uniform pore formation has also been observed within Sn particles, but these pores were not within every particle and were at the oxide surface,[29]

perhaps indicating a non-ideal oxide layer. Previous studies have shown that porous structures can form during delithiation of other alloy materials (such as Si) which are confined by native oxide layers,[42,43] but this process results in a porous network and there is still overall volume change of the material. Critically, this random pore formation was not shown to be reversible, and the resulting dimensional changes of the outer surfaces during volume changes are expected to lead to reduced CE.

Our model further suggests that voiding transformations will not be limited to Li-ion systems. Since the mechanical properties of a sodiated oxide layer are likely similar to the lithiated oxide, we carried out additional experiments to investigate the behavior of Sb during reaction with Na rather than Li. As shown in Fig. 5.25, similar void morphologies were observed upon desodiation of reacted particles, but with less uniformity and consistency compared to Li. The morphology of the delithiated and desodiated particles is similar. In Fig. 5.25, it is clear that there is some merging of the oxide shells between particles after the reaction process, which is especially clear for the desodiation case in Fig. 5.25b. The metal regions within the oxide shells remain distinct, however. This is in contrast to prior reports on alloy anode materials with larger particle size (such as tin[29]), in which the metal can directly contact and merge together or sinter over time. Interestingly, delamination of Sb thin films from a substrate during sodiation has previously been observed to cause pore formation,[78] but this mechanism is distinct from the hollowing observed here. These experiments on Na, along with prior results on other alloy materials, support our model and indicate that these findings could be applicable to a variety of alloy anode compounds.

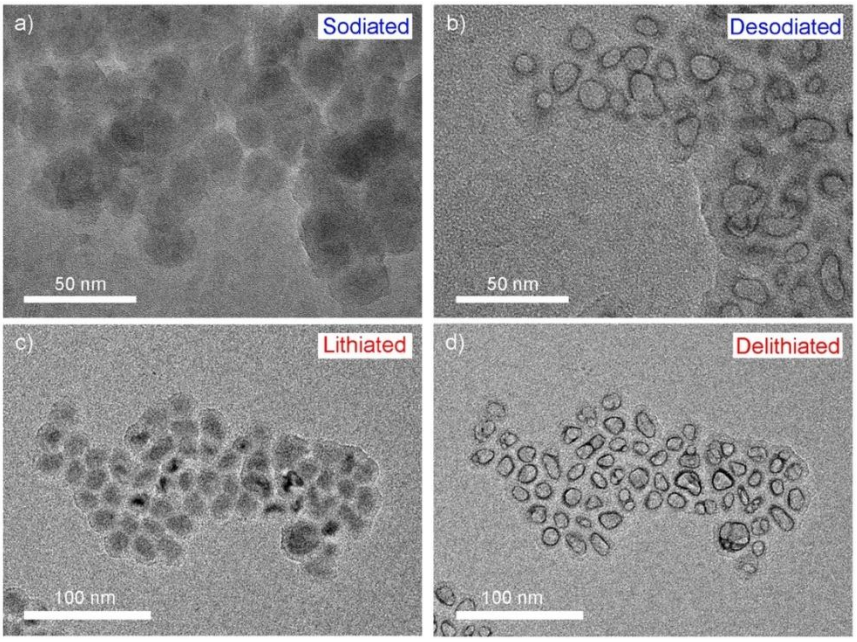

Figure 5.25: Comparing *in situ* TEM sodiation/desodiation of Sb nanocrystals to lithiation/delithiation. **(a)** TEM image of a group of Sb nanocrystals that have undergone sodiation. **(b)** Image of a different group of Sb nanocrystals that have been desodiated. **(c)** TEM image of a group of Sb nanocrystals that have undergone lithiation, and **(d)** the same group after delithiation.

5.6 Conclusions

This investigation has shown that Sb nanocrystals below a critical size spontaneously evolve to form hollow structures during delithiation that can be reversibly filled and vacated within the internal void space during cycling. The correlated *ex situ* TEM experiments also provides evidence that this hollowing process occurs in real electrochemical cells with liquid electrolytes. This unique behavior was only observed in nanoscale electrode materials and, as was found in the previous two chapters, this difference in size of the active material led to a change in the reaction pathway. However,

unlike the previous two studies, the difference in behavior was caused by the development of a naturally occurring oxide, not by the difference in the alkali-metal ion. These small uniformly-shaped internal particles did not cause this oxide to buckle during delithiation, which allowed for stable cycling. Such behavior is highly desired for alloy anodes that can exhibit long-term stability,[38,40,77] since the dimensionally-stable outer surface of such particles can enable passivating and self-terminating SEI growth. Indeed, the conventional electrochemical experiments show consistently higher CE for electrodes made from the smallest nanocrystals compared to larger nanoparticles. These results provide important insight into the stable electrochemical cycling performance of small Sb nanocrystals,[74] which is uncommon for unaltered alloy anode materials.[18,34] The reversible hollowing process during reaction of Sb nanocrystals is likely a key factor that enables stable SEI growth and the observed long-term electrochemical stability of this material.

Intensive research efforts in recent years have focused on designing synthetic hollow nanostructures with outer shells made of carbon and other materials to enable repeatable cycling of alloy materials with high specific and volumetric capacity.[17,36–38] While these efforts have often involved complex procedures that include removal of sacrificial material and require precise control of composition and structure,[38,77] our findings show that Sb nanocrystals naturally and spontaneously evolve to form very similar hollow nanostructures during electrochemical cycling. The ability to form hollow materials *in situ* presents the potential for cost savings and easier manufacturing of stable, high-capacity battery electrodes.

Finally, these results and the developed model can serve as a tool to guide the creation of oxide or other types of shells that enable alloying materials to undergo voiding

transformations *in situ*. In contrast to the generally held view that a native surface oxide is detrimental, this work shows that it is instead a critical feature that enables unique transformation mechanisms in high-capacity materials. Even in alloy materials that do not form robust oxide layers, it may be possible to tailor SEI structure through the use of electrolyte additives or electrochemical formation steps to create mechanically resilient SEI shells that also enable voiding transformations. Thus, by controlling surface layer properties and nanocrystal size, simplified nanoscale alloy materials could be created to enable high-energy batteries with long-term cycling life.

CHAPTER 6. CONCLUSIONS AND FUTURE WORK

This dissertation has examined the effect that alkali-metal ions have on several different high-capacity large-volume-change electrode materials. To this end, *in situ* TEM was used to understand the nanoscale transformation pathways during reaction with Li^+, Na^+, and K^+ ions and then to connect these nanoscale reaction pathways to the electrochemical behavior of these electrode materials. This technique made it possible to identify connections between the size and shape of the nanostructured materials and the structural and volumetric changes that occurred during the reaction both with Li^+ and with the large alkali metal ions. Understanding gained through these experiments can be used to engineer more cost-effective, high-capacity battery materials characterized by high Coulombic efficiency and longer cycle lives.

The study on the displacement-type Cu_2S electrode material showed that glyme-based electrolyte enabled stable cyclability in the Na/Cu_2S. The stable cycling occurred despite the significant morphological changes that this material undergoes during the sodiation reaction. Real-time observation revealed that this reaction proceeded via an unknown nanoscale reaction pathway that was completely different from the reaction pathway in the lithiation case. It was found that during slow sodiation, a thin film forms around the nanocrystals, which then prevent the Cu from diffusing out to the surface. This morphology was found to be much more electrochemically stable than the lithiation case and was the result of the large sodium ion.

Further study of this material system can include the examination of the mechanical stress that this Cu_2S material undergoes during cycling as the large Cu forms within the interior of the particles. Additionally, although cycling these materials during *in situ* TEM experiments has proven difficult in the past, the desodiation and resodiation reaction must be examined to understand the stable cycling behavior this material shows in electrochemical cells. This could be done by developing all-liquid electrochemical cells that make use of *in situ* liquid cell TEM specimen holders. However, the experiments must be designed carefully so as to ensure proper electrochemical behavior and to avoid electron beam effects interacting with the electrolyte.

In chapter 4 a promising conversion-type material, FeS_2, was studied to determine the effect that the size of different alkali-metal ions has on the reaction mechanisms and morphological evolution. *In situ* TEM experiments revealed that, while each reaction had a sharp two-phase reaction front, the smaller volume changes associated with lithiation resulted in fracture, while the much larger volume expansions that took place during sodiation and potassiation did not cause fracture. Nanoindentation tests performed on the reacted materials showed that the hardness and reduced modulus of the materials were found to be similar, so the mechanical properties of the reacted materials were likely not the central cause for the difference in fracture behavior. The different shape evolution during the reaction was found to be the major cause of particle fracture, since chemomechanical finite-element modeling demonstrated that the anisotropic lithiation led to a greater accumulation of stress than the in the more isotropic reaction with sodium and potassium. Overall, these results demonstrate that the different reaction pathways can

influence the fracture behavior and, therefore, the overall stability of these types of electrode materials.

Further study of this material system could, through the use of *in situ* TEM, investigate the cycling behavior. Additionally, more in-depth mechanical testing of the reacted material must be conducted to determine the extent to which the mechanical properties affect the fracture behavior. In particular, the fracture toughness of the reacted material will be required to fully understand the fracture behavior of these two-phase mixtures. Finally, while the size of the FeS_2 nanocrystals was found to affect the concavity of the reaction front, the effect of the shape remains unknown. We could examine the effect that the particle shape by synthesizing FeS_2 nanocrystals to be spherical to see if the lithiation of this material always preferentially reacts the {100} planes, even when the nanocrystal is not cubic.

In addition to studying the effects that alkali metals have on conversion-type materials, *in situ* TEM techniques were used to discover the unique behavior of antimony nanocrystals as it underwent an alloying-type reaction. The uniform shape and sufficiently small size of the Sb nanocrystals were found to spontaneously form voids within an oxide shell matrix upon delithiation. These voids could be reversibly filled and vacated over numerous cycles. During cycling, as lithium was removed, the Sb was found to remain within the interior of the voided oxide structure; upon relithiation, with no change in the external surface, the voids were filled. This morphology, resulting from the natural formation of the oxide in the first discharge, was found to lead to exceptional electrochemical properties with high capacity retention and coulombic efficiency. Finally, a simple chemomechanical model was developed to explain the formation of the voids

within the oxide shell that can be applied to other types of alloying materials in future studies. The model was based on a thin-walled pressure vessel and demonstrated the balance between the strain that develops during delithiation and the stress the oxide layer must withstand in order to not lead to the buckling of the oxide. This model also demonstrated that this void formation behavior was dependent on the size of the internal lithiated particle and the thickness of the oxide layer. Further study of this material needs to be conducted to determine the effect of sodiation and potassiation on this voiding behavior. While initial sodiation tests have been conducted on this material, we still need to figure out how to improve the void formation within these materials and thus to improve their electrochemical performance.

As a whole, these studies showed that Cu_2S, FeS_2, and Sb nanocrystals all demonstrated counter-intuitive morphological evolution and mechanical degradation behavior during electrochemical reaction. All of these naturally-occurring morphologies were found to lend themselves to more beneficial cycling behavior than most other high-capacity alloying/conversion-type electrode materials. These findings indicate that these types of large-volume-change materials could exhibit stable cycling performance that would make possible cost-effective, high-capacity next-generation battery systems.

This experimental technique, when applied to various battery materials, can open up numerous promising areas for further study. In these types of *in situ* experiments, large amounts of visual and diffraction data are collected, and, while some phenomena can seem obvious once the experiment is concluded, subtle changes and overall trends can be hard to notice, and the aid of a computer is necessary. By combining aspects of machine learning, important aspects of the materials evolution can be collected that would otherwise

go unnoticed. Improved data analytics could be a great boon in the further development of these types of experiments. In addition, these types of experiments can be further conducted on batteries with different chemistries, such as those relying on solid-electrolyte systems. These types of materials have recently seen a dramatic increase in attention because – compared to traditional Li-ion battery systems – batteries containing Li metal anode may be potentially safer and have higher energy density.[133] These materials use a solid ceramic electrolyte to shuttle ions between the anode and cathode rather than a liquid electrolyte soaked polymer. However, the interface between these solid electrolytes and the anodes and cathodes have proven to cause significant challenges relating to the charge transfer and chemo-mechanical degradation of the solid electrolyte.[124,134–136] During the research described in this dissertation, additional work was conducted using *in situ* TEM probing experiments on a solid-electrolyte material.[137] However, this issue needs to be further studied with the help of even more precise techniques as even subtle changes to the interphase between these materials can have a significant impact. Overall, the future of these types of experiments on battery materials remains bright as further understanding of the fundamental behavior of these systems can guide the advancement of the field.

.

APPENDIX

A.1 FeS_2 Chemomechanical Simulation Model

In Chapter 4, a chemomechanical model was used to determine the effect the shape of the reaction front had on the development of the stress concentration within the reaction particle and the reaction product mixture. This model was developed by our collaborators in Prof. Ting Zhu's group here at Georgia Tech. The chemomechanical model was developed to study the concurrent ion transport, reaction front migration, volume expansion, and stress generation in a cubic FeS_2 particle. These models were numerically implemented using the commercial finite element package ABAQUS. This model demonstrated that the difference in the shape evolution lead to an increase in the hydrostatic tensile stress the lithiated particles experienced, which could have contributed to the fracture behavior observed.

To capture the two-phase reaction at sharp phase boundaries, a non-linear diffusion model was employed with the concentration-dependent diffusion coefficient $D_0(C)$, where C is the alkali ion concentration normalized by the full capacity limit, as described in detail in previous work.[138] That is, the diffusivity of alkali ions in the reacted phase (corresponding to $C \approx 1$) is set to be 10^4 times that of the unreacted phase. As a result, diffusion of alkali ions is fast in the reacted shell and becomes much slower in the unreacted core ($C \approx 0$), leading to an abrupt change of the alkali ion concentration at the react front (*i.e.*, the core-shell interface). This concentration-dependent diffusion coefficient is used to model the lithiation process involving reaction fronts at {100} facets that intersect to form the sharp corners of the unreacted core. To simulate the rounded corners of the

unreacted core in the case of sodiation and potassiation, orientation-dependent diffusivity is utilized. It should be noted that diffusivity in the biphasic/amorphous reacted phase is expected to be effectively isotropic. However, anisotropic diffusivity is adopted to enable orientation-dependent mobility of the reaction front to create a curved surface, as demonstrated in our previous work.[15,120] Specifically, the diffusivity D is set to be dependent on the local material orientation according to

$$D = D_0\left(\cos\theta_x + \cos\theta_y + \cos\theta_z\right)^4, \qquad \text{(A1.1)}$$

where $D_0(C)$ is the concentration-dependent diffusion coefficient described above, and $\cos\theta_x$, $\cos\theta_y$, and $\cos\theta_z$ are the direction cosines between the three coordinate axes and the local unit vector that links the origin of the Cartesian coordinate system located at the center of the particle to the current position of the material point. Given the coordinate (x, y, z) of the material point, these direction cosines are calculated as x/r, y/r, and z/r, where $r = \sqrt{x^2 + y^2 + z^2}$. As a result, the diffusivity along the <100>, <110>, and <111> directions are D_0, $4D_0$, and $9D_0$ (respectively). These diffusivity values cause anisotropic mobility of the reaction front to be attained, thereby enabling the simulation of rounded edges and corners during sodiation/potassiation. The non-linear diffusion models for lithiation and sodiation described above were numerically implemented by using temperature as a surrogate for ion concentration in ABAQUS since the governing transport equations are identical. A user subroutine UMATHT in ABAQUS was developed to implement the concentration and orientation-dependence of diffusivity.

To model the stress generation during reaction, an elastic and perfectly plastic model was used to describe the reaction-induced deformation, which is similar to our

previous model of the lithiation of silicon.[138] That is, the total strain increment tensor is subdivided into chemical, elastic, and plastic components,

$$d\varepsilon_{ij} = d\varepsilon_{ij}^{e} + d\varepsilon_{ij}^{p} + d\varepsilon_{ij}^{c} \qquad \text{(A1.2)}$$

In Eq. (A1.2), the increment of elastic strain $d\varepsilon_{ij}^{e}$ obeys the linear elastic Hooke's law. The increment of plastic strain $d\varepsilon_{ij}^{p}$ obeys the classic J_2-flow rule. The yield stress is assumed to be $0.05E$, where E is Young's modulus of the unreacted phase. The Poisson's ratio is taken as the typical value of 0.3. The crystalline core is modeled as an isotropic, elastic material; the reacted material is isotropic, elastic, and perfectly plastic, so as to enable plastic flow behavior for accommodating large volume changes at the sharp reaction front. The increment of the chemical strain $d\varepsilon_{ij}^{c}$ is proportional to the increment of the normalized alkali ion concentration dc according to $d\varepsilon_{ij}^{c} = \beta_{ij} dc$, where β_{ij} represents the isotropic expansion coefficient. Based on the experimentally observed volume expansion of 1.8 for lithiation and 2.7 for sodiation, we use a representative volume expansion value of 2.2, and correspondingly $\beta_{ij} = 0.26\delta_{ij}$, where δ_{ij} is 1 when $i = j$ and 0 otherwise. The concentration maps of the lithiation and the sodiation/potassiation reaction and their resulting hydrostatic tensile stress can be seen in Figure 4.15. Slices from the hydrostatic map can be seen in Figure A1.1 below.

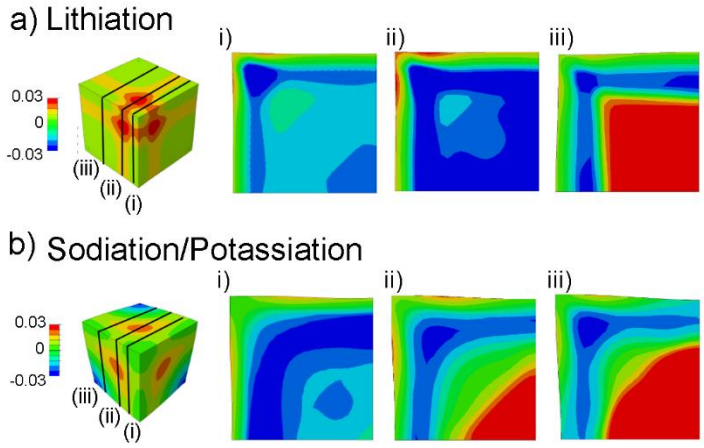

Figure A1.1: Chemomechanical finite element simulation results showing stress generation during reaction of a cubic FeS_2 particle with different reaction front shapes. **(a)** Simulation results of the reaction when the inner crystal retains a cubic shape with a sharp corner (*i.e.*, the lithiation case) showing a contour plot of hydrostatic tensile stress σ_h (normalized by Young's modulus). Different slices are taken from this contour plot and shown in (i-iii) **(b)** Simulation results of the reaction when the inner crystal develops a rounded-off or blunted corner (*i.e.*, sodiation or potassiation) showing a contour plot of hydrostatic tensile stress σ_h (normalized by Young's modulus). Different slices are taken from this contour plot and shown in (i-iii).

REFERENCES

1. Thackeray, M. M., Wolverton, C. & Isaacs, E. D. Electrical energy storage for transportation—approaching the limits of, and going beyond, lithium-ion batteries. *Energy Environ. Sci.* **5**, 7854 (2012).
2. Dunn, B., Kamath, H. & Tarascon, J.-M. Electrical Energy Storage for the Grid: A Battery of Choices. *Science* **334**, 928–935 (2011).
3. Kang, H. *et al.* Update on anode materials for Na-ion batteries. *J. Mater. Chem. A* **3**, 17899–17913 (2015).
4. Yabuuchi, N., Kubota, K., Dahbi, M. & Komaba, S. Research Development on Sodium-Ion Batteries. *Chem. Rev.* **114**, 11636–11682 (2014).
5. Schmuch, R., Wagner, R., Hörpel, G., Placke, T. & Winter, M. Performance and cost of materials for lithium-based rechargeable automotive batteries. *Nat. Energy* **3**, 267–278 (2018).
6. Choi, J. W. & Aurbach, D. Promise and reality of post-lithium-ion batteries with high energy densities. *Nat. Rev. Mater.* **1**, 16013 (2016).
7. Kamali, A. R. & Fray, D. J. Review on carbon and silicon based materials as anode materials for lithium ion batteries. *J. New Mater. Electrochem. Syst.* **13**, 147–160 (2010).
8. Marom, R., Amalraj, S. F., Leifer, N., Jacob, D. & Aurbach, D. A review of advanced and practical lithium battery materials. *J. Mater. Chem.* **21**, 9938–9954 (2011).
9. Zhang, W.-J. J. A review of the electrochemical performance of alloy anodes for lithium-ion batteries. *J. Power Sources* **196**, 13–24 (2011).
10. Huggins, R. A. *Advanced Batteries: Materials Science Aspects*. *Advanced Batteries: Materials Science Aspects* (Springer, 2009). doi:10.1007/978-0-387-76424-5
11. Nitta, N., Wu, F., Lee, J. T. & Yushin, G. Li-ion battery materials: present and future. *Mater. Today* **18**, 252–264 (2015).
12. Hayner, C. M., Zhao, X. & Kung, H. H. Materials for Rechargeable Lithium-Ion Batteries. *Annu. Rev. Chem. Biomol. Eng.* **3**, 445–471 (2012).
13. Goodenough, J. B. & Kim, Y. Challenges for Rechargeable Li Batteries. *Chem. Mater.* **22**, 587–603 (2010).
14. Palacín, M. R. Recent advances in rechargeable battery materials: a chemist's perspective. *Chem. Soc. Rev.* **38**, 2565 (2009).
15. Liu, X. H. *et al.* Anisotropic Swelling and Fracture of Silicon Nanowires during Lithiation. *Nano Lett.* **11**, 3312–3318 (2011).
16. Lee, S. W., McDowell, M. T., Berla, L. A., Nix, W. D. & Cui, Y. Y. Fracture of

crystalline silicon nanopillars during electrochemical lithium insertion. *Proc. Natl. Acad. Sci.* **109**, 4080–4085 (2012).

17. Liu, N. *et al.* A pomegranate-inspired nanoscale design for large-volume-change lithium battery anodes. *Nat. Nanotechnol.* **9**, 187–192 (2014).

18. McDowell, M. T., Xia, S. & Zhu, T. The mechanics of large-volume-change transformations in high-capacity battery materials. *Extrem. Mech. Lett.* **9**, 480–494 (2016).

19. McDowell, M. T. *et al.* In situ observation of divergent phase transformations in individual sulfide nanocrystals. *Nano Lett.* **15**, 1264–1271 (2015).

20. Larcher, D. *et al.* Recent findings and prospects in the field of pure metals as negative electrodes for Li-ion batteries. *J. Mater. Chem.* **17**, 3759–3772 (2007).

21. Kasavajjula, U., Wang, C. & Appleby, A. J. Nano- and bulk-silicon-based insertion anodes for lithium-ion secondary cells. *Journal of Power Sources* **163**, 1003–1039 (2007).

22. Obrovac, M. N. & Chevrier, V. L. Alloy Negative Electrodes for Li-Ion Batteries. *Chem. Rev.* **114**, 11444–11502 (2014).

23. McDowell, M. T., Lee, S. W., Nix, W. D. & Cui, Y. 25th Anniversary Article: Understanding the Lithiation of Silicon and Other Alloying Anodes for Lithium-Ion Batteries. *Adv. Mater.* **25**, 4966–4985 (2013).

24. Chen, Q. & Sieradzki, K. Spontaneous evolution of bicontinuous nanostructures in dealloyed Li-based systems. *Nat. Mater.* **12**, 1102–1106 (2013).

25. Boebinger, M. G. *et al.* Distinct nanoscale reaction pathways in a sulfide material for sodium and lithium batteries. *J. Mater. Chem. A* **5**, 11701–11709 (2017).

26. Débart, A., Dupont, L., Patrice, R. & Tarascon, J.-M. Reactivity of transition metal (Co, Ni, Cu) sulphides versus lithium: The intriguing case of the copper sulphide. *Solid State Sci.* **8**, 640–651 (2006).

27. Kirshenbaum, M. J., Boebinger, M. G., Katz, M. J., McDowell, M. T. & Dasog, M. Solid-State Route for the Synthesis of Scalable, Luminescent Silicon and Germanium Nanocrystals. *ChemNanoMat* **4**, 423–429 (2018).

28. Jache, B., Mogwitz, B., Klein, F. & Adelhelm, P. Copper sulfides for rechargeable lithium batteries: Linking cycling stability to electrolyte composition. *J. Power Sources* **247**, 703–711 (2013).

29. Wang, J. *et al.* Structural Evolution and Pulverization of Tin Nanoparticles during Lithiation-Delithiation Cycling. *J. Electrochem. Soc.* **161**, F3019–F3024 (2014).

30. McDowell, M. T. *et al.* In situ TEM of two-phase lithiation of amorphous silicon nanospheres. *Nano Lett.* **13**, 758–764 (2013).

31. Boebinger, M. G. *et al.* Avoiding Fracture in a Conversion Battery Material through Reaction with Larger Ions. *Joule* **2**, 1783–1799 (2018).

32. Ebner, M., Marone, F., Stampanoni, M. & Wood, V. Visualization and Quantification of Electrochemical and Mechanical Degradation in Li Ion Batteries.

Science **342**, 716–720 (2013).

33. Qi, W. *et al.* Nanostructured anode materials for lithium-ion batteries: principle, recent progress and future perspectives. *J. Mater. Chem. A* **5**, 19521–19540 (2017).

34. Zhang, S., Zhao, K., Zhu, T. & Li, J. Electrochemomechanical degradation of high-capacity battery electrode materials. *Progress in Materials Science* **89**, 479–521 (2017).

35. Wu, H. *et al.* Stable cycling of double-walled silicon nanotube battery anodes through solid–electrolyte interphase control. *Nat. Nanotechnol.* **7**, 310–315 (2012).

36. Liu, N. *et al.* A yolk-shell design for stabilized and scalable Li-ion battery alloy anodes. *Nano Lett.* **12**, 3315–3321 (2012).

37. Hwang, T. H., Lee, Y. M., Kong, B. S., Seo, J. S. & Choi, J. W. Electrospun core-shell fibers for robust silicon nanoparticle-based lithium ion battery anodes. *Nano Lett.* **12**, 802–807 (2012).

38. Liu, J. *et al.* New Nanoconfined Galvanic Replacement Synthesis of Hollow Sb@C Yolk-Shell Spheres Constituting a Stable Anode for High-Rate Li/Na-Ion Batteries. *Nano Lett.* **17**, 2034–2042 (2017).

39. Ng, S. H. *et al.* Highly reversible lithium storage in spheroidal carbon-coated silicon nanocomposites as anodes for lithium-ion batteries. *Angew. Chemie - Int. Ed.* **45**, 6896–6899 (2006).

40. Liu, S., Feng, J., Bian, X., Liu, J. & Xu, H. The morphology-controlled synthesis of a nanoporous-antimony anode for high-performance sodium-ion batteries. *Energy Environ. Sci.* **9**, 1229–1236 (2016).

41. Geng, P. *et al.* Polypyrrole coated hollow metal-organic framework composites for lithium-sulfur batteries. *J. Mater. Chem. A* **7**, 19465–19470 (2019).

42. Adkins, E. R., Jiang, T., Luo, L., Wang, C.-M. & Korgel, B. A. In Situ Transmission Electron Microsopy of Oxide Shell-Induced Pore Formation in (De)lithiated Silicon Nanowires. *ACS Energy Lett.* **3**, 2829–2834 (2018).

43. He, Y. *et al.* In situ transmission electron microscopy probing of native oxide and artificial layers on silicon nanoparticles for lithium ion batteries. *ACS Nano* **8**, 11816–11823 (2014).

44. Chevrier, V. L. & Ceder, G. Challenges for Na-ion Negative Electrodes. *J. Electrochem. Soc.* **158**, A1011 (2011).

45. Slater, M. D., Kim, D., Lee, E. & Johnson, C. S. Sodium-Ion Batteries. *Adv. Funct. Mater.* **23**, 947–958 (2013).

46. Jian, Z., Luo, W. & Ji, X. Carbon Electrodes for K-Ion Batteries. *J. Am. Chem. Soc.* **137**, 11566–11569 (2015).

47. Eftekhari, A., Jian, Z. & Ji, X. Potassium Secondary Batteries. *ACS Applied Materials and Interfaces* **9**, 4404–4419 (2017).

48. Kubota, K. & Komaba, S. Review—Practical Issues and Future Perspective for

Na-Ion Batteries. *J. Electrochem. Soc.* **162**, A2538–A2550 (2015).

49. Kundu, D., Talaie, E., Duffort, V. & Nazar, L. F. The Emerging Chemistry of Sodium Ion Batteries for Electrochemical Energy Storage. *Angew. Chemie Int. Ed.* **54**, 3431–3448 (2015).

50. Pramudita, J. C., Sehrawat, D., Goonetilleke, D. & Sharma, N. An Initial Review of the Status of Electrode Materials for Potassium-Ion Batteries. *Adv. Energy Mater.* **7**, 1602911 (2017).

51. Zhao, J., Zou, X., Zhu, Y., Xu, Y. & Wang, C. Electrochemical Intercalation of Potassium into Graphite. *Adv. Funct. Mater.* **26**, 8103–8110 (2016).

52. Tian, B. *et al.* Phase Transformations in TiS_2 during K Intercalation. *ACS Energy Lett.* **2**, 1835–1840 (2017).

53. Vaalma, C., Buchholz, D. & Passerini, S. Non-aqueous potassium-ion batteries: a review. *Current Opinion in Electrochemistry* **9**, 41–48 (2018).

54. Zhao, Y. *et al.* High-Rate and Ultralong Cycle-Life Potassium Ion Batteries Enabled by In Situ Engineering of Yolk-Shell FeS_2 @C Structure on Graphene Matrix. *Adv. Energy Mater.* **8**, 1802565 (2018).

55. Li, S. *et al.* High-rate aluminium yolk-shell nanoparticle anode for Li-ion battery with long cycle life and ultrahigh capacity. *Nat. Commun.* **6**, 7872 (2015).

56. Wang, Q. *et al.* Reaction and Capacity-Fading Mechanisms of Tin Nanoparticles in Potassium-Ion Batteries. *J. Phys. Chem. C* **121**, 12652–12657 (2017).

57. Yang, H. *et al.* A chemo-mechanical model of lithiation in silicon. *J. Mech. Phys. Solids* **70**, 349–361 (2014).

58. Zhao, K. *et al.* Concurrent Reaction and Plasticity during Initial Lithiation of Crystalline Silicon in Lithium-Ion Batteries. *J. Electrochem. Soc.* **159**, A238–A243 (2012).

59. Evans, H. T. The crystal structures of low chalcocite and djurIeite. *Kristallogr.* **150**, 299–320 (1979).

60. Rivest, J. B., Fong, L.-K., Jain, P. K., Toney, M. F. & Alivisatos, A. P. Size Dependence of a Temperature-Induced Solid–Solid Phase Transition in Copper(I) Sulfide. *J. Phys. Chem. Lett.* **2**, 2402–2406 (2011).

61. Sands, T. D., Washburn, J. & Gronsky, R. High Resolution Observations of Copper Vacancy Ordering in Chalcocite (Cu2S) and the Transformation to Djurleite (Cu1.97 to 1.94S). *Phys. status solidi* **72**, 551–559 (1982).

62. Kim, J. S. *et al.* The electrochemical properties of copper sulfide as cathode material for rechargeable sodium cell at room temperature. *J. Power Sources* **189**, 864–868 (2009).

63. Zhang, S. S. The redox mechanism of FeS2 in non-aqueous electrolytes for lithium and sodium batteries. *J. Mater. Chem. A* **3**, 7689–7694 (2015).

64. Douglas, A. *et al.* Ultrafine Iron Pyrite (FeS_2) Nanocrystals Improve Sodium–Sulfur and Lithium–Sulfur Conversion Reactions for Efficient Batteries. *ACS*

Nano **9**, 11156–11165 (2015).

65. Tomczuk, Z., Tani, B., Otto, N. C., Roche, M. F. & Vissers, D. R. Phase Relationships in Positive Electrodes of High Temperature Li-AI/LiCI-KCI/FeS2 Cells. *J. Electrochem. Soc.* **129**, 925–931 (1982).

66. Whiteley, J. M. *et al.* FeS2-Imbedded Mixed Conducting Matrix as a Solid Battery Cathode. *Adv. Energy Mater.* **6**, 1600495 (2016).

67. Shao-Horn, Y., Osmialowski, S. & Horn, Q. C. Nano-FeS_2 for Commercial Li/FeS_2 Primary Batteries. *J. Electrochem. Soc.* **149**, A1499 (2002).

68. Chen, K. *et al.* Mechanism of Capacity Fade in Sodium Storage and the Strategies of Improvement for FeS_2 Anode. *ACS Appl. Mater. Interfaces* **9**, 1536–1541 (2017).

69. Jones, C. H. W. W., Dahn, J. R., Fong, R., Dahn, J. R. & Jones, C. H. W. W. Electrochemistry of Pyrite-Based Cathodes for Ambient Temperature Lithium Batteries. **136**, (1989).

70. Hu, Z. *et al.* Pyrite FeS2 for high-rate and long-life rechargeable sodium batteries. *Energy Environ. Sci.* **8**, 1309–1316 (2015).

71. Walter, M., Zünd, T. & Kovalenko, M. V. Pyrite (FeS2) nanocrystals as inexpensive high-performance lithium-ion cathode and sodium-ion anode materials. *Nanoscale* **7**, 9158–9163 (2015).

72. Wang, Y. X. *et al.* Uniform yolk-shell iron sulfide-carbon nanospheres for superior sodium-iron sulfide batteries. *Nat. Commun.* **6**, (2015).

73. Yersak, T. A. *et al.* Solid State Enabled Reversible Four Electron Storage. *Adv. Energy Mater.* **3**, 120–127 (2013).

74. He, M., Kravchyk, K., Walter, M. & Kovalenko, M. V. Monodisperse Antimony Nanocrystals for High-Rate Li-ion and Na-ion Battery Anodes: Nano versus Bulk. *Nano Lett.* **14**, 1255–1262 (2014).

75. Darwiche, A. *et al.* Better Cycling Performances of Bulk Sb in Na-Ion Batteries Compared to Li-Ion Systems: An Unexpected Electrochemical Mechanism. *J. Am. Chem. Soc.* **134**, 20805–20811 (2012).

76. Baggetto, L. *et al.* Intrinsic thermodynamic and kinetic properties of Sb electrodes for Li-ion and Na-ion batteries: experiment and theory. *J. Mater. Chem. A* **1**, 7985 (2013).

77. Liu, Y., Zhou, B., Liu, S., Ma, Q. & Zhang, W.-H. Galvanic Replacement Synthesis of Highly Uniform Sb Nanotubes: Reaction Mechanism and Enhanced Sodium Storage Performance. *ACS Nano* **13**, 5885–5892 (2019).

78. Li, Z. *et al.* Coupling In Situ TEM and Ex Situ Analysis to Understand Heterogeneous Sodiation of Antimony. *Nano Lett.* **15**, 6339–6348 (2015).

79. Aricò, A. S., Bruce, P., Scrosati, B., Tarascon, J.-M. & van Schalkwijk, W. Nanostructured materials for advanced energy conversion and storage devices. *Nat. Mater.* **4**, 366–377 (2005).

80. Williams, D. B. & Carter, C. B. *Transmission Electron Microscopy*. *Transmission Electron Microscopy* (Springer US, 2009). doi:10.1007/978-0-387-76501-3_1

81. McDowell, M., Kondekar, N., Boebinger, M. G. & Cortes, F. J. Q. In situ investigation of dynamic processes in materials for energy storage. in *Energy Harvesting and Storage: Materials, Devices, and Applications VIII* (eds. Dhar, N. K., Dutta, A. K. & Balaya, P.) **10663**, 9 (SPIE, 2018).

82. Wang, Z. *et al.* In situ STEM-EELS observation of nanoscale interfacial phenomena in all-solid-state batteries. *Nano Lett.* **16**, 3760–3767 (2016).

83. Ross, F. M. Opportunities and challenges in liquid cell electron microscopy. *Science* **350**, aaa9886–aaa9886 (2015).

84. Yuk, J. M. *et al.* High-resolution EM of colloidal nanocrystal growth using graphene liquid cells. *Science* **335**, 61–64 (2012).

85. Huang, J. Y. Y. *et al.* In situ observation of the electrochemical lithiation of a single SnO2 nanowire electrode. *Science* **330**, 1515–1520 (2010).

86. He, Y. *et al.* Origin of lithium whisker formation and growth under stress. *Nat. Nanotechnol.* **14**, 1042–1047 (2019).

87. McDowell, M. T. *et al.* Studying the Kinetics of Crystalline Silicon Nanoparticle Lithiation with In Situ Transmission Electron Microscopy. *Adv. Mater.* **24**, 6034–6041 (2012).

88. Wang, F. *et al.* Tracking lithium transport and electrochemical reactions in nanoparticles. *Nat. Commun.* **3**, 1201 (2012).

89. He, K. *et al.* Transitions from Near-Surface to Interior Redox upon Lithiation in Conversion Electrode Materials. *Nano Lett.* **15**, 1437–1444 (2015).

90. Heideman, M. T., Johnson, D. H. & Burrus, C. S. Gauss and the History of the Fast Fourier Transform. *IEEE ASSP Mag.* **1**, 14–21 (1984).

91. Arganda-Carreras, I. *et al.* Trainable Weka Segmentation: a machine learning tool for microscopy pixel classification. *Bioinformatics* **33**, 2424–2426 (2017).

92. Tang, A. *et al.* One-pot synthesis and self-assembly of colloidal copper(I) sulfide nanocrystals. *Nanotechnology* **21**, 285602 (2010).

93. Macpherson, H. A. & Stoldt, C. R. Iron Pyrite Nanocubes: Size and Shape Considerations for Photovoltaic Application. *ACS Nano* **6**, 8940–8949 (2012).

94. Britannica, E. of E. Bragg Law. *Encyclopaedia Britannica* (1998). Available at: https://www.britannica.com/science/Bragg-law. (Accessed: 22nd January 2020)

95. Klein, F., Jache, B., Bhide, A. & Adelhelm, P. Conversion reactions for sodium-ion batteries. *Phys. Chem. Chem. Phys.* **15**, (2013).

96. Zhu, Y. *et al.* Ether-based electrolyte enabled Na/FeS 2 rechargeable batteries. *Electrochem. commun.* **54**, 18–22 (2015).

97. Seh, Z. W. *et al.* Sulphur-TiO 2 yolk-shell nanoarchitecture with internal void space for long-cycle lithium-sulphur batteries. *Nat. Commun.* **4**, (2013).

98. Ren, W., Ma, W., Zhang, S. & Tang, B. Recent advances in shuttle effect inhibition for lithium sulfur batteries. (2019). doi:10.1016/j.ensm.2019.02.022

99. Cohn, A. P., Share, K., Carter, R., Oakes, L. & Pint, C. L. Ultrafast Solvent-Assisted Sodium Ion Intercalation into Highly Crystalline Few-Layered Graphene. *Nano Lett.* **16**, 543–548 (2016).

100. Seh, Z. W., Sun, J., Sun, Y. & Cui, Y. A Highly Reversible Room-Temperature Sodium Metal Anode. *ACS Cent. Sci.* **1**, 449–455 (2015).

101. Jache, B., Binder, J. O., Abe, T. & Adelhelm, P. A comparative study on the impact of different glymes and their derivatives as electrolyte solvents for graphite co-intercalation electrodes in lithium-ion and sodium-ion batteries. *Phys. Chem. Chem. Phys.* **18**, 14299–14316 (2016).

102. Kim, H. *et al.* Sodium intercalation chemistry in graphite. *Energy Environ. Sci.* **8**, 2963–2969 (2015).

103. Shi, C., Li, X., He, X. & Zhao, J. New Insight into the Interaction between Carbonate-based Electrolyte and Cuprous Sulfide Electrode Material for Lithium Ion Batteries. *Electrochim. Acta* **174**, 1079–1087 (2015).

104. He, K. *et al.* Visualizing non-equilibrium lithiation of spinel oxide via in situ transmission electron microscopy. *Nat. Commun.* **7**, 11441 (2016).

105. Cabana, J., Monconduit, L., Larcher, D. & Palacín, M. R. Beyond Intercalation-Based Li-Ion Batteries: The State of the Art and Challenges of Electrode Materials Reacting Through Conversion Reactions. *Adv. Mater.* **22**, E170–E192 (2010).

106. Cassaignon, S., Pauporté, T., Guillemoles, J.-F. F. & Vedel, J. Copper diffusion in copper sulfide: a systematic study. *Ionics (Kiel).* **4**, 364–371 (1998).

107. He, K. *et al.* Sodiation Kinetics of Metal Oxide Conversion Electrodes: A Comparative Study with Lithiation. *Nano Lett.* **15**, 5755–5763 (2015).

108. Linden, D. *et al. HANDBOOK OF BATTERIES*. (2002).

109. Butala, M. M. *et al.* Local Structure Evolution and Modes of Charge Storage in Secondary Li–FeS $_2$ Cells. *Chem. Mater.* **29**, 3070–3082 (2017).

110. Liu, X. H. *et al.* In situ atomic-scale imaging of electrochemical lithiation in silicon. *Nat. Nanotechnol.* **7**, 749–756 (2012).

111. Mukhopadhyay, A., Kali, R., Badjate, S., Tokranov, A. & Sheldon, B. W. Plastic deformation associated with phase transformations during lithiation/delithiation of Sn. *Scr. Mater.* **92**, 47–50 (2014).

112. Xiao, X., Liu, P., Verbrugge, M. W. W., Haftbaradaran, H. & Gao, H. Improved cycling stability of silicon thin film electrodes through patterning for high energy density lithium batteries. *J. Power Sources* **196**, 1409–1416 (2011).

113. Gabrisch, H., Wilcox, J. & Doeff, M. M. TEM study of fracturing in spherical and plate-like LiFePO4 particles. *Electrochem. Solid-State Lett.* **11**, (2008).

114. Epler, E., Roddatis, V. V. & Volkert, C. A. Measuring Mechanical Properties during the Electrochemical Lithiation of Silicon. *Energy Technol.* **4**, 1575–1581

(2016).

115. Pharr, M., Choi, Y. S., Lee, D., Oh, K. H. & Vlassak, J. J. Measurements of stress and fracture in germanium electrodes of lithium-ion batteries during electrochemical lithiation and delithiation. *J. Power Sources* **304**, 164–169 (2016).

116. Nadimpalli, S. P. V. *et al.* On plastic deformation and fracture in Si films during electrochemical lithiation/delithiation cycling. *J. Electrochem. Soc.* **160**, A1885–A1893 (2013).

117. Kondekar, N. P., Boebinger, M. G., Woods, E. V. & McDowell, M. T. In Situ XPS Investigation of Transformations at Crystallographically Oriented MoS_2 Interfaces. *ACS Appl. Mater. Interfaces* **9**, 32394–32404 (2017).

118. Cortes, F. J. Q., Boebinger, M. G., Xu, M., Ulvestad, A. & McDowell, M. T. Operando Synchrotron Measurement of Strain Evolution in Individual Alloying Anode Particles within Lithium Batteries. *ACS Energy Lett.* **3**, 349–355 (2018).

119. Liu, X. H. *et al.* Size-Dependent Fracture of Silicon Nanoparticles During Lithiation. *ACS Nano* **6**, 1522–1531 (2012).

120. Yang, H. *et al.* Orientation-Dependent Interfacial Mobility Governs the Anisotropic Swelling in Lithiated Silicon Nanowires. *Nano Lett.* **12**, 1953–1958 (2012).

121. Choi, Y. S., Park, J. H., Ahn, J. P. & Lee, J. C. Anisotropic Swelling Governed by Orientation-Dependent Interfacial Na Diffusion in Single-Crystalline Sb. *Chem. Mater.* **31**, 1696–1703 (2019).

122. Gutiérrez-Kolar, J. S. *et al.* Interpreting Electrochemical and Chemical Sodiation Mechanisms and Kinetics in Tin Antimony Battery Anodes Using in Situ Transmission Electron Microscopy and Computational Methods. *ACS Appl. Energy Mater.* **2**, 3578–3586 (2019).

123. Xie, H. *et al.* β-SnSb for Sodium Ion Battery Anodes: Phase Transformations Responsible for Enhanced Cycling Stability Revealed by in Situ TEM. *ACS Energy Lett.* **3**, 1670–1676 (2018).

124. Tippens, J. *et al.* Visualizing Chemomechanical Degradation of a Solid-State Battery Electrolyte. *ACS Energy Lett.* **4**, 1475–1483 (2019).

125. Kravchyk, K. *et al.* Monodisperse and inorganically capped Sn and Sn/SnO2 nanocrystals for high-performance Li-ion battery anodes. *J. Am. Chem. Soc.* **135**, 4199–4202 (2013).

126. Singh, S., Valencia-Jaime, I., Pavlic, O. & Romero, A. H. Elastic, mechanical, and thermodynamic properties of Bi-Sb binaries: Effect of spin-orbit coupling. *Phys. Rev. B* **97**, 054108 (2018).

127. de Jong, M. *et al.* Charting the complete elastic properties of inorganic crystalline compounds. *Sci. Data* **2**, 150009 (2015).

128. Tran, R. *et al.* Data Descriptor: Surface energies of elemental crystals. *Sci. Data* **3**, (2016).

129. Goodno, B. J. & Gere, J. M. *Statics and Mechanics of Materials*. (Cengage Learning, 2019).

130. Hutchinson, J. W. Buckling of spherical shells revisited. *Proc. R. Soc. A Math. Phys. Eng. Sci.* **472**, 20160577 (2016).

131. Niu, K.-Y., Park, J., Zheng, H. & Alivisatos, A. P. Revealing Bismuth Oxide Hollow Nanoparticle Formation by the Kirkendall Effect. *Nano Lett.* **13**, 5715–5719 (2013).

132. Wang, W., Dahl, M. & Yin, Y. Hollow Nanocrystals through the Nanoscale Kirkendall Effect. *Chem. Mater.* **25**, 1179–1189 (2013).

133. Janek, J. & Zeier, W. G. *A solid future for battery development*. **1**, (Nature Publishing Group, 2016).

134. Lewis, J. A., Tippens, J., Cortes, F. J. Q. & McDowell, M. T. Chemo-Mechanical Challenges in Solid-State Batteries. *Trends Chem.* **1**, 845–857 (2019).

135. Augustyn, V., McDowell, M. T. & Vojvodic, A. *Toward an Atomistic Understanding of Solid-State Electrochemical Interfaces for Energy Storage*. *Joule* **2**, 2189–2193 (2018).

136. Kasemchainan, J. *et al.* Critical stripping current leads to dendrite formation on plating in lithium anode solid electrolyte cells. *Nat. Mater.* **18**, 1105–1111 (2019).

137. Lewis, J. A. *et al.* Interphase Morphology between a Solid-State Electrolyte and Lithium Controls Cell Failure. *ACS Energy Lett.* **4**, 591–599 (2019).

138. Huang, S., Fan, F., Li, J., Zhang, S. & Zhu, T. Stress generation during lithiation of high-capacity electrode particles in lithium ion batteries. *Acta Mater.* **61**, 4354–4364 (2013).